

TECHNISCHE UNIVERSITÄT MÜNCHEN

Lehrstuhl für Aerodynamik und Strömungsmechanik

**Analysis of the unsteady behavior in shockwave
turbulent boundary layer interaction**

Muzio Grilli

Vollständiger Abdruck der von der Fakultät für Maschinenwesen der
Technische Universität München zur Erlangung des akademischen
Grades eines

Doktor-Ingenieurs

genehmigten Dissertation.

Vorsitzender: Univ.-Prof. Dr. Phaedon-Stelios Koutsourelakis
Prüfer der Dissertation: 1. Univ.-Prof. Dr.-Ing. habil. Nikolaus A. Adams
2. Prof. Dr.-Ing. Roberto Verzicco
Università degli Studi di Roma 'Tor Vergata'
Italien

Die Dissertation wurde am 21.03.2013 bei der der Technische Univer-
sität München eingereicht und durch die Fakultät für Maschinenwe-
sen am 08.11.2013 angenommen.

Abstract

The need for better understanding of the shockwave/turbulent boundary layer interactions phenomenon has been driving research in this area for several decades. This work investigates the flow of a supersonic turbulent boundary layer along a compression-expansion ramp by means of large-eddy simulation. Several numerical tools have been developed and implemented into the in-house code of the Institute of Aerodynamics and Fluid Mechanics of the Technische Universität München, in order to perform the numerical simulation of this phenomenon.

A conservative immersed interface method for compressible viscous flows has been derived, implemented and validated, allowing for the treatment of complex geometries in a cartesian-grid based code. The proposed approach for large-eddy simulation has been analyzed and validated with special focus on wall bounded flows. All of the building blocks of the numerical code have been employed in the large-eddy simulation of the flow of a supersonic turbulent boundary layer over a compression-expansion ramp. Results from the computation have been validated through direct comparison with experimental measurements provided by [Zhel-tovodov et al., 1990].

The computational results confirm theoretical and experimental findings on fluctuation amplification across the shockwave/boundary layer interaction region and on turbulence damping through the interaction with rarefaction waves. The large-eddy simulation provides evidence of the existence of Görtler-like structures originating from the recirculation region and traveling downstream along the ramp.

The computation has shown clear evidence of the existence of a low-frequency unsteadiness localized in the vicinity of the oblique shock, thus confirming earlier experimental findings. Furthermore, these oscillations are found to persist even if no long coherent structures are present in the incoming turbulent boundary layer. Wall pressure data are analyzed by means of Fourier analysis, highlighting the low-frequency phenomenon in the interaction region. Furthermore, the flow dynamics are analyzed using a Dynamic Mode Decomposition which shows the presence of a low-frequency mode associated with the pulsation of the separation bubble and accompanied by a forward-backward motion of the shock. The performed analysis leads us to conclude that embedded incoming turbulent structures cannot represent the driving mechanism for the low-frequency motion of the shock. The observed shockwave/turbulent boundary layer interaction phenomenon is therefore a consequence of the inherent dynamics between recirculation region and shock.

Contents

Abstract	iii
1. Introduction	1
1.1. Motivation	1
1.2. Introduction to the SWTBLI phenomenon	4
1.2.1. Description of the SWTBLI phenomenon	4
1.2.2. Low-frequency unsteadiness	7
1.3. Objective of the present work	10
2. Numerical approach	11
2.1. Governing equations	11
2.2. Large-eddy simulation	12
2.2.1. The filtering procedure	13
2.2.2. Explicit LES approach	13
2.2.3. Implicit LES approach	15
2.3. Boundary conditions	26
2.3.1. Turbulent inflow boundary condition	26
2.3.2. Conservative Immersed Interface Method	28
2.3.3. Implementation	36
3. Numerical approach validation	39
3.1. ALDM for compressible wall bounded flows	39
3.2. Supersonic turbulent channel flow	40
3.2.1. Problem setup	40
3.2.2. Flow description	42
3.2.3. Turbulence statistics	42
3.3. Supersonic turbulent boundary layer flow	48
3.3.1. Numerical method	48
3.3.2. Problem setup	48
3.3.3. Flow description	49
3.3.4. Turbulence statistics	51
3.4. CIIM validation cases	58
3.4.1. Steady flow over a circular cylinder at $Re_D = 40$	58
3.4.2. Unsteady flow past a circular cylinder at $Re_D = 100$	62
3.4.3. Vortex induced vibration of a 2-D elastically mounted cylinder	62

3.4.4.	Laminar boundary layer flow over a compression corner at $Ma = 6.06$	66
3.4.5.	Laminar cavity flow at $Ma = 8.9$	67
4.	Compression-Expansion corner flow	73
4.1.	Flow configuration	73
4.2.	Experimental setup	74
4.3.	Numerical setup	74
4.4.	Incoming supersonic turbulent boundary layer	77
4.5.	Time-averaged flow characteristics	79
4.5.1.	Wall pressure and skin-friction coefficient	79
4.5.2.	Comparison of mean velocity profiles	82
4.5.3.	RMS profiles comparison	85
4.5.4.	Görtler-like vortices	85
4.5.5.	Turbulence evolution	89
4.6.	Shock-system features	94
5.	Analysis of the unsteady shockwave behavior	99
5.1.	Wall pressure data analysis	99
5.2.	Dynamic Mode Decomposition	101
6.	Conclusions	109
	Appendix	111
A.	Dynamic Mode Decomposition	113
A.1.	General description	113
A.2.	Matlab script for Dynamic Mode Decomposition	116
A.3.	Validation example	119
	Bibliography	123

List of Figures

1.1.	Shock system description during a free-shock separation state.	2
1.2.	Shock system description during a restricted-shock separation state. .	2
1.3.	Schematic of the unsteady motion of the incipient separation front and reattachment line during RSS flow configuration with a single separation bubble. Azimuthal variations cause asymmetric pressure distributions and ultimately result in off-axis side loads.	3
1.4.	Schematic representation of the wall pressure evolution for the inviscid flow case, the viscid interaction without separation and the shock-induced separated flow. The points S and R represent possible separation and reattachment locations of the shear layer, respectively. The interaction length L_{int} is defined as the distance between the inviscid impingement location X_0 and the intersection of the upstream pressure p_1 with the extrapolation of the quasi-linear part of the wall pressure distribution.	5
1.5.	Sketch of the oblique shock/boundary-layer interaction with separation.	6
1.6.	Sketch of the compression ramp interaction with separation.	7
2.1.	Time-averaged ALDM weight functions for central deconvolution of the streamwise and wall-normal velocity component. Implicit LES of supersonic turbulent channel flow at $Re_\tau = 450$	22
2.2.	(a) Decomposition of the total shear stress τ_T . (b) Decomposition of the total heat flux q_T	23
2.3.	Effective van Driest damping for the implicit LES of a supersonic turbulent channel flow at $Re_\tau = 450$, — damping functional used with ALDM (parameters value $s = 1/3$, $d = 3$, $a^+ = 50$) and --- linear approximation $0.02 y^+$	24
2.4.	Effective coherent-structure damping for the implicit LES of a supersonic turbulent channel flow at $Re_\tau = 450$, — damping function and --- analytical approximation in the vicinity of the wall $(y/H)^{3/2}$	25
2.5.	Two dimensional schematic of conservative discretization for a cut cell.	29
2.6.	Local reference system for a cut cell.	31
2.7.	Two-dimensional description of the interpolation.	32
2.8.	Two dimensional description of the mixing procedure.	35

3.1.	Instantaneous flowfield obtained from the supersonic turbulent channel flow DNS. (center) Q-criterion iso-surface colored with streamwise velocity. (top) Instantaneous temperature field in the $x - y$ and $y - z$ plane. (bottom) Temperature fluctuations in the $x - z$ plane at $y^+ \approx 10$.	43
3.2.	DNS results comparison.(a) Mean van-Driest scaled velocity $\langle u_{1,VD}^+ \rangle$, (b) mean wall normal velocity $\langle u_2 \rangle$, (c) mean temperature $\langle T \rangle$, (d) mean Mach number $\langle Ma \rangle$.	45
3.3.	DNS results comparison. Velocity fluctuations.	45
3.4.	Mean van-Driest transformed velocity $\langle u_{1,VD}^+ \rangle$ for the LES of a supersonic turbulent channel flow at $Re = 4880$ and $Ma = 3.0$. (a) L1 grid. (b) L2 grid.	46
3.5.	(a)-(b) Streamwise, wall normal and spanwise velocity fluctuations for the L1 grid (left) and L2 grid (right). (c)-(d) Turbulent shear stress.	46
3.6.	Turbulent heat flux for the L1 grid (a) and L2 grid (b).	47
3.7.	Contribution of the sub-grid scale term to the global shear-stress balance (a) and to the total heat flux (b) for the L2 grid configuration.	47
3.8.	(a) Instantaneous velocity fluctuations at $y^+ \approx 10$. (b) Instantaneous velocity fluctuations at $y^+ \approx 100$.	50
3.9.	Instantaneous flowfield obtained from the L4 grid using the ALDM-CS formulation. (center) Q-criterion iso-surface colored with streamwise velocity. (top) Instantaneous temperature field in the $x - y$ and $y - z$ plane. (bottom) Temperature fluctuations in the $x - z$ plane at $y^+ \approx 10$.	51
3.10.	Incompressible skin-friction coefficient $C_{f_{inc}}$ as a function of the Reynolds number based on incompressible momentum thickness $Re_{\theta_{inc}}$. (---) Blasius, (----) Smits, (.....) Kármán-Schoenherr. (○) [Pirozzoli and Bernardini, 2011] ($Ma = 2$), (■) ($Ma = 2.5$) [Guarini et al., 2000], (◆) ($Ma = 2.25$) [Pirozzoli et al., 2004], (●) ($Ma = 3.0$) [Maeder et al., 2001]. (a) Comparison between the different LES formulations with the L1 grid. (b) Grid sensitivity study.	53
3.11.	Mean van-Driest transformed streamwise velocity $\langle u_{1,VD}^+ \rangle$ as a function of y^+ . (----) linear-law. (----) logarithmic-law $\log(y^+)/0.41+5.25$. (a) Comparison between the different LES formulations with the L1 grid. (b) Grid sensitivity study.	54
3.12.	Mean averaged mass flux $\langle \rho u_1 \rangle$ and temperature $\langle T \rangle$. (a) Comparison between the different LES formulations with the L1 grid. (b) Grid sensitivity study.	54
3.13.	Reynolds stresses. (a) Comparison between the different LES formulations with the L1 grid. (b) Grid sensitivity study.	55
3.14.	Streamwise velocity u_1 skewness. (a) Comparison between the different LES formulations with the L1 grid. (b) Grid sensitivity study.	56
3.15.	Temperature T skewness. (a) Comparison between the different LES formulations with the L1 grid. (b) Grid sensitivity study.	56
3.16.	Computational domain for the flow over a circular cylinder.	59

3.17. Computational grid for the flow over a circular cylinder at $Re = 40$, $n = 40$. In the local zoomed region every 5 th line is shown.	60
3.18. Streamwise velocity and streamlines for the flow over a circular cylinder at $Re_D = 40$	60
3.19. Pressure coefficient C_p along the surface of a circular cylinder at $Re = 40$ ($\theta = 0$ in the stagnation point; \circ : experimental data Grove et al. [Grove et al., 1998], $---$: numerical computation using body-fitted from Tseng and Ferziger [Tseng and Ferziger, 2003], $—$: present method, $n = 80$).	61
3.20. $— \circ$ Error in C_D for the flow past a circular cylinder at $Re_D = 40$	61
3.21. Streamwise velocity and streamlines for the flow over a circular cylinder at $Re_D = 100$	63
3.22. (a) System description. (b) $—$ Time history of the cylinder vertical position for the following parameters setting: $M_{red} = 2$, $U_{red} = 4$	65
3.23. Instantaneous z -vorticity contour in the vicinity of the cylinder and streamlines for the following parameters setting: $M_{red} = 2$, $U_{red} = 4$	65
3.24. Maximum amplitude variations for the CURVIB method of [Borazjani et al., 2008] ($—\square$) and for the immersed interface method ($---\circ$: $n = 50$, $---\triangle$: $n = 25$.)	66
3.25. Computational box for the laminar boundary layer over a compression corner.	67
3.26. Pressure contours and streamlines showing the recirculation region for the adiabatic wall case.	68
3.27. Pressure distribution along the ramp surface.(a) Adiabatic wall case: • Experimental data [Lewis et al., 1968]; level 1 grid $---$; level 2 grid $—$. (b) Isothermal wall case: • Experimental data [Lewis et al., 1968]; level 1 grid $---$; level 2 grid $—$	68
3.28. Computational domain for the cavity and the region external to the body of revolution. The body of revolution is described by the zero levelset contour line.	70
3.29. Detail of the computational grid in the cavity region. Each 20 th line is shown.	70
3.30. Instantaneous representation of the flow by the Schlieren-type visualization. (a) The computed density gradient magnitude $\ \nabla\rho\ $ and (b) experimental Schlieren visualization [Jackson et al., 2001].	71
3.31. Computed local Mach number profile at $x/D = 7.6$. $----$ level 1 grid; $—$ level 2 grid; \circ numerical reference data [Jackson et al., 2001].	71
3.32. Cavity streamlines pattern. The flow over the cavity is from left to right and the main cavity vortex has a clockwise circulation.	72
3.33. (a) Surface pressure distribution. (b) Surface heat transfer distribution. $----$ level 1 grid; $—$ level 2 grid; \circ experimental reference data [Jackson et al., 2001].	72
4.1. Main flow phenomena of the compression-expansion ramp flow.	75

4.2.	Global view of the compression-expansion ramp flow. (left) Temperature field. (middle) turbulent structures visualized by means of Q-criterion isosurface, together with the shock visualized as pressure isosurface. (right) streamwise velocity fluctuations in the vicinity of the wall.	75
4.3.	Experimental test model.	76
4.4.	Experimental measurement sections for the large (a) and small (b) model.	76
4.5.	Computational domain of the present LES.	78
4.6.	Computational grid of the present LES (not every line is shown). — Subdomain adopted for the incoming turbulent boundary layer computation.	78
4.7.	(a) Friction coefficient evolution in the streamwise direction — . $E1$ section location ---- . (b) Wall normal distribution of the mean flow for the incoming boundary layer at the station $E1$. Mach number (LES --- , experiment \circ); temperature (LES , experiment \square); velocity (LES — , experiment \diamond); density (LES ---- , experiment \triangle).	80
4.8.	Distribution of the two-point correlations in the spanwise direction at $x/\delta_0 = 11.95$ and $y^+ \approx 150$. — $\alpha = u_1$; ---- $\alpha = u_2$; -.- $\alpha = u_3$; $\alpha = \rho$.	80
4.9.	(a) Van-Driest transformed mean-velocity profile at the station $E1$. \square , experimental (computed using the skin-friction coefficient C_f measured in the experiment). — , LES. -.-, linear law. ---- , log-law $\log(y^+)/0.4 + 5.25$. (b) Turbulence statistics at the station $E1$. Lines denote LES data shown in inner-layer scaling using the compressibility correction of [Huang et al., 1995] and symbols represent DNS data of [Spalart, 1988]. — $\langle u'_1 u'_1 \rangle$; — $\langle u'_2 u'_2 \rangle$; — $\langle u'_3 u'_3 \rangle$; — $\langle u'_1 u'_2 \rangle$	81
4.10.	Friction coefficient dependence on Re_{δ_2} . \blacktriangle , LES. \blacksquare , experiment. ∇ , Stalmach CAT5802 ($M_\infty = 2.75$). \diamond , Laderman & Demetriades CAT7702 ($M_\infty = 3.0$). \triangle , Maier CAT7003 ($M_\infty = 2.9$). \diamond , Mabey et al. CAT7402 ($M_\infty = 2.8$). \circ , Mabey et al. CAT7402 ($M_\infty = 3.0$). — Kármán-Schönerr $C_f - Re_{\delta_2}$ correlation.	81
4.11.	(a) Averaged wall-pressure and (b) skin-friction coefficient distributions in the streamwise direction. \circ , reference experiment; — current LES averaged in time and over the spanwise direction. Symbols S and R indicate the mean separation and reattachment points.	83
4.12.	Velocity profiles at stations E1-E13. \circ , reference experiment; — current LES averaged in time and over the spanwise direction. ---- Maximum values along the spanwise direction. ---- Minimum values along the spanwise direction.	84
4.13.	Root-mean-square profiles of the velocity (a) and density (b) fluctuations at stations T1-T4. \circ , reference experiment; — current LES averaged in time and over spanwise direction. ---- Maximum values along the spanwise direction. ---- Minimum values along the spanwise direction.	86

-
- 4.14. Instantaneous snapshot of u'_t/U_∞ at $y^+ \approx 12$. Symbols **S** and **R** indicate the mean separation and reattachment points. 87
- 4.15. (a) Isosurface of streamwise vorticity. The clockwise rotation is represented by the blue color. Anti-clockwise rotation is given in the red color. (b) Sketch of the main features characterizing the Görtler vortices. 87
- 4.16. Distribution of the mean skin-friction coefficient at the wall in the spanwise direction. — , averaged in time; ---- , averaged in time and over spanwise direction. 88
- 4.17. (a) Numerical surface streamlines pattern. Contours of the time averaged local friction coefficient are shown. The thick solid line indicates the location of $\langle C_f \rangle = 0$ where the boundary layer reattaches. (b) Oil-flow visualization from the experiment [Zhel'tovodov and Yakovlev, 1986]. The thick dashed line indicates the position of the corner. 90
- 4.18. (a) Streamwise velocity fluctuation $\sqrt{\langle u'_t u'_t \rangle}$, (b) Density fluctuations $\sqrt{\langle \rho' \rho' \rangle}$. ---- Maximum values along the spanwise direction. ---- Minimum values along the spanwise direction. 91
- 4.19. (a) Reynolds normal stress $\tau_{11} = \langle \rho u''_1 u''_1 \rangle$, (b) Reynolds shear stress $\tau_{12} = \langle \rho u''_1 u''_2 \rangle$ and (c) the structure parameter $-\tau_{12}/\tau_{11}$ at measurements sections. ---- Maximum values along the spanwise direction. ---- Minimum values along the spanwise direction. 93
- 4.20. Reynolds stress anisotropy invariant map evaluated at different stations. (a) station $E1$ $x/\delta_0 = -8.05$, (b) station $E3$ $x/\delta_0 = -2.93$, (c) station $E7$ $x/\delta_0 = 3.05$, (d) station $E10$ $x/\delta_0 = 7.56$, (e) station $E11$ $x/\delta_0 = 12.20$, (f) station $E13$ $x/\delta_0 = 19.25$. The color map indicates the distance from the wall y/δ_0 95
- 4.21. Instantaneous representation of the flow by the Schlieren-type visualization. The computed density gradient averaged in spanwise direction $\|\nabla\rho\|$ (a) and experimental Schlieren visualization (b). 96
- 4.22. Instantaneous snapshot of $\|\nabla p\|$ at $y/\delta_0 \approx 0.1$. The dashed line indicates the mean shock location. 97
- 5.1. (a) Wall-pressure signals and (b) corresponding weighted power spectral density at different streamwise locations relative to the ramp corner. 100
- 5.2. Contours of the weighted power spectral density of wall-pressure in the $St-x/\delta_0$ -plane. The power spectral density is normalized such that their integral over frequency is unity. Thirty contours levels have been used; the dashed vertical lines indicate the location of the separation S and reattachment point R respectively. The solid line indicates the position of the corner CC 101
- 5.3. (a) Close-up view of the eigenvalue distribution of the inter-snapshot mapping in the complex plane, detected by the DMD method. (b) Amplitude distribution of the detected modes. 103
- 5.4. Amplitude distribution of the detected modes with decreasing number of snapshots. — $\Delta t U_\infty/\delta_0 = 1$, ---- $\Delta t U_\infty/\delta_0 = 2$, -.- $\Delta t U_\infty/\delta_0 = 3$ 104
-

5.5.	Four snapshots from a reconstruction of the flow fields from a linear combination of the four most dominant dynamic modes. — Instantaneous oblique shock position. ---- Mean oblique shock position. ----- Mean recirculation region domain.	105
5.6.	(a) Temporal evolution of the mass (per unit span) of the reverse-flow region; (b) shock location versus time. Each variable has been extracted from a reconstructed flow-field sequence based on the four most dominant dynamic modes.	107
6.1.	(a) Contours of the amplitude of the superimposition of the four most dominant modes. (a) streamwise velocity u_1 (20 contours ranging from 0.005 to 0.065). (b) density ρ (20 contours ranging from 0.005 to 0.15).	111
A.1.	Snapshot from the flame visualization database.	120
A.2.	DMD spectrum for the flame visualization example. (a) Time-stepper spectrum visualization. The color and symbol size of the eigenvalues indicate the coherence of the associated dynamic modes. (b) amplitudes distribution with respect to the frequency. The spectrum is symmetric since the post-processed data is not complex.	120
A.3.	Spatial distribution of the first four most dominant dynamic modes. .	121

List of Tables

3.1. Lines and symbols for the different cases.	41
3.2. Grid adopted for the resolutions study.	41
3.3. Mean flow variables.	41
3.4. Digital-Filter procedure parameters.	48
3.5. Lines and symbols for the different cases.	49
3.6. Grid resolutions study using ALDM-CS.	49
3.7. Grid sizes and number of points n along the diameter.	59
3.8. Steady flow past a circular cylinder at $Re_D = 40$	62
3.9. Grid sizes and number of points n along the diameter.	62
3.10. Unsteady flow past a circular cylinder at $Re_D = 100$	63
3.11. Grid details for the vortex induced vibration test case.	64
3.12. Grid details for the hypersonic compression corner flow test case. Total number of cells N_p and cells for incoming boundary layer thickness n_{δ_0}	67
3.13. Computed laminar boundary layer data at $x/D = 7.6$	69
4.1. Streamwise location of the measurement stations.	77
4.2. Summary of mean-flow parameters for the flat-plate boundary layer simulation.	79

1. Introduction

1.1. Motivation

Modern rockets, under the competing demands of cost and performance, are typically designed to achieve high thrust-to-weight ratios. This objective is often pursued using high area ratio, reduced length nozzles and/or optimized nozzle designs [Östlund and Muhammad-Klingmann, 2005]. While modern nozzles typically provide high in-vacuum performance, during low altitude flight unsteady detachment of the over-expanded supersonic flow within the nozzle can lead to the generation of often dangerous nozzle side loads [Summerfield et al., 1954, Sunley and Ferriman, 1964, Nave and Coffey, 1973, Dumnov, 1996, Frey and Hagemann, 1999, Brown et al., 2002]. The detrimental and sometimes catastrophic effects of these loads have been documented, for example, in J2, SSME Block I, Ariane-5, Chinese CZ-3B, Fastrac, Vulcain, and Japanese H-II and LE-7 engines [Nave and Coffey, 1973, S, 1996, Newman, 2001, Wang, 2004]. In large engines, side loads can reach extreme magnitudes, for example, of the order of $10^3 kN$ in Apollo Saturn V rockets [Brown et al., 2002].

Such phenomena take place during the transient startup and shutdown of rocket nozzles, when off-axis forces are triggered by unsteady internal flow separation, and are occasionally enhanced by unsteady flow reattachment. The asymmetry of the internal flow structures is responsible for the generation of a net lateral force, generally defined as side load. Depending on the nozzle contour and the nozzle pressure ratio, the overall features concerning the nature and location of the separated flow and shock structure features different states.

In the case of a thrust-optimized parabolic (TOP) nozzle, during the transient startup and shutdown of phases, the flow states can be classified into two categories: free shock separation (FSS) and restricted shock separation (RSS), as sketched in Fig. 1.1 and Fig 1.2. The schematics of these processes are given in the models proposed from by [Frey and Hagemann, 2000, Hagemann et al., 2002, Verma and Haidn, 2009].

The free-shock separation occurs at low values of nozzle pressure ratio (NPR) (defined as the ratio between the stagnation pressure p_0 and the back pressure p_{out}). The flow configuration that is achieved in the FSS state is characterized by an incipient separation of the flow, which is triggered by an adverse pressure gradient between the region of isentropic expansion and the subsonic entrainment region. Compression waves, originating from within the turbulent boundary layer, coalesce to form a separation shock in the outer regions of the flow. This separation shock interacts

1. Introduction

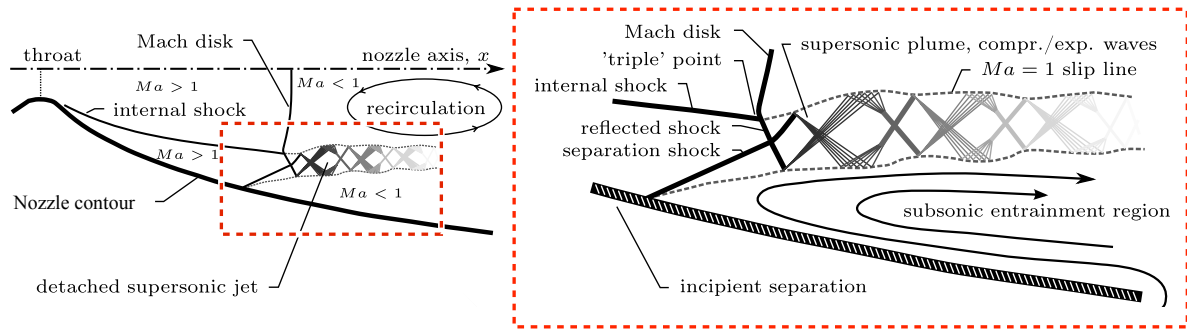


Figure 1.1.: Shock system description during a free-shock separation state.

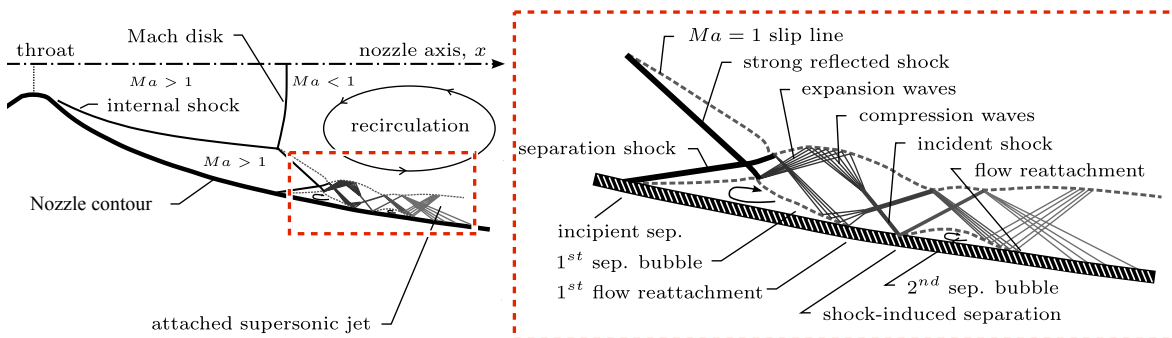


Figure 1.2.: Shock system description during a restricted-shock separation state.

with the reflected shock that originates at the so-called "triple" point, where the Mach disk, internal shock, and reflected shock coincide. A separated region encompassing a series of compression and expansion waves is located downstream of the shocks. When the NPR is increased in the nozzle, the flow configuration transitions to a restricted-shock separation state. The incipient separation point is now located further downstream with respect to the interaction point of the internal shock and Mach disk. The strong shock originating from this interaction eventually induces an outward radial motion of the fluid that reattaches the supersonic plume to the wall. A bounded region of separated flow is now formed in between the separation shock and an expansion fan reflecting from the shear layer of the supersonic plume, further referred to as an annular separation bubble. Depending on the NPR, the annular supersonic jet might remain attached to the wall. However, it is believed that if the initial shocks (labeled as separation shock and strong shock in inset of Fig. 1.2) are sufficiently strong, a shock (indicated as incident shock) is generated which can separate the flow from the inner wall again through a shockwave turbulent boundary-layer interaction (SWTBLI) phenomenon. The flow might reattach further downstream, thereby creating a second separation bubble. Concerning the

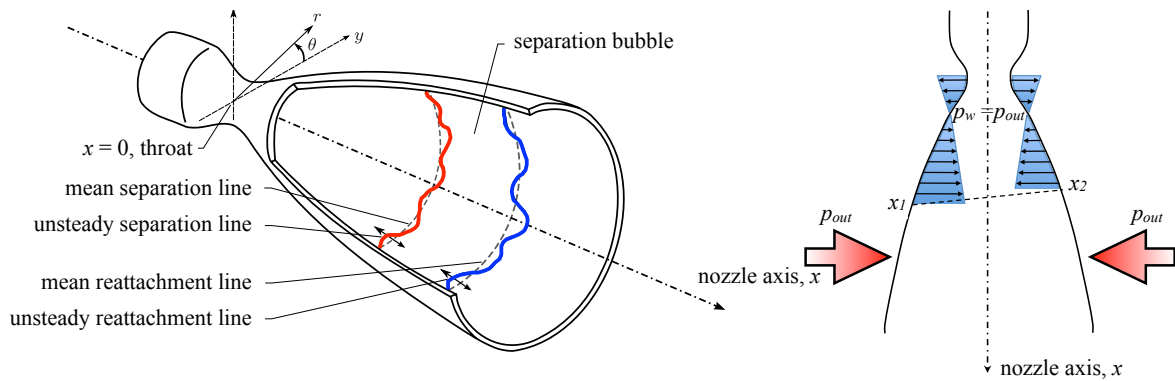


Figure 1.3.: Schematic of the unsteady motion of the incipient separation front and reattachment line during RSS flow configuration with a single separation bubble. Azimuthal variations cause asymmetric pressure distributions and ultimately result in off-axis side loads.

static wall pressure, a pressure increase above ambient conditions occurs in the separated regions. After the reattachment, the flow expands and the pressure decreases up to the second separation point. Finally, upon further increases in NPR, the RSS structure returns to a FSS state with an entrainment flow region that eventually vanishes once the nozzle flows full.

The works of [Ruf et al., 2009, Hagemann et al., 2002] have highlighted that the highest value for the side loads is achieved during the phase in which the shock-system transitions from the FSS state to the RSS and viceversa. Furthermore, [Östlund et al., 2004] highlighted that additional sources of side load disturbances are linked to wall pressure fluctuations in the separated regions of the nozzle. Computational models have also been proposed to provide a deeper insight into the source of the side loads during the full duty cycle of a rocket engine. [Chen and Chakravarthy, 1994, Deck and Guillen, 2002, Schwane and Xia, 2005, Wang, 2009] used an unsteady, compressible RANS simulation to investigate the evolution of the separated region. Even if the findings from these computational efforts appear to coincide with the experimental observations, the details of the mechanisms governing the interaction zone remain still unknown. With only a fraction of these simulations having accounted for the modern advancements in computational modeling, comprehensive quantitative datasets are still not allowing for an extension of the predictions to more realistic conditions which do not allow for a direct experimental investigation.

The fluctuating nature of the surface pressure signal is a direct consequence of unsteady pulsations of the shock structure and separated flow during both FSS and RSS states. The unsteadiness of the FSS and RSS flow structures is illustrated in Fig. 1.3. The incipient separation front and reattachment line (which is present only in the case of RSS) are identified in this illustration and are characterized by an unsteady motion along the azimuthal direction. The resulting unsteady wall pressure distribution varies along the same direction and asymmetries in such distribution with

respect to the nozzle axis generate an off-axis force. The modification of the pressure distribution with respect to time constitutes the direct source of side load activity. This motions originate directly from the intrinsic unsteadiness of the SWTBLI phenomenon. In the experimental study of [Baars et al., 2012], both RSS and FSS configurations are investigated by means of dynamic wall pressure measurements and response moments of the nozzle/strain tube assembly. The spectral analysis of their pressure data for the FSS condition has revealed two distinct peaks for the pressure probe located near the separation shock. The first lower frequency peak is found to be directly connected to the typical low-frequency unsteadiness that characterizes the SWTBLI, while the second peak comprised more broadband high-frequency noise that grew in energy with increasing distance downstream. The main aim of the present work is to investigate the SWTBLI phenomenon in order to gain a deeper insight into the mechanism that leads to the origin of the so called low-frequency shock unsteadiness.

1.2. Introduction to the SWTBLI phenomenon

1.2.1. Description of the SWTBLI phenomenon

The basic interaction types most commonly studied between a shockwave and a laminar/turbulent boundary layer are the normal/oblique shockwave interaction and the compression corner flow or the flow over a bump. In this introduction both configuration will be described. In the case of an oblique shock impinging on a flat plate, the inviscid theory states that the shock is reflected in order to maintain wall-parallel flow. The pressure increase, characterized by the Rankine-Hugoniot condition, takes place abruptly at the nominal impingement point within an infinite small extent, see Fig. 1.4. In real flows, where viscosity leads to the formation of a boundary layer at the wall, SWTBLI becomes much more complex leading to greater deviations from the inviscid solution. While weak interactions resemble the inviscid theory, stronger ones induce a separation of the boundary layer and the original shock system comprising simply an incident and reflected shock is replaced by a complex system of interactions. A description of the main phenomena characterizing the interaction between an impinging oblique shock and a supersonic turbulent boundary layer are given in Fig. 1.5. The shock strength of the incident shock C1 and the associated adverse pressure gradient are large enough to cause a separation of the boundary layer. Due to the upstream influence mechanism, the separation takes place well ahead of the nominal impingement point at the location S . The upstream propagation of the adverse pressure gradient imposed by C1 induces compression waves in the supersonic part of the boundary layer, which coalesce to form the reflected shock C2. The reflected shock C2 intersects the incident shock C1 at point I and the original shocks continue traveling as transmitted shocks C3 and C4, respectively. The shock C4 penetrates into the separated dissipative layer while being curved due to the local Mach number variation, and is then reflected at the sonic

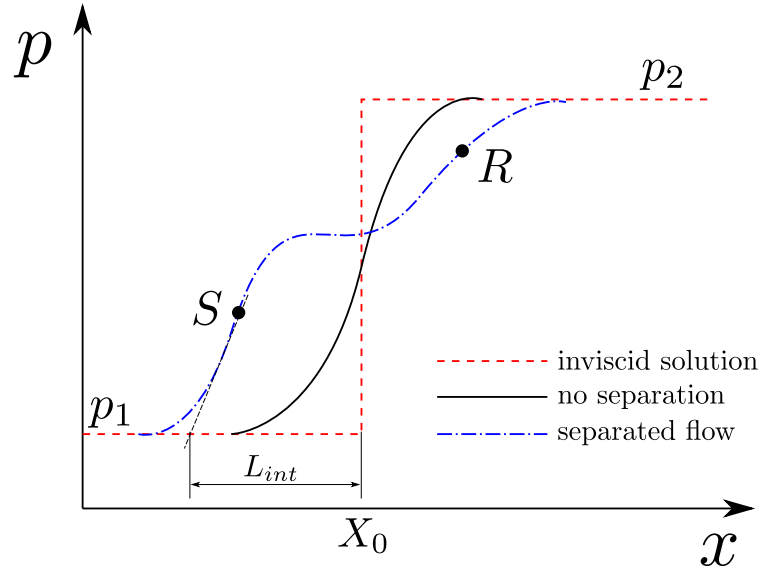


Figure 1.4.: Schematic representation of the wall pressure evolution for the inviscid flow case, the viscid interaction without separation and the shock-induced separated flow. The points S and R represent possible separation and reattachment locations of the shear layer, respectively. The interaction length L_{int} is defined as the distance between the inviscid impingement location X_0 and the intersection of the upstream pressure p_1 with the extrapolation of the quasi-linear part of the wall pressure distribution.

line as a system of centered expansion waves. The expansion fan compensates the pressure increase induced by the impinging shock C_4 , resulting in a pressure plateau within the separated zone, see Fig. 1.4. The separated shear layer is thus deflected in the direction of the wall, where it reattaches at the point R while being continuously decelerated. The compression waves associated with the deceleration process coalesce to form the reattachment shock. Through their DNS of an impinging shock on a $Ma = 2.25$ turbulent boundary layer, [Loginov et al., 2006, Pirozzoli and Grasso, 2006] find that the formation of a mixing layer at the separation bubble edge S is primarily responsible for the amplification mechanism of turbulence. Downstream of the SWTBLI, the boundary layer recovers an equilibrium state. The dividing streamline, which bounds the recirculation zone, originates at the separation point S and ends at the reattachment point R . The mixing layer is responsible for an energy transfer of momentum from the outer high speed flow towards the separation region. Consequently, the velocity on the dividing streamline steadily increases until the reattachment process begins. The ability of the shear layer to overcome a pressure increase associated to the reattachment process is directly influenced by the maxi-

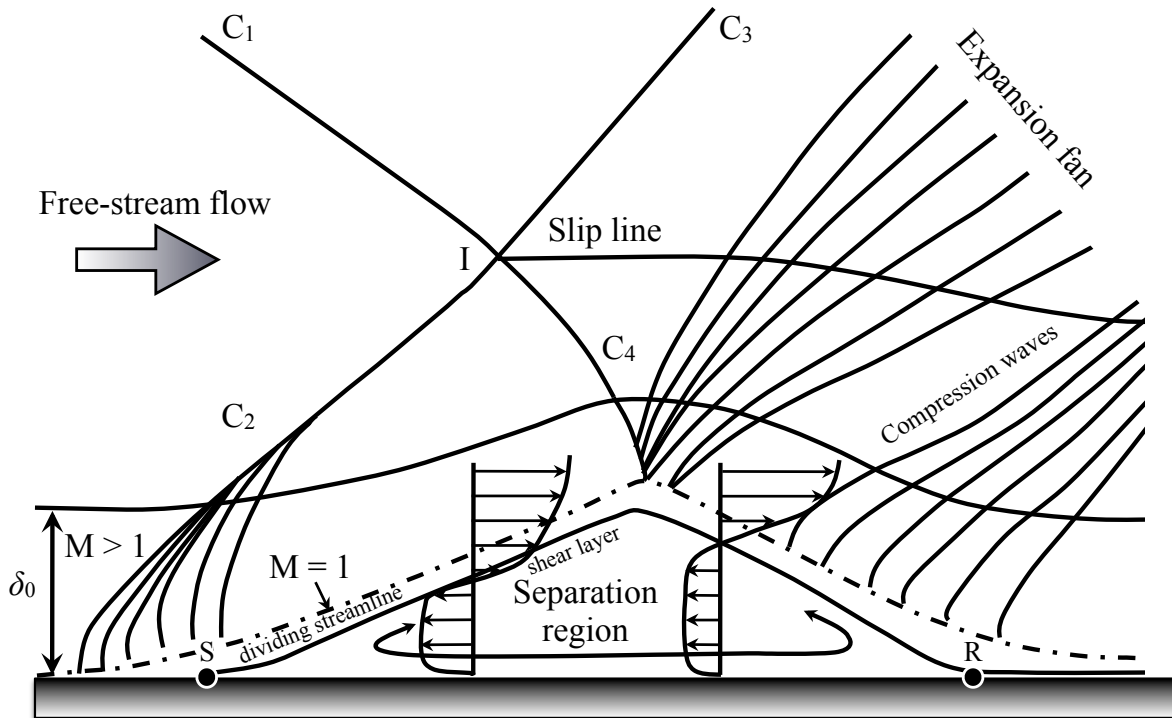


Figure 1.5.: Sketch of the oblique shock/boundary-layer interaction with separation.

imum velocity on this streamline at the onset of reattachment [Delery and Bur, 2000]. This characteristic furthermore explains why the interaction length L_{int} (see Fig. 1.4 for a definition of L_{int}) increases when the shock strength is incremented. As depicted in Fig. 1.4, the pressure increase Δp through the SWTBLI can be decomposed in two parts, namely Δp_1 associated to the separation and Δp_2 accompanied by the reattachment process. [Delery and Bur, 2000] have shown that for the same flow parameters of the incoming boundary layer (especially the shape factor H_{12}), the onset of separation occurs at the same pressure level, consistent with the Free Interaction Theory which states that the pressure rise until separation is only a function of upstream flow conditions. Therefore, an increase in the overall pressure rise Δp goes hand in hand with an increase in Δp_2 . This in turn means, that the fluid particles on the dividing streamline must possess a higher stagnation pressure which can only be achieved by an increase of the shear layer length, allowing entrainment effects to have enough time to provide sufficient momentum transfer from the outer flow when reattachment begins [Delery, 1985].

Figure 1.6 shows a description of the main features of the interaction between oblique shock and supersonic turbulent boundary layer along a compression ramp. Ramp induced interactions lead to a similar organization for the separated flow, with the boundary layer reacting to a pressure rise, no matter the cause of this pressure increase. What changes, in this case, is the shock pattern associated with the interaction. The separation of the boundary layer at point S induces a deflection of the

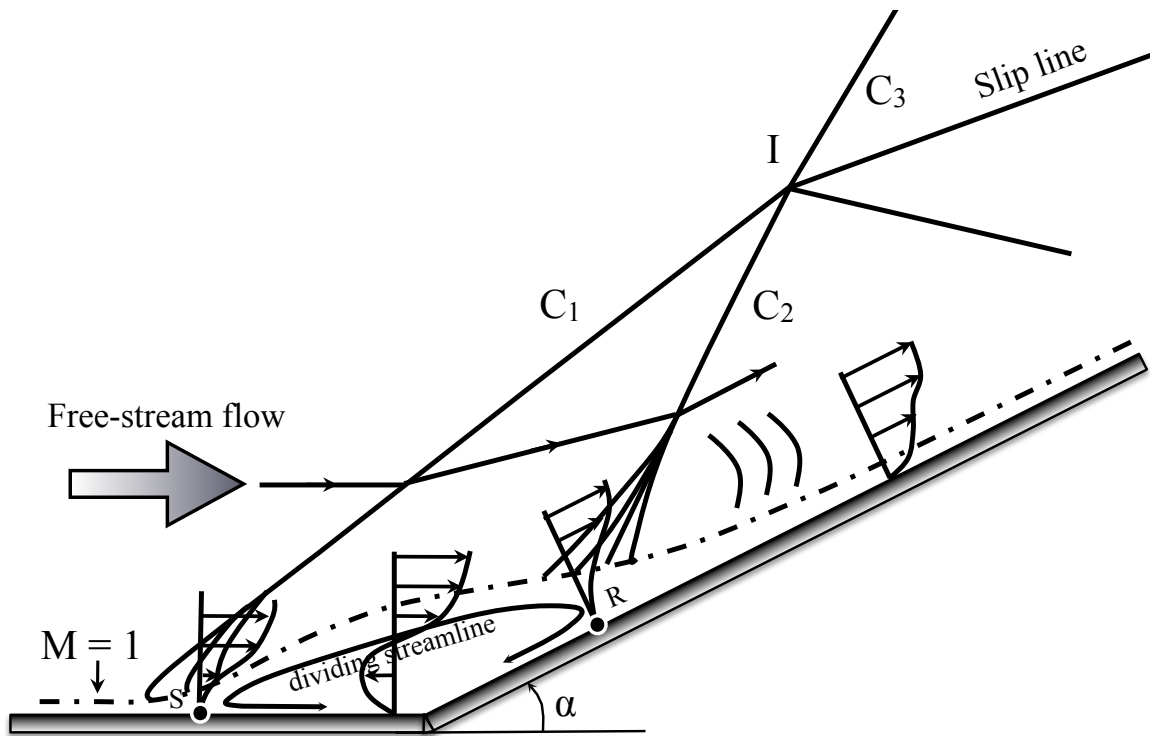


Figure 1.6.: Sketch of the compression ramp interaction with separation.

flow giving rise to the oblique shock C_1 as in the previous cases, the flow behind C_1 being still supersonic. The two shocks C_1 and C_2 meet at the triple point I . Since, the states behind C_1 and C_2 are not compatible with the Rankine-Hugoniot conditions, a third shock C_3 starts from I , leading to a compatible state. Downstream of I , the two states are separated by the slip line.

1.2.2. Low-frequency unsteadiness

The interaction properties described above relate to the steady aspects of the STWBLI, which are well studied and documented. In reality however, the case of a shock induced separated turbulent boundary layer is much more complex as unsteady shock motions of the reflected shock ranging over large spatial and temporal scales occur. Various experimental and numerical studies confirmed the existence of such low-frequency phenomena and identified a characteristic frequency being about two or three orders of magnitude smaller than the characteristic frequency of the incoming boundary layer $\mathcal{O}(U_\infty/\delta_0)$, [Dolling, 2001]. The driving mechanism of such low-frequency shock motions is currently not understood and different theories have been presented. Stated by [Piponniau et al., 2009], a major problem is to separate the low-frequency shock motions associated to the separated flow from the ones related to unsteady conditions of the upstream boundary layer. Basically two main lines of thought can be identified, where on the one hand the unsteadiness is cor-

related with upstream events, while a second group links the the low-frequency motion to an intrinsic feature associated to the dynamics of the separation bubble and the shock motion. [Beresh et al., 2002] suggested that the low-frequency shock motion is inherited by upstream events by means of continuous variations in the upstream velocity profile, which is therefore responsible for the unsteady shock foot motion. Positive velocity fluctuations resemble an instantaneously fuller velocity profile, featuring an increased resistance to separation and hence shifting the separation shock downstream while the separation bubble is passively responding to the shock movement. In order to relate such high-frequency dynamics to the low-frequency shock-motion, the shock can be thought of as a low-pass filter, selectively amplifying the low- frequency motions contained in the upstream boundary layer. This idea has been formally proposed by [Plotkin, 1975], who postulated that the shock displacement was obeying a first-order stochastic ordinary differential equation (ODE) with an associated characteristic time scale. [Plotkin, 1975] has shown that such a mathematical model is capable of reproducing the wall-pressure low-frequency spectrum. However, as stated by [Touber and Sandham, 2010], this model lacks justifications about whether the oblique shock/boundary layer interaction can be modeled so simply and, if so, on the key parameters responsible for the cutoff frequency. In addition it is unclear if the low-energy/low-frequency content of the upstream boundary layer is sufficient to be solely responsible for the low-frequency unsteadiness, once the high frequencies have been cut off. Another approach is to relate the slow timescales of the incoming boundary layer to the unsteady shock movements, which led to investigations of the so-called "superstructures". Indeed, in order to relate the low-frequency unsteadiness of the reflected shock with structures present in the incoming boundary layer, they need to be at least one order of magnitude larger than the associated boundary layer thickness. [Ganapathisubramani et al., 2006] investigated a supersonic boundary layer at $Ma = 2$ by means of particle-image velocimetry (PIV) and Taylor's hypothesis and found elongated coherent structures with a length of about $50\delta_0$. The impact of a structure of such length will inevitably displace the reflected shock, possibly explaining the unsteadiness. They proposed a simple scaling argument for the low-frequency content of such superstructures being $U_\infty/2L_s$, with L_s representing the length of the structure and U_∞ the upstream free stream velocity. Considering the experimental investigations by [Dupont et al., 2006], who created a database for the oblique shock reflection case for different shock intensities, energetically significant low-frequency shock oscillations for the 8° case could be found at frequencies about $U_\infty/(119\delta_0)$. Using the above scaling hypothesis for the superstructures would result in a length of $L_s \approx 60$, consistent with the value reported by [Ganapathisubramani et al., 2006]. Support for this hypothesis is provided by the DNS results of [Wu and Martin, 2007] where long coherent structures with a length of $48\delta_0$ have been found. However, it should be noted that the appearance of such structures could be related to the recycling/rescaling technique used in their work for the turbulent inflow generation, probably forcing such structures. In addition, different experimental studies with same inflow conditions but different corner and wedge angles [Dolling, 2001, Dus-

saugé et al., 2006, Dupont et al., 2006, Piponniau et al., 2009], have shown that the low-frequency shock motion changed markedly. Unless the shock truly acts as a low-pass filter, the above mentioned investigations make the superstructures theory questionable. The other line of thought states the low-frequency shock motions to be deriving from a coupling effect between the dynamics of the separation bubble and the shock movements, either through global instability of the separation bubble or through some mechanism of self-sustainment. As mentioned before, [Dupont et al., 2006] measured the characteristic low-frequencies of the shock motion for an oblique shock impinging on a $Ma = 2.3$ turbulent boundary layer for various wedge angles varying between $7^\circ < \theta < 9.5^\circ$ and found that for an identical incoming boundary layer the shock frequency is directly related to the shock intensity. Based on the interaction length L_{int} and free stream velocity U_∞ , they stated the Strouhal number $St_L = fL_{int}/U_\infty$ to lie in between $0.02 < St_L < 0.04$. The idea that vortical structures originating from the shear layer which forms in the vicinity of the reflected shock could interact with the separation bubble has been extensively studied by [Piponniau et al., 2009]. They proposed a model based on the mass-entrainment timescale from the mixing layer, whose timescale could be related to those of the low-frequency shock motions. Moreover, they showed a coupling between the breathing motion of the separation bubble and the excursion of the reflected shock. While contractions of the bubble are related to downstream motion of the reflected shock, expansions result consequently in an upstream shift. Low-frequency self-sustained oscillations have numerically been supported by [Touber and Sandham, 2009], who analyzed the stability of the SWTBLI by considering the linearized Navier-Stokes equations about the base flow associated to the full LES. Their main result was the proof of existence of a two-dimensional, non-oscillatory but globally unstable mode, whose growth rate was found to be significantly smaller than the typical time scales of the incoming boundary layer. In addition, using standard and non-standard modal decomposition, [Pirozzoli et al., 2010b] found the occurrence of two distinct flow modes, one associated with the turbulence structures in the incoming boundary layer, the other associated with a cyclic breathing motion of the separation bubble, hence resulting in a fore-and-aft motion of the reflected shock. Another theory for self-sustained low-frequency unsteadiness based on an acoustic feedback mechanism has been proposed by [Pirozzoli and Grasso, 2006]. Based on their DNS of an impinging shock at $Ma = 2.25$ and $Re_{\delta_2} = 3725$, they proposed an acoustic feedback mechanism in the interaction region being responsible for the self-sustained low-frequency oscillations of the reflected shock. Large coherent structures are shed in the vicinity of the mean separation location and are convected along the detached shear layer towards the tip of the incident shock. The unsteady interaction of such vortical structures with the incident shock tip produces acoustic waves that propagate upstream within the subsonic part of the boundary layer, affecting the position of the separation point and enhancing the shedding of coherent structures. [Touber and Sandham, 2009] detected upstream acoustic waves within the interaction region, confirming the possibility of the feedback-loop mechanism proposed by [Pirozzoli and Grasso, 2006].

1.3. Objective of the present work

Given the elements proposed in the presented discussion, it becomes clear that shock-wave/turbulent boundary layer interaction, and in particular the associated low-frequency unsteadiness, is still a very active field of research where no exhaustive description of this phenomenon has been reached yet. The following work intends to give a deeper insight in the SWTBLI, using large-eddy simulation as the primary tool to generate the data that is then analyzed by means of modal analysis.

In particular we will:

- Validate the proposed LES approach through sensitivity studies and comparisons with direct numerical simulation data.
- Validate the conservative immersed interface method introduced to handle complex geometries in a cartesian-grid based code.
- Perform a global validation of the different parts of the numerical approach by direct comparison with experimental results.
- Investigate the low-frequency unsteadiness phenomenon of the SWTBLI by mean of Dynamic Mode Decomposition.

The thesis is organised as follows. The next chapter will introduce the governing equations with a focus on the 3D compressible Navier-Stokes equations and the numerical approach proposed for the large-eddy simulation. In addition, the so called conservative immersed interface method (CIIM) for compressible viscous flows will be introduced. The following chapter will be devoted to the validation of the single building blocks of the numerical approach proposed, namely: the implicit large-eddy simulation approach, the digital-filter technique for the generation of the turbulent inflow profiles and the CIIM for the description of embedded boundaries. From there, the following chapter will focus on the analysis of the results of a large-eddy simulation of the flow of a supersonic turbulent boundary layer along a compression-expansion ramp. The results will be directly compared with experimental measurements derived from the work of [Zheltovodov et al., 1990]. The next chapter will be devoted to the analysis of the low-frequency unsteadiness of the shock motion. The proposed approach makes use of the numerical database generated in the previous validation step, which will be analyzed by mean of Dynamic Mode Decomposition (DMD). Finally, a discussion about the low-frequency motion, based on the knowledge acquired from both the large-eddy simulation and the DMD analysis will be provided, followed by the conclusions and some suggestions for future work.

2. Numerical approach

This chapter describes the numerical approach that was implemented in order to perform the simulations presented throughout this dissertation. In particular, the large-eddy simulation technique used in this work will be detailed together with the approach implemented for generation of the incoming turbulent-boundary-layer fluctuations. Furthermore, the conserved immersed interface technique, used to describe embedded boundaries in the cartesian-grid based code adopted in this work, will also be presented.

2.1. Governing equations

We consider the compressible Navier-Stokes equations in a dimensionless form :

$$\frac{\partial \rho}{\partial t} + \frac{\partial \rho u_i}{\partial x_i} = 0, \quad (2.1)$$

$$\frac{\partial \rho u_i}{\partial t} + \frac{\partial \rho u_i u_j}{\partial x_j} = -\frac{\partial p}{\partial x_i} + \frac{1}{Re} \frac{\partial \tau_{ij}}{\partial x_j}, \quad (2.2)$$

$$\frac{\partial \rho E}{\partial t} + \frac{\partial \rho E u_j}{\partial x_j} = -\frac{\partial p u_j}{\partial x_j} + \frac{1}{Re} \frac{\partial \tau_{ij} u_j}{\partial x_j} + \frac{1}{(\gamma - 1) Re Pr Ma^2} \frac{\partial}{\partial x_j} \left(\kappa \frac{\partial T}{\partial x_j} \right), \quad (2.3)$$

where t and x_i represent the time and the spatial coordinates of a Cartesian reference system, respectively. The above dimensionless equations represent the continuity, momentum and energy equation and have been derived by considering the dimensional Navier-Stokes equations and normalizing all flow parameters with the following reference values:

$$u_i = \frac{u_i^*}{U_\infty^*}, \quad \rho = \frac{\rho^*}{\rho_\infty^*}, \quad T = \frac{T^*}{T_\infty^*}, \quad (2.4)$$

$$p = \frac{p^*}{\rho_\infty^* U_\infty^{*2}}, \quad E = \frac{E^*}{U_\infty^{*2}}, \quad x_i = \frac{x_i^*}{L_{ref}^*}, \quad (2.5)$$

$$t = t^* \frac{U_\infty^*}{L_{ref}^*}, \quad (2.6)$$

where the variables marked with a star (*) represent dimensional quantities. The governing flow parameters which appear in the system of equations after the non-dimensionalization process are the Reynolds number Re , the Prandtl number Pr , the Mach number Ma and the specific heat ratio γ .

2. Numerical approach

In Eq. (2.3) u_i denotes the single component of the velocity vector and τ_{ij} represents the viscous stress tensor for a Newtonian fluid

$$\tau_{ij} = \mu(T) \left(\frac{\partial u_i}{\partial x_j} + \frac{\partial u_j}{\partial x_i} - \frac{2}{3} \delta_{ij} \frac{\partial u_k}{\partial x_k} \right). \quad (2.7)$$

The Navier-Stokes system of equations is closed by constitutive relations for pressure p , temperature T , viscosity μ and diffusivity k . In the numerical examples presented in this work we consider a perfect gas with the ratio of specific heats γ assumed to be equal to 1.4. For an ideal gas the pressure p and the temperature T are determined by the definition of total energy

$$p = (\gamma - 1) \left(E - \frac{1}{2} \rho u_i^2 \right), \quad (2.8)$$

$$T = \frac{p}{R\rho}, \quad \text{with } R = \frac{1}{\gamma Ma^2}. \quad (2.9)$$

The temperature dependence of the viscosity is given either by a power-law or by the Sutherland's law

$$\mu(T) = \begin{cases} \frac{1}{Re} T^\psi \\ T^{1.5} \frac{1+N}{T+N} \text{ with } N = \frac{S}{T_a^*}, S = 110.4K \end{cases}. \quad (2.10)$$

The thermal conductivity is computed from the viscosity using the following relation

$$\kappa = \frac{1}{(\gamma - 1) Ma^2 Pr} \mu(T). \quad (2.11)$$

2.2. Large-eddy simulation

Direct Numerical Simulation (DNS) suffers from the overall computational cost which scales with $\mathcal{O}(Re^{\frac{11}{4}})$, thus constraining practical applications of turbulent flows to small Reynolds-numbers. Therefore, the Large-eddy simulation (LES) can be seen as the most suitable approach to obtain a three-dimensional unsteady simulation of a turbulent flow [Garnier et al., 2009]. The basic idea of LES is a scale separation approach, where the large-scale most-energetic turbulent structures are fully resolved and the effect of the unresolved smaller scales is accounted for by the adoption of a model. According to Kolmogorov's theory of turbulence [Kolmogorov, 1991], small scales of the flow are supposed to be universal and less dependent on the boundary conditions than large scales, therefore leading to a simplification of the underlying LES modeling effort.

2.2.1. The filtering procedure

The above mentioned spatial-scale separation can be mathematically defined as the convolution of a flow variable with a filter kernel. The resolved part of an arbitrary vector field $\phi(\mathbf{x}, t)$ is therefore defined by:

$$\bar{\phi}(\mathbf{x}, t) = \int_{\Omega(t)} G(\mathbf{x} - \mathbf{x}'; \Delta) \phi(\mathbf{x}', t) d\mathbf{x}' = G * \phi, \quad (2.12)$$

where G is a homogeneous filter convolution kernel with normalization

$$\int G(\mathbf{x}) d\mathbf{x} = 1 \quad (2.13)$$

and Δ its associated characteristic cut-off scale in space. Note that the spatial cut-off scale is directly associated to the cut-off wave number $k_c = \pi/\Delta$ in Fourier-space. The vector field ϕ is split into a resolved $\bar{\phi}$ and non-resolved part ϕ' , where the latter quantity is referring to the subgrid-scales:

$$\phi = \bar{\phi} + \phi'. \quad (2.14)$$

It is worth mentioning that three different filters can be identified in the framework of LES, where two of them act implicitly. The first being the *analytical filter* represented by the convolution product introduced above, that is needed for explicit subgrid-scale models, where the additional model terms are derived from filtering operations on the resolved fields. The second one is the *grid filter*, which arises from the use of a finite computational mesh which is too coarse to resolve the smallest scales of the turbulent flow and thus acts as an implicit low-pass filter in Fourier-space. The latter is, hence, associated to the numerical scheme. Although the accuracy of a numerical scheme is often characterized by the order of its truncation error in physical space, it seems more appropriate to compute the spectral distribution of the truncation error in Fourier-space for LES in order to assess which wave numbers k are captured by the numerical scheme [Garnier et al., 2009]. Therefore, the numerical solution of the Navier-Stokes equations is a result of all the mentioned filtering processes which constitute the effective filter.

2.2.2. Explicit LES approach

In the framework of the explicit LES both the *analytical filter* and the *grid filter* are active. To avoid any confusion between the grid-filtered and test-filtered fields, the grid-filtered field will be denoted by the *overline* notation $\overline{(\cdot)}$ and the test-filtered field will be indicated by the *hat* notation $\hat{(\cdot)}$. Both filters are of the type introduced in Eqns. (2.12) and (2.13) and they also possess *consistency*, *linearity* and *commutation* properties [Garnier et al., 2009]. The grid-filtered compressible Navier-Stokes equations may be written as:

2. Numerical approach

$$\frac{\partial \bar{\rho}}{\partial t} + \frac{\partial \bar{\rho} \tilde{u}_i}{\partial x_i} = 0, \quad (2.15)$$

$$\frac{\partial \bar{\rho} \tilde{u}_i}{\partial t} + \frac{\partial \bar{\rho} \tilde{u}_i \tilde{u}_j}{\partial x_j} + \frac{\partial \bar{p}}{\partial x_i} - \frac{1}{Re} \frac{\partial \tilde{\tau}_{ij}}{\partial x_j} = -A_i^1 + A_i^2, \quad (2.16)$$

$$\begin{aligned} & \frac{\partial \bar{\rho} \tilde{E}}{\partial t} + \frac{\partial \bar{\rho} \tilde{E} \tilde{u}_j}{\partial x_j} - \frac{\partial \bar{p} \tilde{u}_j}{\partial x_j} + \frac{1}{Re} \frac{\partial \tilde{\tau}_{ij} \tilde{u}_j}{\partial x_j} - \\ & \frac{1}{(\gamma - 1) Re Pr Ma^2} \frac{\partial}{\partial x_j} \left(\tilde{\mu} \frac{\partial \tilde{T}}{\partial x_j} \right) = -B_1 - B_2 - B_3 + B_4 + B_5 + B_6 - B_7, \end{aligned} \quad (2.17)$$

where the quantities on the left hand-side can be directly calculated from the resolved scales. The terms on the right hand-side need to be modeled and represent the effects of the unresolved subgrid-scales. The tilde notation denotes the Favre-filter operator which is defined as:

$$\tilde{\phi} = \frac{\overline{\rho \phi}}{\bar{\rho}}. \quad (2.18)$$

This change of variable, in which filtered variables are weighted by the density, is often used in the compressible case, since the necessary transformation from $\overline{\rho u_i}$ to $\bar{\rho} \tilde{u}_i$ raising from the non-linear terms in the Navier-Stokes equations would result in an additional subgrid term which can be avoided by the use of Favre-filtering. An exact definition of the subgrid-scale terms at the right hand side of the above introduced system of equations can be found in the work of [Vreman et al., 1995, Garnier et al., 2009]. On the basis of the a posteriori analysis of DNS data proposed by [Vreman et al., 1995], it is possible to neglect part of the arising subgrid-scale terms obtaining the following form for the system of equation:

$$\frac{\partial \bar{\rho}}{\partial t} + \frac{\partial \bar{\rho} \tilde{u}_i}{\partial x_i} = 0, \quad (2.19)$$

$$\frac{\partial \bar{\rho} \tilde{u}_i}{\partial t} + \frac{\partial \bar{\rho} \tilde{u}_i \tilde{u}_j}{\partial x_j} + \frac{\partial \bar{p}}{\partial x_i} - \frac{1}{Re} \frac{\partial \tilde{\tau}_{ij}}{\partial x_j} \approx -\frac{\partial \sigma_{i,j}}{x_j}, \quad (2.20)$$

$$\begin{aligned} & \frac{\partial \bar{\rho} \tilde{E}}{\partial t} + \frac{\partial \bar{\rho} \tilde{E} \tilde{u}_j}{\partial x_j} - \frac{\partial \bar{p} \tilde{u}_j}{\partial x_j} + \frac{1}{Re} \frac{\partial \tilde{\tau}_{ij} \tilde{u}_j}{\partial x_j} - \\ & \frac{1}{(\gamma - 1) Re Pr Ma^2} \frac{\partial}{\partial x_j} \left(\tilde{\mu} \frac{\partial \tilde{T}}{\partial x_j} \right) \approx -\frac{\partial \sigma_{i,j} \tilde{u}_j}{x_j} - \frac{1}{(\gamma - 1) Ma^2} \frac{\partial \bar{\rho} Q_j}{\partial x_j}. \end{aligned} \quad (2.21)$$

The terms $\sigma_{i,j}$ and Q_j represent the SGS stress tensor and the SGS Reynolds heat flux, respectively defined as:

$$\sigma_{ij} = \bar{\rho} (\overline{u_i u_j} - \tilde{u}_i \tilde{u}_j), \quad (2.22)$$

$$Q_j = (\overline{T u_j} - \tilde{T} \tilde{u}_j). \quad (2.23)$$

According to the energy cascade process in turbulent flows, on average the energy is transferred from the large scales (integral length scales L) to the small ones (Kolmogorov scales η), where finally the energy is dissipated through viscous effects and transformed into internal energy. The main task of a subgrid-scale model is to account for the influence of the unresolved scales onto the resolved ones and in particular to predict the energy transfer between those scales in an adequate manner. Since the energy transfer to the small scales has been artificially inhibited through the filtering process, the subgrid-scale model becomes responsible for providing the correct amount of energy dissipation. In the framework of the explicit LES a simple eddy-viscosity assumption is commonly made in analogy to gas kinetics, which states that the impulse transfer between turbulent eddies through collisions induces stresses:

$$\sigma_{ij} - \frac{1}{3}\delta_{ij}\sigma_{kk} = -2\bar{\rho}\nu_t\tilde{S}_{ij}^D, \quad (2.24)$$

where ν_t denotes the eddy viscosity and \tilde{S}_{ij}^D is the deviatoric part of the strain-rate tensor which is computed from the filtered velocity field as follows:

$$\tilde{S}_{ij}^D = \tilde{S}_{ij} - \frac{1}{3}\delta_{ij}\tilde{S}_{kk} = \frac{1}{2}\left(\frac{\partial\tilde{u}_i}{\partial x_j} + \frac{\partial\tilde{u}_j}{\partial x_i}\right) - \frac{1}{3}\delta_{ij}\tilde{S}_{kk}. \quad (2.25)$$

The eddy viscosity ν_t has been modeled in numerous ways, the most popular model being the classical Smagorinsky model where, according to the mixing length model of Prandtl number, the eddy viscosity is related to a length and velocity-scale, the length-scale being implicitly prescribed by the filter length Δ . A detailed overview of several SGS models for LES of compressible flows is given in the work of [Garnier et al., 2009]. Once the eddy viscosity ν_t has been calculated, the SGS heat flux is modeled through:

$$Q_j = \widetilde{T\tilde{u}_j} - \tilde{T}\tilde{u}_j = -\frac{\nu_t}{Pr_t}\frac{\partial\tilde{T}}{\partial x_i}, \quad (2.26)$$

where Pr_t denotes the turbulent Prandtl, which is often considered constant. After having related the unresolved scales to the resolved ones through Eqns. (2.24)-(2.26), the system of equations is closed.

2.2.3. Implicit LES approach

In the previous section, explicit SGS modeling has been introduced by the filtering concept where the underlying conservation law is modified and subsequently discretized. Without suggesting specific discretization schemes it was assumed for the explicit SGS approach, that the truncation error of the spatial discretization scheme is small enough, hence not affecting the SGS physics. Thus, the numerical method and the turbulence modeling are assumed to be completely decoupled which in general is not true. However, when solving numerically Eqns. (2.19)-(2.21) the explicitly computed SGS stress is affected by the truncation error of the discretization scheme. This interference can result in strange results such as the lack of grid

2. Numerical approach

convergence. [Ghosal, 1996] has analyzed this problem analytically and has found that the truncation error even of a fourth-order central-difference discretization can have the same order of magnitude as the SGS stress. Implicit large-eddy simulation (ILES) discretizes the unmodified conservation law and exploits this interference between truncation error and SGS stress. Instead of an explicit computation of the SGS stress, the truncation error of the discretization scheme itself is employed to model the effects of unresolved scales. Therefore, ILES discretizes the unmodified conservation law and employs the truncation error of the spatial discretization scheme, which is calibrated in such a way that it acts as a physically motivated SGS model. Since the SGS model is implicitly contained within the discretization scheme, an explicit computation of model terms becomes consequently unnecessary [Adams et al., 2004, Hickel et al., 2006, Hickel and Larsson, 2008]. In order to highlight the general idea of the ILES approach, consider the following generic one-dimensional non-linear scalar transport equation for ϕ :

$$\frac{\partial \phi}{\partial t} + \frac{\partial F(\phi)}{\partial x} = 0 \quad (2.27)$$

Following the filtering procedure, the discretized equation is obtained by convolution with an homogeneous filter kernel G and the subsequent discretization

$$\frac{\partial \bar{\phi}_N}{\partial t} + G * \frac{\partial F_N(\phi_N)}{\partial x} = -G * \frac{\partial \mathcal{G}_{SGS}}{\partial x}, \quad (2.28)$$

where the subscript N indicates grid functions resulting from the projection of the continuous function $\phi(x)$ onto the numerical grid $x_N = x_j$, thus representing a discrete approximation of $\phi(x)$. This projection operation is one of the sources of the SGS modeling problem in LES, since it removes all scales beyond the Nyquist wavenumber $k_c = \pi/\Delta_g$, where Δ_g is assumed to be a constant grid spacing. It has also to be noted that Eq. (2.28) considers spatial scales only, although the underlying transport equations makes it possible to associate a characteristic time scale with a length scale. However, it is common practice to consider only spatial filtering, assuming that all relevant time scales are resolved by choosing a sufficiently small time step for the time integration scheme [Hickel et al., 2006].

In order to compute the nonlinear term in Eq. (2.28), the represented-scale part of the unfiltered field is reconstructed by a suitable numerical approximation of the inverse-filter operation $\phi_N = G^{-1} * \bar{\phi}_N$ applied to represented scales. Such reconstruction is defined as soft deconvolution problem. Since non-represented scales cannot be retrieved, it is $\phi_N \neq \phi$. The irreversibility of the grid projection of non-linear terms is the cause of the generation of the subgrid-stress tensor or residual

$$\mathcal{G}_{SGS} = F(\phi) - F_N(\phi_N), \quad (2.29)$$

which needs to be modeled in order to close Eq. (2.28). An introduction to the explicit SGS models which provide approximations or estimations of \mathcal{G}_{SGS} has been given in the previous Sec. 2.2.2.

When Eq. (2.28) is solved numerically, the truncation error of the numerical discretization scheme affects the solution $\bar{\phi}_N$ in such a way that it does not satisfy Eq. (2.28) anymore, but rather a Modified Differential Equation (MDE) which may be formulated as:

$$\frac{\partial \bar{\phi}_N}{\partial t} + G * \frac{\partial F_N(\phi_N)}{\partial x} = \mathcal{G}_N - \check{G} * \frac{\check{\partial} \check{\mathcal{G}}_{SGS}}{\check{\partial} x}, \quad (2.30)$$

where the approximate numerical operators are denoted as $(\check{\cdot})$. The truncation error of the discretization scheme for the calculation of the numerical fluxes \mathcal{G}_N can be expressed as:

$$\mathcal{G}_N = G * \frac{\partial F_N(\phi_N)}{\partial x} - \check{G} * \frac{\check{\partial} \check{F}(\check{\phi}_N)}{\check{\partial} x}, \quad (2.31)$$

where $\check{\phi}_N$ is an approximation of the discrete grid function ϕ_N , which is obtained from a regularized deconvolution applied to $\bar{\phi}_N$. In the framework of explicit LES, it is generally assumed that $\|\mathcal{G}\| \gg \|G * \partial_x \mathcal{G}_{SGS}\|$ and that $\check{\mathcal{G}}_{SGS} \doteq \mathcal{G}_{SGS}$, but actually such requirement is violated by most of the discretization schemes at grid resolutions that are of common use for LES. As it has been shown in other works [Ghosal, 1996, Kravchenko and Moin, 1997], this mutual interference of G_N and G_{SGS} can have large and generally unpredictable effects on the accuracy of LES results. In the present work we will make use of an implicit large-eddy simulation approach which is based on the so called Adaptive Local Deconvolution Method which employs the Finite Volume (FV) method as a starting point.

Finite Volume formulation

We consider the compressible Navier-Stokes equations expressed in a conservative form :

$$\frac{\partial \mathbf{U}}{\partial t} + \nabla \cdot \mathbf{F}(\mathbf{U}) = 0. \quad (2.32)$$

After defining the computational domain $\Omega(t)$ and integrating Eq.(2.32) over the space-time volume $V_j \cap \Omega(t)$ of a computational cell we obtain the following finite volume discretization

$$\frac{\partial \bar{\mathbf{U}}}{\partial t} = -\frac{1}{V_j} \oint_{\partial(V_j \cap \Omega(t))} \mathbf{F}(\mathbf{U}) \cdot \mathbf{n} dA + \frac{1}{V_j} \oint_{V_j \cap \Omega(t)} \mathbf{S}(\mathbf{U}) dV, \quad (2.33)$$

where the solution vector $\bar{\mathbf{U}}$ containing the volume averaged conserved variables is defined as

$$\bar{\mathbf{U}} = \frac{1}{V_j} \int_{V_j} \mathbf{U} dV_j. \quad (2.34)$$

The vector $\mathbf{U} = [\rho, \rho u_1, \rho u_2, \rho u_3, \rho E]$ contains density ρ , momentum ρu_i and total energy ρE . The overbar notation $(\bar{\cdot})$ identifies the volume average for any arbitrary

2. Numerical approach

control volume $V_j \cap \Omega(t)$, which can be considered equal to any of the computational cells of the grid. The flux form adopted in Eq. (2.32) ensures the exact conservation of all components of the solution vector independently from the numerical scheme adopted to compute the fluxes $\mathbf{F}(\mathbf{U})$ at the control volume surface $\partial(V_j \cap \Omega(t))$. For later convenience the flux $\mathbf{F}(\mathbf{U})$ across $\partial(V_j \cap \Omega(t))$ is split into three components: a first component $\mathbf{C}(\mathbf{U})$ due to the convective terms, a second component $\mathbf{P}(\mathbf{U})$ due to surface stresses related to pressure and a final component $\mathbf{D}(\mathbf{U})$ due to viscous surface stresses. Non-conservative source terms are collected into $\mathbf{S}(\mathbf{U})$. The components of the fluxes along each direction of the reference system is given as:

$$\mathbf{F}_i = \mathbf{C}_i + \mathbf{P}_i + \mathbf{D}_i = \begin{bmatrix} u_i \rho \\ u_i \rho u_1 \\ u_i \rho u_2 \\ u_i \rho u_3 \\ u_i \rho E \end{bmatrix} + \begin{bmatrix} 0 \\ \delta_{i1} p \\ \delta_{i2} p \\ \delta_{i3} p \\ u_k \delta_{ik} p \end{bmatrix} + \begin{bmatrix} 0 \\ \tau_{i1} \\ \tau_{i2} \\ \tau_{i3} \\ u_k \tau_{ik} + q_i \end{bmatrix}, \quad (2.35)$$

Overview on the Adaptive Local Deconvolution Method ¹

The finite volume method provides a suitable framework for I-LES. The FV discretization corresponds in fact to the evaluation of Eq. (2.28) using a top-hat filter

$$G(\mathbf{x}, V_j) d\mathbf{x} = \begin{cases} 1/V_j & , \quad \mathbf{x} \in V_j \\ 0 & , \quad \mathbf{x} \notin V_j \end{cases}. \quad (2.36)$$

The numerical building blocks of finite-volume methods are a reconstruction of the unfiltered solution at cell faces, a numerical flux function that works on the reconstructed solution, and a numerical integration scheme to compute the face-averaged flux. The truncation error of finite-volume methods can be expressed as the divergence of a tensor. This is a favorable feature with respect to physically motivated implicit modeling. ALDM is therefore based on exploiting the formal equivalence between cell-averaging and reconstruction in finite-volume discretizations and top-hat filtering and deconvolution in SGS modeling.

Reconstruction procedure: the reconstruction of the unfiltered solution is obtained from a solution-adaptive convex combination of Harten-type deconvolution polynomials [Hickel et al., 2006, Adams et al., 2004, Harten et al., 1997]:

$$\tilde{g}_{k,r}^\mp(x_{j\pm 1/2}) = \sum_{l=0}^{k-1} c_{k,r,l}^\mp(x_N) \bar{\phi}(x_{j-r+l}), \quad (2.37)$$

where half-integer indices denote reconstructions at the cell faces. The grid-dependent coefficients $c_{k,r,l}^\mp(x_N)$ are chosen such that

$$\tilde{g}_{k,r}^\mp(x_{j\pm 1/2}) = \phi(x_{j\pm 1/2}) + \mathcal{O}(\Delta_g^k) \quad (2.38)$$

¹In this section a brief overview on the Adaptive Local Deconvolution Method for compressible flows is given. A more detailed description of the method can be found in the work of [Hickel, 2012].

on a grid with spacing Δ_g . The deconvolution is regularized by limiting the degree k of local approximation polynomials to $k < K$ and by permitting all polynomials of degree $1 < k < K$ to contribute to the approximately deconvolved solution. The adaptivity of the deconvolution operator is achieved by dynamically weighing the respective contributions by the factors

$$\omega_{k,r}(\gamma_{k,r}, \bar{\phi}_N) = \frac{\gamma_{k,r}^\lambda \beta_{k,r}(\bar{\phi}_N)}{\sum_{s=0}^{k-1} \gamma_{k,s}^\lambda \beta_{k,s}(\bar{\phi}_N)}, \quad (2.39)$$

where $\gamma_{k,r}$ are free model parameters and $\beta_{k,r}$ are estimates of the smoothness of the grid function on the respective stencil, to obtain a nonlinear adaptation of the deconvolution. The following functional

$$\beta_{k,r}(\bar{\phi}_N, x_i) = \left(\epsilon_\beta + \sum_{l=-r}^{k-r-2} (\bar{\phi}(x_{i+m+1}) - \bar{\phi}(x_{i+m}))^2 \right)^{-2}, \quad (2.40)$$

where $\epsilon_\beta = 10^{-99}$ to avoid division by zero. The procedure described above leads to a hierarchy of reconstructions with increasing order of accuracy

$$\tilde{\phi}_1^\mp(x_{j\pm 1/2}) = \tilde{g}_{1,0}^\mp(x_{j\pm 1/2}) \quad (2.41)$$

$$\tilde{\phi}_2^\mp(x_{j\pm 1/2}) = \sum_{r=0}^1 \omega_{2,r}^\mp(\gamma_{2,r}, \bar{\phi}_N) \tilde{g}_{2,r}^\mp(x_{j\pm 1/2}) \quad (2.42)$$

$$\tilde{\phi}_3^\mp(x_{j\pm 1/2}) = \sum_{r=0}^2 \omega_{3,r}^\mp(\gamma_{3,r}, \bar{\phi}_N) \tilde{g}_{3,r}^\mp(x_{j\pm 1/2}), \quad (2.43)$$

which are then combined in the final reconstruction step:

$$\tilde{\phi}^\mp(x_{j\pm 1/2}) = \sum_{k=1}^K \alpha_k \tilde{\phi}_k^\mp(x_{j\pm 1/2}), \quad (2.44)$$

where the additional parameters α_k are introduced. In the compressible framework the local adaptive reconstruction scheme is applied to primitive rather than conserved variables leading to improved robustness of the numerical method in case of strong density gradients.

Numerical flux function: a suitable consistent numerical flux function operates on the approximately deconvolved solution. The adopted numerical flux function is capable to meet the requirement of preserving the symmetries of the Navier-Stokes flux and of being asymptotically consistent with incompressible turbulence theory for low Mach number flows [Hickel, 2012]. For implicit SGS modeling, only the hyperbolic flux $\mathbf{C} + \mathbf{P}$ is considered, whose discretization causes the SGS effects of interest. The effect of the truncation error of the diffusive flux could also be considered, as done by [Zandonade et al., 2004] for finite-volume optimal LES. However, the discretization of the viscous flux has negligible influence on the results of LES

2. Numerical approach

at large Reynolds numbers, since the grid cutoff is typically chosen to be within the inertial range. Gradients in the viscous flux tensor \mathbf{D} are therefore approximated by linear second-order schemes.

In the ALDM framework, secondary regularization is provided by a numerical flux function with the general form

$$\tilde{F}_{j\pm 1/2} = F \left(\frac{\tilde{\phi}^+ + \tilde{\phi}^-}{2} \right) - R (\tilde{\phi}^+ - \tilde{\phi}^-). \quad (2.45)$$

The numerical flux is composed of two elements. The first term corresponds to the physical Navier-Stokes flux computed from the mean of both reconstructions of the unfiltered solution at the considered cell face. The difference between both reconstructions is exploited in a regularization term based on the reconstruction error $(\tilde{\phi}^+ - \tilde{\phi}^-)$. The dissipation matrix R needs to be defined specifically for the particular differential equation being under consideration.

Based on this observation, the single component of the convective flux C_i is given as

$$\tilde{C}_i^\rho = \tilde{u}^* \frac{\tilde{\rho}^+ + \tilde{\rho}^-}{2} - R_i^\rho (\tilde{\rho}^+ - \tilde{\rho}^-) \quad (2.46)$$

$$\tilde{C}_i^{\rho u_i} = \tilde{C}_i^\rho \frac{\tilde{u}_i^+ + \tilde{u}_i^-}{2} - R_i^{\rho u_i} \frac{\tilde{\rho}^+ + \tilde{\rho}^-}{2} (\tilde{u}_k^+ - \tilde{u}_k^-) \quad (2.47)$$

$$\tilde{C}_i^{\rho E} = \tilde{u}^* \frac{\tilde{\rho E}^+ + \tilde{\rho E}^-}{2} + \frac{\tilde{u}_k^+ + \tilde{u}_k^-}{2} \left(\tilde{C}_i^{\rho u_i} - \frac{\tilde{u}_k^+ + \tilde{u}_k^-}{4} \tilde{C}_i^{\rho u_k} \right) - R_i^{\rho E} (\tilde{\rho E}^+ - \tilde{\rho E}^-). \quad (2.48)$$

The pressure flux is defined in the following way:

$$\tilde{\mathbf{P}}_i = \begin{bmatrix} 0 \\ \delta_{i1} \tilde{p}^* \\ \delta_{i2} \tilde{p}^* \\ \delta_{i3} \tilde{p}^* \\ \tilde{u}_i^* \tilde{p}^* \end{bmatrix}, \quad (2.49)$$

where the interface pressure and transport velocity are computed from:

$$\tilde{p}^* = \frac{\tilde{p}^+ + \tilde{p}^-}{2} \quad (2.50)$$

$$\tilde{u}_i^* = \frac{\tilde{u}_i^+ + \tilde{u}_i^-}{2} - \frac{1}{\tilde{c}} \frac{\tilde{p}_3^+ - \tilde{p}_3^-}{\tilde{\rho}^+ + \tilde{\rho}^-}, \quad (2.51)$$

Here \tilde{c} is the maximum speed of sound achieved in the adjacent cells. It has to be highlighted that the second term in Eq. (2.51) is introduced in order to ensure the pressure velocity coupling.

In the framework of compressible flows, subgrid-scales are related to unresolved turbulence but can also be connected to the presence of shockwaves. The spectral energy transfer at shock waves differs considerably from the mechanisms in unresolved turbulence. These differences have to be taken into account in the SGS

modeling strategy. Unresolved turbulence can be modeled with a numerical viscosity proportional to a velocity gradient and the square of a characteristic length scale. Propagating discontinuities represent unique SGS that usually modeled with a numerical viscosity proportional to the fastest signal speed. Based on the considerations above, the dissipation matrix is defined as follows:

$$\tilde{\mathbf{R}}_i = \begin{bmatrix} \sigma^\rho |\tilde{u}_i^+ - \tilde{u}_i^-| \\ \sigma^{\rho u_1} |\tilde{u}_1^+ - \tilde{u}_1^-| \\ \sigma^{\rho u_2} |\tilde{u}_2^+ - \tilde{u}_2^-| \\ \sigma^{\rho u_3} |\tilde{u}_3^+ - \tilde{u}_3^-| \\ \sigma^{\rho E} |\tilde{u}_i^+ - \tilde{u}_i^-| \end{bmatrix} + f_s \frac{|\tilde{u}_i^*| + |\tilde{u}_i^+ - \tilde{u}_i^-|}{2} \begin{bmatrix} 1 \\ 1 \\ 1 \\ 1 \\ 1 \end{bmatrix}. \quad (2.52)$$

An additional term is hereby added to the regularization which is responsible to account for the spectral energy transfer taking place at shock waves. This second term is active only in the region where discontinuities are detected by the sensor functional of [Ducros et al., 2000] :

$$f_s = \begin{cases} 1 & , \quad \frac{|\nabla \cdot \bar{u}|}{|\nabla \cdot \bar{u}| + \|\nabla \times \bar{u}\|} \geq 0.95 \\ 0 & , \quad else \end{cases}, \quad (2.53)$$

where the large threshold value in Eq. (2.53) ensures that the term is active only at strong shock waves.

The proposed form of the numerical flux is therefore capable of guaranteeing the correct dissipation mechanism for unresolved turbulence and shockwaves and also ensures asymptotic consistency with the ALDM formulation for incompressible turbulence in the limit of $Ma \rightarrow 0$.

Finally the values for the model parameters α, γ, σ in the adaptive stencil-selection scheme and the numerical flux function are optimized to adjust the spatial truncation error of the discretization. The list of the values obtained for the parameters after the optimization can be found in the work of [Hickel, 2012].

ALDM Wall effects: The solution-adaptive behavior of ALDM is controlled by dynamic weight functionals $\omega_{k,r}^\mp$. The form of these weights is defined in such a way that their statistical average resembles a central reconstruction scheme for isotropic turbulence. Near solid walls, however, velocity fluctuations are strongly anisotropic. Time-averaged values of selected weight functions of the ALDM deconvolution operator are shown in Fig. 2.1 for a supersonic turbulent channel flow. We note that ALDM reacts to flow anisotropy by becoming anisotropic in the near-wall region. The resulting weights always prefer the stencil that is closer to the wall as shown, e.g., for the wall-normal velocity component in Fig. 2.1. This weight distribution leads to an upwind bias for fluid moving away from the wall and to a downwind bias for fluid moving towards the wall. A central scheme is reproduced only at the channel centerline and at two other other planes within the logarithmic layer.

The effect of the non-symmetric stencil selection on the implicit SGS model can be analyzed indirectly. By considering the results of a direct numerical simulation

2. Numerical approach

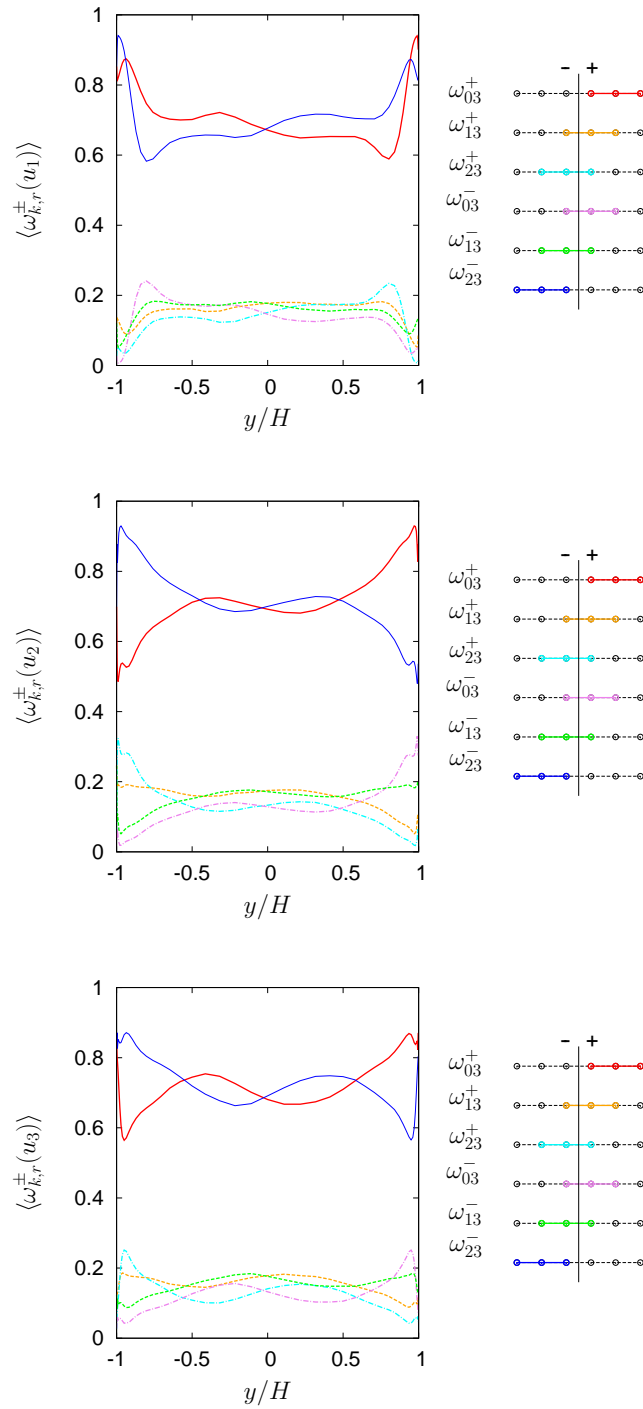


Figure 2.1.: Time-averaged ALDM weight functions for central deconvolution of the streamwise and wall-normal velocity component. Implicit LES of supersonic turbulent channel flow at $Re_\tau = 450$.

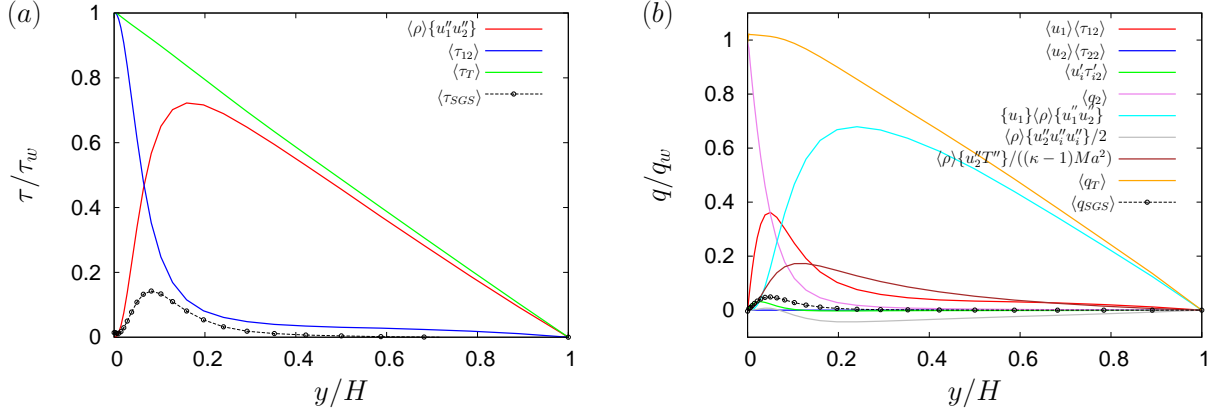


Figure 2.2.: (a) Decomposition of the total shear stress τ_T . (b) Decomposition of the total heat flux q_T .

of a supersonic turbulent channel flow at $Ma = 3$ and $Re = 4880$ it is possible to compute the single contributions to the total shear stress $\langle \tau_T \rangle$ and the total heat flux $\langle q_T \rangle$ [Huang et al., 1995].

$$\frac{\langle \tau_T \rangle}{\langle \tau_w \rangle} = \frac{1}{\langle \tau_w \rangle} \left(\langle \tau_{12} \rangle - \langle \rho \rangle \{ u''_1 u''_2 \} \right) \quad (2.54)$$

$$\begin{aligned} \frac{\langle q_T \rangle}{\langle q_w \rangle} &= \frac{1}{\langle q_w \rangle} \left(\langle u_1 \rangle \langle \tau_{12} \rangle + \langle u_2 \rangle \langle \tau_{22} \rangle + \langle u'_i \tau'_{i2} \rangle - \langle q_2 \rangle \right. \\ &\quad \left. - \{ u_1 \} \langle \rho \rangle \{ u''_1 u''_2 \} - \langle \rho \rangle \frac{\{ u''_2 u''_i u''_i \}}{2} - \frac{\langle \rho \rangle \{ u''_2 T'' \}}{(\kappa - 1) Ma^2} \right) \end{aligned} \quad (2.55)$$

The statistical average of the residual stress and heat flux of the implicit SGS model can be computed from the global shear-stress and energy balance as follows:

$$\left. \frac{\langle \tau_T \rangle}{\langle \tau_w \rangle} \right|_{SGS} = \left. \frac{\langle \tau_T \rangle}{\langle \tau_w \rangle} \right|_{DNS} - \left. \frac{\langle \tau_T \rangle}{\langle \tau_w \rangle} \right|_{I-LES} \quad (2.56)$$

$$\left. \frac{\langle q_T \rangle}{\langle q_w \rangle} \right|_{SGS} = \left. \frac{\langle q_T \rangle}{\langle q_w \rangle} \right|_{DNS} - \left. \frac{\langle q_T \rangle}{\langle q_w \rangle} \right|_{I-LES} \quad (2.57)$$

Figures 2.2(a) and 2.2(b) show the singular component of the total shear stress and heat flux computed from the implicit LES results, together with the SGS contribution obtained by using the DNS results as reference. The position of maximum SGS contribution is closer to the wall than expected. The location of the SGS term maximum does not coincide with the location of the resolved-Reynolds-shear-stress and resolved turbulent heat transfer maximum. This shift is a consequence of the anisotropic stencil selection, which causes increased SGS contributions near the walls.

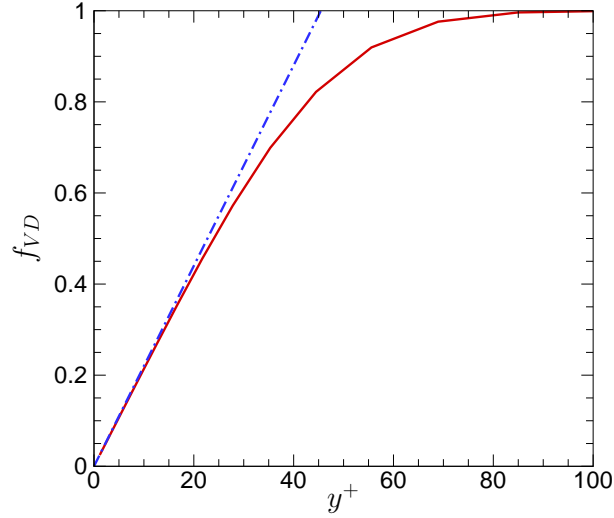


Figure 2.3.: Effective van Driest damping for the implicit LES of a supersonic turbulent channel flow at $Re_\tau = 450$, — damping functional used with ALDM (parameters value $s = 1/3$, $d = 3$, $a^+ = 50$) and -.- linear approximation $0.02 y^+$.

Approaches for wall correction: One of the possible approaches to reduce the discretization anisotropy in the vicinity of the wall can be based on constraining or damping the dynamic range of the stencil weights. Another possible approach can be formulated by reducing the dissipative weight of the numerical flux function. As already shown in the work of [Hickel, 2007], the latter approach is more practicable due to a less negative impact on numerical stability of the former.

Van Driest wall damping: For the purpose of wall modeling a new formulation is proposed for the factor $\sigma^{\rho u_i}$ based on the Van Driest damping

$$\sigma_{VD}^{\rho u_i} = \sigma^{\rho u_i} \underbrace{\left(1 - \exp \left[- \left(\frac{l_w u_\tau}{a^+ \nu} \right)^d \right] \right)^s}_{f_{VD}} \quad (2.58)$$

where l_w is the wall distance and u_τ is the friction velocity at the closest wall. The original scheme is recovered at large wall distances where $\sigma_{VD}^{\rho u_i} \rightarrow \sigma^{\rho u_i}$; d and a^+ are free parameters. The wall-asymptotic behavior of the effective change of the model parameter $\sigma^{\rho u_i}$ can be determined by Taylor series expansion. The leading term of the expansion is

$$f_{VD} \approx \frac{1}{(a^+)^{ds}} (y^+)^{ds}. \quad (2.59)$$

The work of [Hickel, 2007] has shown that the damping of Eq. (2.59) is rather insensitive to the particular choice of d and a^+ . Given d , an optimal value for the length

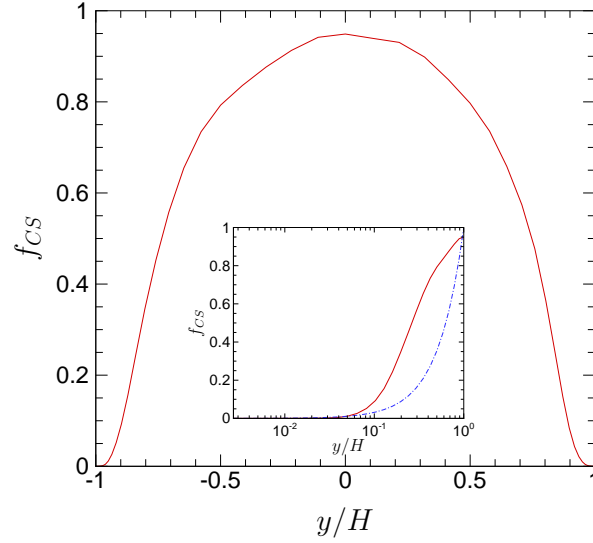


Figure 2.4.: Effective coherent-structure damping for the implicit LES of a supersonic turbulent channel flow at $Re_\tau = 450$, — damping function and - - - analytical approximation in the vicinity of the wall $(y/H)^{3/2}$.

scale a^+ can be selected such that the correct wall-shear stress is obtained. Optimal values for ALDM were proposed [Hickel, 2007] as

$$d = \frac{1}{s} = 3 \quad (2.60)$$

$$a^+ = 50.0 \quad (2.61)$$

With the adopted parameter values, the van Driest damping does not affect ALDM at wall distances $y^+ > 80$. The effective damping function is plotted in Fig. 2.3.

Coherent structure based criterion: A different formulation to achieve an adaptive coefficient $\sigma_{CS}^{\rho u_i}$ is proposed based on the coherent structures model described in the work of [Kobayashi, 2005, Kobayashi et al., 2008]. In this work, a new approach is given for the dynamic computation of the Smagorinsky model constant C_s using a function of the velocity gradient tensor. The method is based on the assumption that the SGS dissipation is small in the center of a coherent fine-scale eddy, and that the energy transfer between resolved scales and SGS is located around this coherent

eddy. The damping coefficient in this case is constructed as follows:

$$\sigma_{CS}^{\rho u_i} = \sigma^{\rho u_i} \underbrace{\pi F_{CS}^{3/2} F_\Omega}_{f_{CS}} \quad (2.62)$$

$$F_{CS} = \frac{\langle Q \rangle}{\langle E \rangle} \quad , \quad F_\Omega = 0.9 (1 - F_{CS}), \quad (2.63)$$

$$Q = \frac{1}{2} (\langle W_{ij} \rangle \langle W_{ij} \rangle - \langle S_{ij} \rangle \langle S_{ij} \rangle) \quad , \quad E = \frac{1}{2} (\langle W_{ij} \rangle \langle W_{ij} \rangle + \langle S_{ij} \rangle \langle S_{ij} \rangle), \quad (2.64)$$

$$\langle W_{ij} \rangle = \frac{1}{2} \left(\frac{\partial \langle u_j \rangle}{\partial x_i} - \frac{\partial \langle u_i \rangle}{\partial x_j} \right) \quad , \quad \langle S_{ij} \rangle = \frac{1}{2} \left(\frac{\partial \langle u_j \rangle}{\partial x_i} + \frac{\partial \langle u_i \rangle}{\partial x_j} \right). \quad (2.65)$$

$\langle S_{ij} \rangle$ and $\langle W_{ij} \rangle$ are the Reynolds averaged velocity-strain tensor and the vorticity tensor of the flow field, respectively. F_{CS} is the coherent-structure function defined as the second invariant $\langle Q \rangle$ normalized by the magnitude of the resolved velocity gradient tensor $\langle E \rangle$. For incompressible flows, the second invariant $Q \propto x^2$ and $E \propto const$, therefore, the 3/2 power of f_{CS} scales the implicit SGS viscosity proportionally to $x^{(3/2)}$ near the wall. Figure 2.4 shows the effective damping function obtained for the implicit LES of a supersonic turbulent channel flow. In contrast to the van-Driest damping approach the unit value is never recovered even in the channel centerline. A detailed analysis and validation of the different damping approaches proposed here can be found in Sec. (3.1).

2.3. Boundary conditions

2.3.1. Turbulent inflow boundary condition

When considering DNS and LES of turbulent flows, one needs to prescribe three-dimensional and time-dependent inflow conditions with correct statistical moments, phase information and spectrum of the real turbulent flow under consideration [Touber, 2009]. Stated by [Garnier et al., 2009], the definition of such inflow conditions is certainly one of the hardest open problems in the field of LES research. The most straightforward approach is to simulate the complete transition from laminar to turbulent by adding random disturbances to the laminar inflow profiles, hence inducing natural transition further downstream. This approach has been followed in the work of [Pirozzoli et al., 2004] and [Shahab et al., 2011], which allows to avoid prescribing time-dependent turbulent fluctuations at the domain inlet. Besides the fact that this method yields the most realistic results, simulating the transition process is in itself a very expensive approach from the computational point of view.

In order to cope with this issue, one needs a certain level of approximation for practical applications, hence yielding a conflict between accuracy and efficiency. Commonly used techniques can be classified into two categories, namely *precursor* methods and *synthetic turbulence* methods.

The basic idea of the precursor type of methods is to run auxiliary simulations to provide time and space dependent inflow conditions for the actual simulation. Therefore, inflow boundary conditions are extracted from an instantaneous plane of the auxiliary simulation and rescaled to the correct flow properties of the inflow plane of the actual simulation [Stolz and Adams, 2003]. This is the basic idea of the periodic and recycling/rescaling techniques, where the auxiliary simulation directly generates the inflow condition since periodic boundary conditions are applied in streamwise direction. The most famous approach has been introduced by [Spalart and Leonard, 1985], where the spatial streamwise growth of the boundary layer in the auxiliary simulation is replaced by additional source terms in the Navier-Stokes equations. The major drawback of this method is the explicit evaluation of such growth terms. Based on the approach by [Spalart and Leonard, 1985], [Lund et al., 1998] proposed a simplified method where the auxiliary simulation is allowed to be quasi-periodic. Therefore, the outflow boundary conditions of the auxiliary simulation are extracted and rescaled back to the inflow plane in an adequate manner. It is worth mentioning that this recycling/rescaling technique can be used either in the context of an auxiliary simulation or within the actual simulation itself by placing the extraction plane inside the main domain. One major drawback in conjunction with the recycling/rescaling technique with respect to the shockwave boundary layer interaction dynamics that are investigated in this work is the fact that this method artificially introduces a frequency content related to the recycling length, hence strongly affecting the interaction dynamics. In order to exclude that the investigated shock motion is affected by numerical artifacts, the recycling/rescaling approach proposed by [Lund et al., 1998] has been avoided in this work.

The basic idea of the synthetic turbulence methods is to prescribe an artificial inflow field which resembles the real turbulence by matching first/second order statistical moments. Stated by [Touber and Sandham, 2010], one major consequence of the high level of approximation used is that the flow will be unphysical for some distance downstream of the inflow plane. This in turn means that the flow exhibits a certain unphysical transient length in which it slowly recovers these modeling errors. One needs to account for this fact when considering the spatial extent of the simulation domain. The simplest approach is to add random disturbances such as white noise to the mean profiles. This method, however, usually leads to relaminarization of the flow, since the energy in the wave-number space associated to this approach is uniformly distributed, leading to a small amount of energy in the large wavelengths. A more sophisticated approach is the Digital Filter (DF) technique originally proposed by [Klein et al., 2003]. The general idea of this method will be discussed briefly in the following. A random dataset is filtered to achieve targeted one-point second order statistics as well as autocorrelation functions. Stated by [Veloudis et al., 2007], integral length scales are used as input to make the non-dimensional assumed (often Gaussian) shape of the autocorrelation function dimensional at each point. Besides the prescribed turbulence length (or time) scales in each coordinate direction, the main input parameters for the DF technique are the first and second order statistical moments (mean values and Reynolds stresses) of

all three velocity components for the inlet plane. In order to account for different length scales present in boundary layers with regard to the wall-normal direction, [Veloudis et al., 2007] proposed a zonal approach which will also be used in this work. Based on this input, the DF approach is able to generate the inflow time-dependent velocity field. The remaining task is to generate the thermodynamic fluctuations, which in general is achieved by making use of the Strong Reynolds Analogy (SRA), hence linking velocity fluctuations already obtained from the DF technique with temperature fluctuations. Density fluctuations are obtained assuming that the pressure is constant across the boundary layer. For a more detailed description of the DF technique with respect to implementation issues the interested reader is referred to [Klein et al., 2003, Touber, 2009, Veloudis et al., 2007].

2.3.2. Conservative Immersed Interface Method

Mathematical basis

The computational domain $\Omega(t)$ is divided into two different subdomains $\Omega_1(t)$ and $\Omega_2(t)$, by the interface $\Gamma(t)$. The volume $\Omega_1(t)$ accounts for the region occupied by the fluid and $\Omega_2(t)$ refers to the region occupied by the solid obstacle. We solve Eq. (2.31) for the fluid occupying the sub-domain Ω_1 on a three-dimensional Cartesian grid with spacings $\Delta x, \Delta y, \Delta z$. The fluid volume $V_{i,j,k} \cap \Omega_1(t)$ can be expressed through $\alpha_{i,j,k}(t)\Delta x\Delta y\Delta z$, where $\alpha_{i,j,k}(t)$ is the fluid volume fraction of the considered cell (i, j, k) . Applying Gauss' theorem to Eq. (2.31), we obtain

$$\int_n^{n+1} dt \int_{V_{i,j,k} \cap \Omega_1(t)} dx dy dz \frac{\partial \mathbf{U}}{\partial t} + \int_n^{n+1} dt \int_{\partial(V_{i,j,k} \cap \Omega_1)} dx dy dz \mathbf{F} \cdot \mathbf{n} = 0, \quad (2.66)$$

where $\partial(V_{i,j,k} \cap \Omega_1(t))$ are the cell faces. Defining the interface segment within $V_{i,j,k}$ as $\Delta\Gamma_{i,j,k}(t) = \Gamma(t) \cap V_{i,j,k}$, the term $\partial(V_{i,j,k} \cap \Omega_1(t))$ can be expressed as the combination of two elements. The first element is the sum of the surfaces obtained by intersecting the interface with the cell faces, which can be presented as $A_{i,j,k}^{11}\Delta y\Delta z, A_{i,j,k}^{12}\Delta y\Delta z, A_{i,j,k}^{21}\Delta x\Delta z, A_{i,j,k}^{22}\Delta x\Delta z, A_{i,j,k}^{31}\Delta x\Delta y, A_{i,j,k}^{32}\Delta x\Delta y$ where $A_{i,j,k}^{lm}$ is the so called cell face aperture described in Fig. 2.5. The second element is the interface segment $\Delta\Gamma_{i,j,k}(t)$. After introducing the volume averaged solution, Eq. (2.66) can be rewritten in the following form where time integration is approximated for simplicity by an forward-Euler scheme and all terms on the right hand side are evaluated at t^n . Note that for Runge-Kutta schemes this corresponds to a substep

$$\begin{aligned} & \Delta x \Delta y \Delta z \left(\alpha_{i,j,k}^{n+1} \bar{\mathbf{U}}_{i,j,k}^{n+1} - \alpha_{i,j,k}^n \bar{\mathbf{U}}_{i,j,k}^n \right) \\ & = \Delta t \Delta y \Delta z \left[A_{i,j,k}^{11} \mathbf{F}_{i,j,k}^{11} - A_{i,j,k}^{12} \mathbf{F}_{i,j,k}^{12} \right] \\ & + \Delta t \Delta x \Delta z \left[A_{i,j,k}^{21} \mathbf{F}_{i,j,k}^{21} - A_{i,j,k}^{22} \mathbf{F}_{i,j,k}^{22} \right] \\ & + \Delta t \Delta x \Delta y \left[A_{i,j,k}^{31} \mathbf{F}_{i,j,k}^{31} - A_{i,j,k}^{32} \mathbf{F}_{i,j,k}^{32} \right] + \Delta t \mathbf{X}_{i,j,k} (\Delta\Gamma_{i,j,k}(t)). \end{aligned} \quad (2.67)$$

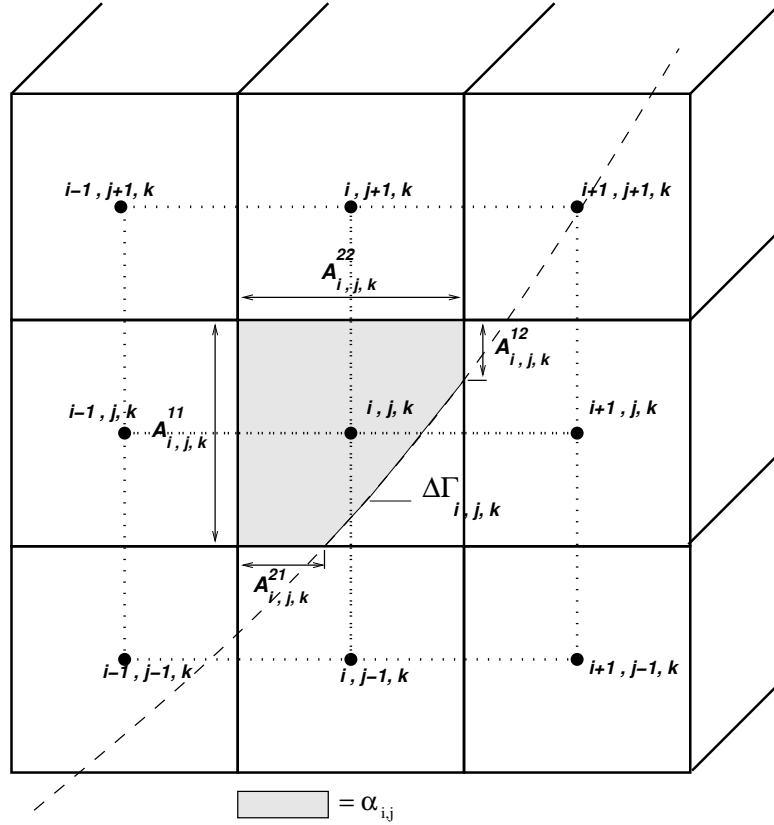


Figure 2.5.: Two dimensional schematic of conservative discretization for a cut cell.

$\Delta t = t^{n+1} - t^n$ is the time step size, $\alpha_{i,j,k} V_{i,j,k} \bar{\mathbf{U}}_{i,j,k}$ and $\bar{\mathbf{U}}_{i,j,k}$ are the vector of the conserved quantities in the cut cell and the vector of volume averaged conservative variables respectively. $\mathbf{F}_{i,j,k}^{lm}$ is the average flux across a cell face and $\mathbf{X}_{i,j,k}$ is the integral momentum and energy exchange across the interface. Details on $\mathbf{X}_{i,j,k}$ are given in the following section. For cells that are not cut by the interface, volume fractions and cell face apertures become unity, the corresponding interface surface fraction $\Delta\Gamma_{i,j,k}$ vanishes and Eq. (2.66) simplifies to

$$\begin{aligned} V_{i,j,k} (\bar{\mathbf{U}}_{i,j,k}^{n+1} - \bar{\mathbf{U}}_{i,j,k}^n) &= \Delta t \Delta y \Delta z [\mathbf{F}_{i,j,k}^{11} - \mathbf{F}_{i,j,k}^{12}] \\ + \Delta t \Delta x \Delta z [\mathbf{F}_{i,j,k}^{21} - \mathbf{F}_{i,j,k}^{22}] &+ \Delta t \Delta x \Delta y [\mathbf{F}_{i,j,k}^{31} - \mathbf{F}_{i,j,k}^{32}]. \end{aligned} \quad (2.68)$$

Being effective only in cut cells, this immersed interface method can be seen as a local modification of the underlying finite volume scheme near the interface.

Geometry of the immersed interface

Cell-face apertures $A_{i,j,k}^{lm}$, volume fractions $\alpha_{i,j,k}$ and interface area $\Delta\Gamma_{i,j,k}(t)$ are determined from a levelset field Φ , i.e., a signed distance of a point in the domain to the immersed surface. The zero-levelset contour ($\Phi = 0$) describes the interface between

the fluid and the obstacle. Cells that are completely inside the obstacle are blocked by imposing zero cell-face apertures and consequently do not contribute to the volume balances. The levelset field allows for the representation arbitrary geometries and straightforward handling of moving boundaries.

Interface interaction

The interface interaction term $\mathbf{X}_{i,j,k}(\Delta\Gamma_{i,j,k})$ proposed in Eq. (2.67) contains contributions of pressure, viscous effects and heat transfer to the momentum and energy balance across the interface

$$\mathbf{X}_{i,j,k}(\Delta\Gamma_{i,j,k}) = \mathbf{X}^p + \mathbf{X}^v + \mathbf{X}^{ht}. \quad (2.69)$$

The cell index is omitted, for clarity, here and in the following equations.

Pressure term \mathbf{X}^p : following the work of [Hu et al., 2006] a one-sided face-normal Riemann problem

$$\mathcal{R}(\bar{\mathbf{U}}, \mathbf{v}_n^\Gamma) = 0 \quad (2.70)$$

is solved for the pressure on $\Delta\Gamma(t)$. The velocity $\mathbf{v}_n^\Gamma = \mathbf{v}^\Gamma \mathbf{n}^\Gamma$ is the component of the interface velocity in the direction of the local normal vector \mathbf{n}^Γ on the interface. The interface velocity can be imposed for a given interface motion or it can be derived from fluid-structure interaction. Approximate Riemann solvers [Toro, 2006] are sufficient for solving Eq.(2.70) with acceptable accuracy. After solving the Riemann problem for the interface pressure p_Γ , the contributions of the term \mathbf{X}^p to momentum and energy equation are computed as follows

$$\mathbf{X}^p = \begin{bmatrix} 0 \\ p_\Gamma \Delta\Gamma(t) n_1^\Gamma \\ p_\Gamma \Delta\Gamma(t) n_2^\Gamma \\ p_\Gamma \Delta\Gamma(t) n_3^\Gamma \\ p_\Gamma \Delta\Gamma(t) (\mathbf{n}^\Gamma \cdot \mathbf{v}^\Gamma) \end{bmatrix}, \quad (2.71)$$

where $\mathbf{n}^\Gamma = [n_1^\Gamma, n_2^\Gamma, n_3^\Gamma]$ is the interface normal vector.

Viscous term \mathbf{X}^v : in order to take into account the viscous stress at the immersed boundary, a viscous term \mathbf{X}^v is added to the flux balance of the cut cell. This term contributes to the momentum and energy equations. The contribution to the momentum equation derives from the friction force \mathbf{D} that a fluid moving along a solid boundary exerts on the boundary itself. Integrating the viscous stress tensor $\bar{\boldsymbol{\tau}}$ over the surface of the fluid solid interface $\Delta\Gamma(t)$ gives

$$\mathbf{D} = \int_{\Delta\Gamma(t)} \bar{\boldsymbol{\tau}} \cdot \mathbf{n}^\Gamma dS \quad (2.72)$$

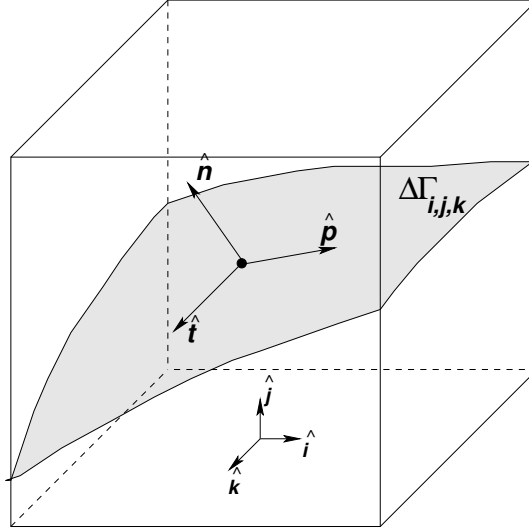


Figure 2.6.: Local reference system for a cut cell.

The viscous stress tensor $\bar{\tau}$ can be expressed in the local reference system $(\hat{n}, \hat{t}, \hat{p})$, see Fig. 2.6, as

$$\bar{\tau} = \begin{bmatrix} 2\mu \frac{\partial u_n}{\partial \hat{n}} - \frac{2}{3}\mu (\nabla \cdot \mathbf{u}) & \mu \left(\frac{\partial u_t}{\partial \hat{n}} + \frac{\partial u_n}{\partial \hat{t}} \right) & \mu \left(\frac{\partial u_p}{\partial \hat{n}} + \frac{\partial u_n}{\partial \hat{p}} \right) \\ \mu \left(\frac{\partial u_n}{\partial \hat{t}} + \frac{\partial u_t}{\partial \hat{n}} \right) & 2\mu \frac{\partial u_t}{\partial \hat{t}} - \frac{2}{3}\mu (\nabla \cdot \mathbf{u}) & \mu \left(\frac{\partial u_t}{\partial \hat{p}} + \frac{\partial u_p}{\partial \hat{t}} \right) \\ \mu \left(\frac{\partial u_n}{\partial \hat{p}} + \frac{\partial u_p}{\partial \hat{n}} \right) & \mu \left(\frac{\partial u_p}{\partial \hat{t}} + \frac{\partial u_t}{\partial \hat{p}} \right) & 2\mu \frac{\partial u_p}{\partial \hat{p}} - \frac{2}{3}\mu (\nabla \cdot \mathbf{u}) \end{bmatrix}. \quad (2.73)$$

A line approximation of the interface surface cutting the cell together with the no-slip condition lead to the following simplification of the term $\nabla \cdot \mathbf{u}$

$$\nabla \cdot \mathbf{u} = \frac{\partial u_n}{\partial \hat{n}} + \frac{\partial u_t}{\partial \hat{t}} + \frac{\partial u_p}{\partial \hat{p}}. \quad (2.74)$$

The viscous stress tensor then reduces to

$$\bar{\tau} = \begin{bmatrix} 2\mu \frac{\partial u_n}{\partial \hat{n}} - \frac{2}{3}\mu \frac{\partial u_n}{\partial \hat{n}} & \mu \frac{\partial u_t}{\partial \hat{n}} & \mu \frac{\partial u_p}{\partial \hat{n}} \\ \mu \frac{\partial u_t}{\partial \hat{n}} & -\frac{2}{3}\mu \frac{\partial u_n}{\partial \hat{n}} & 0 \\ \mu \frac{\partial u_p}{\partial \hat{n}} & 0 & -\frac{2}{3}\mu \frac{\partial u_n}{\partial \hat{n}} \end{bmatrix} \quad (2.75)$$

and the viscous force becomes with second order accuracy

$$\mathbf{D} \simeq \int_{\Delta\Gamma(t)} \bar{\tau} \cdot \mathbf{n}^\Gamma dS \simeq \begin{bmatrix} \frac{4}{3}\mu \frac{\partial u_n}{\partial \hat{n}} \\ \frac{\partial u_t}{\partial \hat{n}} \\ \frac{\partial u_p}{\partial \hat{n}} \end{bmatrix} \Delta\Gamma(t). \quad (2.76)$$

The local volume averaged velocity can be decomposed into a normal and a tangential component

$$\bar{\mathbf{u}} = \mathbf{u}^\parallel + \mathbf{u}^\perp, \quad (2.77)$$

2. Numerical approach

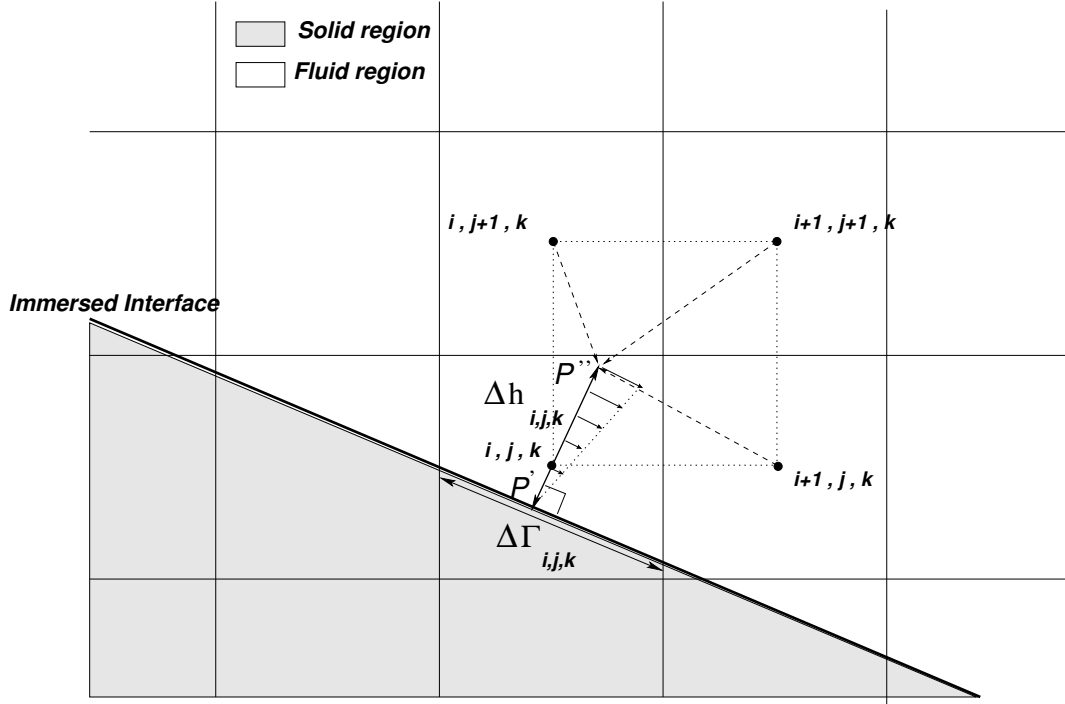


Figure 2.7.: Two-dimensional description of the interpolation.

where

$$\mathbf{u}^\perp = (\bar{\mathbf{u}} \cdot \mathbf{n}^\Gamma) \cdot \mathbf{n}^\Gamma \quad (2.78)$$

$$\mathbf{u}^\parallel = \bar{\mathbf{u}} - \mathbf{u}^\perp. \quad (2.79)$$

Based on the previous definition, the viscous force becomes

$$\mathbf{D} = \begin{bmatrix} \frac{4}{3}\mu \frac{\partial u_n}{\partial \hat{n}} \\ \frac{\partial u_t}{\partial \hat{n}} \\ \frac{\partial u_p}{\partial \hat{n}} \end{bmatrix} \Delta\Gamma_{i,j,k}(t) = \mu \left(\frac{4}{3} \frac{\partial \mathbf{u}^\perp}{\partial \hat{n}} + \frac{\partial \mathbf{u}^\parallel}{\partial \hat{n}} \right) \Delta\Gamma(t). \quad (2.80)$$

The problem now reduces to the computation of the velocity gradient. The velocity gradient is computed by a linear approximation, and an estimate of the velocity difference is obtained by subtracting the interface velocity \mathbf{v}^Γ from the velocity $\mathbf{u}_{P''}$ in the point P'' , see Fig. 2.7. The point P'' is determined based on the foot point P' on the immersed interface, the normal vector and the distance $\Delta h_{i,j,k}$. The velocity in P'' is calculated from the eight surrounding cell centers using a linear Lagrange interpolation as proposed in [Meyer et al., 2010]. The same interpolation procedure is used to interpolate the viscosity μ in the interpolation point P'' . Then, Eq. (2.80) can be written as

$$\mathbf{D} = \mu \left(\frac{4}{3} \frac{\mathbf{u}_{P''}^\perp - \mathbf{v}_\perp^\Gamma}{\Delta h} + \frac{\mathbf{u}_{P''}^\parallel - \mathbf{v}_\parallel^\Gamma}{\Delta h} \right) \Delta\Gamma(t), \quad (2.81)$$

with

$$\mathbf{v}_\perp^\Gamma = (\mathbf{v}^\Gamma \cdot \mathbf{n}^\Gamma) \cdot \mathbf{n}^\Gamma \quad (2.82)$$

$$\mathbf{v}^\parallel = \mathbf{v}^\Gamma - \mathbf{v}_\perp^\Gamma, \quad (2.83)$$

where the length scale Δh is defined as

$$\Delta h = \sqrt{(\Delta x n_1^\Gamma)^2 + (\Delta y n_2^\Gamma)^2 + (\Delta z n_3^\Gamma)^2}, \quad (2.84)$$

Concerning the energy equation, the presence of the immersed boundary introduces a new term C , which is effective only in case of moving boundary problems

$$C = \int_{\Delta\Gamma(t)} (\bar{\boldsymbol{\tau}} \cdot \mathbf{v}^\Gamma) \cdot d\mathbf{S}. \quad (2.85)$$

Using the quantities that were introduced previously we obtain with second-order accuracy in the global reference system

$$C \simeq \mathbf{D} \cdot \mathbf{v}^\Gamma. \quad (2.86)$$

The additional viscous term of the flux balance of the cut cell \mathbf{X}^v assumes the following final expression

$$\mathbf{X}^v = \begin{bmatrix} 0 \\ D_1 \\ D_2 \\ D_3 \\ C \end{bmatrix}. \quad (2.87)$$

Heat Transfer term \mathbf{X}^{ht} : in case of an adiabatic solid wall, no heat is transferred across the boundary since $\nabla T \cdot \mathbf{n} = 0$, but heat transfer q has to be considered in case of an isothermal wall boundary condition. The heat transfer across the interface $\Delta\Gamma_{i,j,k}$ is

$$q = \int_{\Delta\Gamma(t)} k \nabla T \cdot d\mathbf{S} = \int_{\Delta\Gamma(t)} k \nabla T \cdot \mathbf{n}^\Gamma dS, \quad (2.88)$$

the temperature gradient ∇T is expressed in the local reference system $(\hat{n}, \hat{t}, \hat{p})$ as described in Fig. 2.6. A linear approximation of the interface cutting the cell and the isothermal-wall assumption lead to the following simplification of the temperature gradient

$$\nabla T = \begin{bmatrix} \frac{\partial T}{\partial \hat{n}} \\ \frac{\partial T}{\partial \hat{t}} \\ \frac{\partial T}{\partial \hat{p}} \end{bmatrix} = \begin{bmatrix} \frac{\partial T}{\partial \hat{n}} \\ 0 \\ 0 \end{bmatrix} \quad (2.89)$$

and the heat transfer across the wall boundary is approximated with second order accuracy as

$$q = \int_{\Delta\Gamma(t)} k \nabla T \cdot d\mathbf{S} = k \frac{\partial T}{\partial \hat{n}} \Delta\Gamma(t). \quad (2.90)$$

2. Numerical approach

The temperature gradient is computed by linear approximation and an estimate of the temperature difference is obtained by subtracting the fixed wall temperature T^Γ from the temperature $T^{P''}$ in the point P'' , see Fig. 2.7. The temperature in P'' is calculated from the eight surrounding cell centers using a linear Lagrange interpolation. For the computation of the temperature gradient we use the same distance $\Delta h_{i,j,k}$ as in the previous section. The resulting approximation to the heat flux is

$$q = k \frac{T^{P''} - T^\Gamma}{\Delta h} \Delta \Gamma(t), \quad (2.91)$$

where the thermal conductivity k is evaluated in the in the interpolation point P'' . The heat transfer term \mathbf{X}^{ht} added to the flux balance of the cut cell is

$$\mathbf{X}^{ht} = \begin{bmatrix} 0 \\ 0 \\ 0 \\ 0 \\ q \end{bmatrix}. \quad (2.92)$$

Mixing Procedure

The intersection between the immersed interface and the Cartesian grid can give rise to small cells for which a stable fluid state may not be reached based on the timestep calculated according to the *CFL* condition for the full cell size. On the other hand, accounting for the real size of these small cells can lead to extremely small time steps.

In order to achieve numerical stability without the need of excessively decreasing the time step size, a conservative mixing procedure is introduced, where the conserved quantities of small cells are mixed with larger neighboring cells. The procedure essentially follows the approach proposed in the work of [Hu et al., 2006]. Modifications are introduced in order to account for non uniform grid spacing and in order to remove directional dependencies. Furthermore, the number of target cells adopted for the mixing is increased to include all possible neighboring cells available in a three dimensional field.

The mixing procedure is only applied to cut cells with a volume fraction below a certain threshold, which in our computational examples is set to $\alpha_{th} = 0.5$. Increasing this threshold allows for a larger timestep but reduces the accuracy of the solution in the interface region.

Seven target cells for mixing are determined from the local normal vector on the interface. For each mixing target cell a weight $\beta_{i,j,k}$ is defined

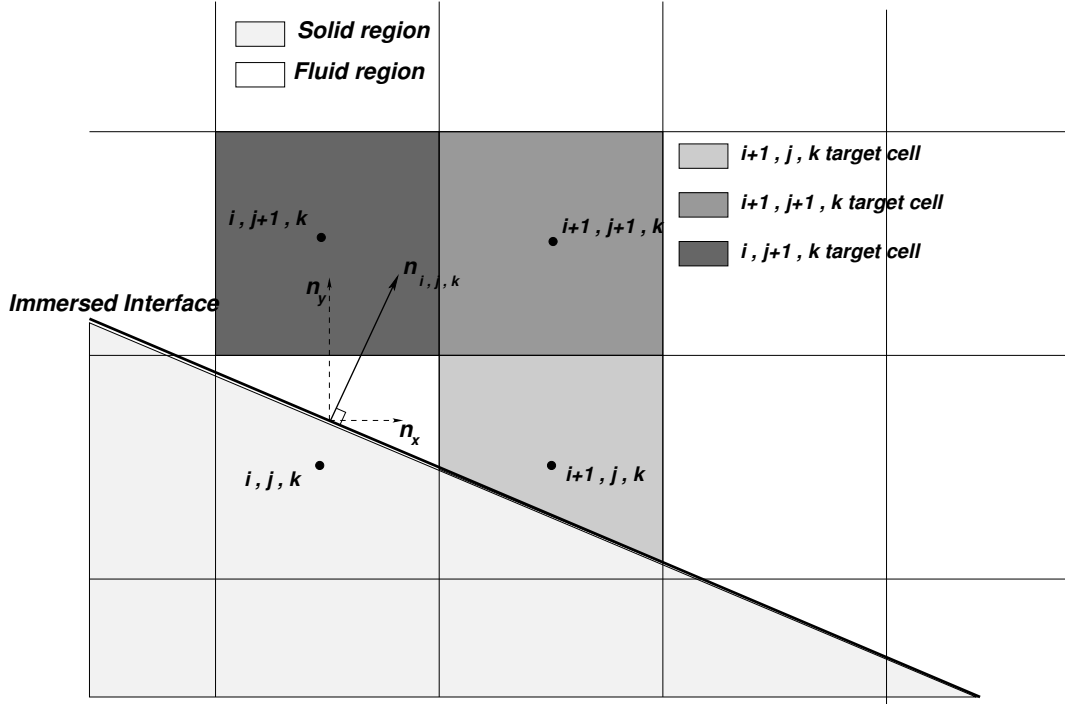


Figure 2.8.: Two dimensional description of the mixing procedure.

$$\begin{aligned}
 \beta_{i,j,k}^x &= |n_1^\Gamma|^2 \alpha_{mix_{i,j,k}} & (2.93) \\
 \beta_{i,j,k}^y &= |n_2^\Gamma|^2 \alpha_{i,mix_{j,k}} \\
 \beta_{i,j,k}^z &= |n_3^\Gamma|^2 \alpha_{i,j,mix_k} \\
 \beta_{i,j,k}^{xy} &= |n_1^\Gamma n_2^\Gamma| \alpha_{mix_i,mix_{j,k}} \\
 \beta_{i,j,k}^{xz} &= |n_1^\Gamma n_3^\Gamma| \alpha_{mix_i,j,mix_k} \\
 \beta_{i,j,k}^{yz} &= |n_2^\Gamma n_3^\Gamma| \alpha_{i,mix_j,mix_k} \\
 \beta_{i,j,k}^{xyz} &= |n_1^\Gamma n_2^\Gamma n_3^\Gamma|^{2/3} \alpha_{mix_i,mix_j,mix_k} .
 \end{aligned}$$

The weights are subsequently normalized to ensure consistency

$$\beta_{i,j,k}^x + \beta_{i,j,k}^y + \beta_{i,j,k}^z + \beta_{i,j,k}^{xy} + \beta_{i,j,k}^{xz} + \beta_{i,j,k}^{yz} + \beta_{i,j,k}^{xyz} = 1 . \quad (2.94)$$

The mixing flux $M_{i,j,k}^{trg}$ is calculated for each mixing direction in the following way

$$M_{i,j,k}^{trg} = \frac{\beta_{i,j,k}^{trg} [(V_{trg} \alpha_{trg} \bar{U}_{trg}) V_{i,j,k} \alpha_{i,j,k} - (V_{i,j,k} \alpha_{i,j,k} \bar{U}_{i,j,k}) V_{trg} \alpha_{trg}]}{\alpha_{i,j,k} V_{i,j,k} \beta_{i,j,k}^{trg} + \alpha_{trg} V_{trg}} , \quad (2.95)$$

where trg stands for the mixing target cell. Conservativity is maintained by a flux

formulation consistent with non-uniform Cartesian grids

$$\bar{U}_{i,j,k} = (\bar{U}_{i,j,k})^* + \frac{M_{i,j,k}^{trg}}{\alpha_{i,j,k}^n V_{i,j,k}} \quad (2.96)$$

$$\bar{U}_{trg} = (\bar{U}_{trg})^* - \frac{M_{i,j,k}^{trg}}{\alpha_{trg}^n V_{trg}} \quad (2.97)$$

where $(\bar{U}_{i,j,k})^*$ and $(\bar{U}_{trg})^*$ are the volume averaged conserved variables of the cut cell (i, j, k) and of the target cell before mixing. This procedure is applied for all small cut cells and mixing target cells before each time-step and Runge-Kutta sub-step.

Note that the mixing procedure automatically deals with vanishing and newly created cells. In the first case, the conservative quantities are all transported to the target cells, whereas, for the second case, the conservative quantities in a newly created small cell are derived directly from its target cell.

Extending Procedure

In order to allow for using unmodified, interpolation stencils in the finite volume reconstruction scheme near the interface and to provide physical conditions for newly created fluid cells, the conserved variables are extrapolated across the interface into a ghost-cell by solving

$$\frac{\partial \bar{U}}{\partial t_f} - \mathbf{n} \cdot \nabla \bar{U} = 0, \quad (2.98)$$

in the pseudo-time t_f until a steady state solution in the near interface region is reached. In case of stationary boundary condition the velocity is mirrored in the cells that are located beyond the ghost-cell, while in case of moving boundary the velocity is set to be equal to the local interface velocity \mathbf{v}^Γ . In case of isothermal wall boundary condition the temperature is set to be equal to the local wall temperature T^Γ , the pressure is obtained from the extension procedure, the density is calculated from the local wall temperature and the extended pressure and finally the energy is computed from the extended pressure, the newly computed density and the local velocities. For an adiabatic wall boundary, the extending procedure is applied to all the thermodynamic variables.

2.3.3. Implementation

At the beginning of the computation, the level-set field is computed on the basis of geometrical input data. Based on the level-set field information, cut cells are identified and their face apertures and volume fractions are determined. In cases with non-moving interfaces this procedure is applied once at the start of the computation. For moving interfaces, the level-set field is updated and the above procedure has to

be repeated in each timestep. The general procedure for one Euler time step can be summarized as follows:

Step 1. The conservative mixing procedure is applied to all cells with a volume fraction below the set threshold.

Step 2. Given the volume averaged conservative quantities \bar{U}^n , the extending procedure described in Sec. 2.3.2 is applied to small or empty cells in the interface region and to the cells on the other side of the interface.

Step 3. The convective and diffusive fluxes are calculated for all cells without accounting for the presence of the interface.

Step 4. The fluxes across the cell faces of cut cells are scaled with the face apertures.

Step 5. The terms X^p , X^v and X^{ht} are computed in each cut cell.

Step 6. The flux divergence is computed.

Step 7. The level-set field and the solution are advanced in time.

At the end of this procedure, mass, energy and momentum conservation are locally and globally ensured by construction. A third-order Runge-Kutta time integration scheme [Shu, 1988] is used in this work. In each Runge-Kutta sub-step, all the steps are invoked once. For moving interfaces, the level-set field needs to be updated in time in each Runge-Kutta sub-step. After each sub-step, cut cells are identified with the instantaneous zero-level-set, and their face apertures and volume fractions are updated.

3. Numerical approach validation

In this present chapter the validation of the single component blocks of the numerical approach is presented. The implicit large-eddy simulation approach and the digital-filter technique for the generation of the turbulent inflow profiles will be validated through supersonic turbulent channel flow and boundary layer computations. A set of validation cases for the conservative immersed interface method is also presented.

3.1. ALDM for compressible wall bounded flows

Most flows of practical interest are bounded by a solid surface. Examples include internal flows such as the flow through pipes, channels, ducts and tunnels; external flows such as the flow around aircraft, cars, ships or other vehicles.

The first LES of wall-bounded flow dates back to the 1970's when [Deardorff, 1970] performed the first large-eddy simulation of an incompressible channel flow, at infinitely large Reynolds number, using the Smagorinsky model and only 6720 grid points. A few years later, fast growing computer resources allowed [Kim et al., 1987] to carry out a LES on a grid almost 10 times the size of Deardorff's and at a Reynolds number, based on channel halfwidth and mean centerline velocity, of $Re = 13800$. Nevertheless, the first DNS computed by [Kim et al., 1987] was only affordable in the mid-80's and used about four million grid points to simulate the turbulent incompressible channel flow at a Reynolds number of $Re = 3253$. These DNS results provided an unprecedented insight into the details of near-wall flow phenomena and allowed for assessments and improvements of RANS turbulence models and LES subgrid-scale models.

The effect of compressibility on wall-bounded flows has been investigated experimentally by [Morkovin, 1962] and [Bradshaw, 1977]. They concluded that for a Mach number up to 5 and in the absence of massive heat transfer at the wall, small-scale turbulent fluctuations were little affected by compressibility (often referred to as Morkovin's hypothesis in the literature). Numerical confirmation of this hypothesis was obtained from the DNS of the supersonic channel flow of [Coleman et al., 1995], followed by the DNS of supersonic boundary layers of [Guarini et al., 2000] and [Maeder et al., 2001]. Later [Foyi et al., 2004] further investigated the effects of compressibility and gave an explanation for the reduction of pressure-strain correlations in supersonic compared to incompressible isothermal channel flow by relating it to the sharp wall-normal density variations in the framework of a Green-function-based analysis of the pressure field.

In this section, we propose an analysis of the different implicit modeling approaches for wall bounded flows. The original ALDM formulation is compared with its extensions based on the van-Driest and the coherent-structures damping procedures. Each of the formulations is evaluated through a comparison with results derived from Direct Numerical Simulation.

3.2. Supersonic turbulent channel flow

3.2.1. Problem setup

Supersonic, turbulent channel flow only exists when the heat generated by dissipation within the flow field is removed through the walls. This requirement poses the need for wall cooling and leads to the generation of strong near-wall mean temperature, viscosity and density gradients. The compressible channel flow considered here features a Reynolds number based on the bulk quantities and channel half-width of $Re_b = 4880$ and a Mach number of $Ma = 3.0$. This flow configuration allows to compare our DNS results with those of [Coleman et al., 1995]. We consider an ideal gas with a ratio of specific heats $\gamma = c_p/c_v = 1.4$. The variables are non-dimensionalized with the wall temperature T_w , the channel half-width H , the bulk averaged density $\rho_b = \int_0^1 \langle \rho \rangle d(y/H)$ and the bulk velocity $u_b = 1/\rho_b \int_0^1 \langle \rho \rangle \langle u \rangle d(y/H)$. The Reynolds number is defined with the bulk quantities and the channel half-width H as $Re = \rho_b u_b H / \mu_w$, and the Mach number is computed according to $Ma = u_b / c_w$. The non-dimensional dynamic viscosity is calculated using as a power law with the exponent $\psi = 0.7$ [Coleman et al., 1995]. The time is non-dimensionalized with H/u_b . The friction Reynolds number $Re_\tau = \rho_w u_\tau H / \mu_w$, with $u_\tau = \tau_w / \rho_w$, is a result of the simulations.

The channel flow is periodic in the streamwise (x) and spanwise (z) directions. The wall boundary conditions are no-slip for the velocity and isothermal for the temperature. To enforce streamwise periodic boundary conditions in the simulation, the mean pressure gradient $\partial \langle p \rangle / \partial x$ has been replaced by a body force of type f_{pg} . In the course of the simulation the body force f_{pg} is controlled to achieve constant mass flux. The grid spacing is constant in the streamwise and spanwise directions and is stretched with hyperbolic tangent function in the wall-normal direction. Table 3.2 gives an overview of the different grids resolutions adopted for the simulation. Except for the DNS, all simulations were initialized with a laminar velocity profile with a random disturbance superimposed in each of the three coordinate directions. The maximal amplitude of the disturbances was chosen to be 10% of the bulk velocity. To save computer time, the DNS simulation was started from a turbulent profile obtained from a coarse grid LES computation, interpolated onto the fine DNS mesh. The convective fluxes are computed using the Adaptive Local Deconvolution Method. The viscous fluxes are discretized using a second-order central differences scheme. Time advancement is achieved by a third-order TVD explicit Runge-Kutta [Shu, 1988].

Table 3.1.: Lines and symbols for the different cases.

Case	Symbol
DNS [Coleman et al., 1995]	
DNS	
LES (ALDM) ^a	
LES (ALDM-VD) ^b	
LES (ALDM-CS) ^c	

(^a) Original ALDM formulation for compressible flows as in [Hickel, 2012].
(^b) ALDM with van-Driest formulation for wall-damping.
(^c) ALDM with coherent structures damping approach.

Table 3.2.: Grid adopted for the resolutions study.

Case	N_x	N_y	N_z	β^b
DNS [Coleman et al., 1995] ^a	144	119	80	-
DNS	504	128	168	2.45
LES (L1)	320	170	86	2.9
LES (L2)	640	170	86	2.6

(^a) Results obtained using a spectral Fourier-Legendre space differentiation
(^b) hyperbolic tangent stretching function in the y -direction
 $y(i) = L_y(1.0 - \tanh(\beta_y(1.0 - i/Ny)))/\tanh(\beta_y)$

Table 3.3.: Mean flow variables.

Case	Δx^+	Δy^+	Δz^+	Re_τ	$\langle T_c \rangle^a$
DNS [Coleman et al., 1995]	39.1	0.2	24.0	451.0	2.493
DNS	11.2	0.5	5.6	450.0	2.498
LES (L1) - ALDM	40.0	0.8	15.0	412.3 (8.4%)	2.538 (1.61%)
LES (L1) - ALDM-VD	41.3	1.1	20.7	414.5 (7.9%)	2.522 (0.97%)
LES (L1) - ALDM-CS	40.0	0.8	15.0	429.4 (4.6%)	2.481 (0.66%)
LES (L2) - ALDM	20.0	0.8	7.0	422.3 (6.2%)	2.523 (1.02%)
LES (L2) - ALDM-VD	31.8	1.1	16.5	424.6 (5.6%)	2.506 (0.33%)
LES (L2) - ALDM-CS	20.0	0.8	7.0	441.3 (1.9%)	2.489 (0.31%)

(^a) The subscript c indicates center-line values.

3.2.2. Flow description

Turbulent channel flows are characterized by the presence of alternately high-speed and low-speed streaks in the viscosity-affected near-wall layer. It is well established, based on two-point-correlation data, that the length of the streaks in fully-established channel flow or a canonical boundary layer is of order 10^3 wall units [Kreplin and Eckelmann, 1979], and that the streaks are separated by a distance of order 10^2 wall units [Kim et al., 1971]. There is no complete agreement, however, on the precise mechanisms responsible for the formation and sustenance of these quasi-organised structures. Conventional explanations, mostly derived from low-Reynolds-number DNS results, focus on the quasi-streamwise vortices as being the primary dynamical structures responsible for streak formation and turbulence generation [Jimenez and Pinelli, 1999], and these are interpreted by some as being the tails of hair-pin vortices [Adrian and Meinhart, 2000]. Fig. 3.1 shows the Q iso-surface criterion in the domain, highlighting the turbulent structures in the supersonic turbulent channel flow. The temperature distribution is given in both $x-y$ and $y-z$. Temperature fluctuations in the near wall region are also presented showing the typical streamwise elongated patterns connected to the high-speed and low-speed streaks.

3.2.3. Turbulence statistics

Statistical quantities are computed by time-averaging over a sampling period τ_s , which accounts for 250 non-dimensional time units, and spatial-averaging in the homogeneous direction z . A general Reynolds average quantity noted as $\langle \phi \rangle$ is defined as:

$$\langle \phi(y) \rangle = \frac{1}{L_x} \frac{1}{L_z} \frac{1}{\tau_s} \int_{L_x} \int_{L_z} \int_{\tau_s} \phi(x, y, z, t) dx dz dt. \quad (3.1)$$

Favre-average quantities are obtained from Reynolds averaged values through the following relationship:

$$\{\phi\} = \frac{\langle \rho \phi \rangle}{\langle \rho \rangle} \quad (3.2)$$

$$\{\phi'' \phi''\} = \langle \rho \phi \phi \rangle - \frac{\langle \phi \phi \rangle \langle \rho \phi \rangle}{\langle \rho \rangle}. \quad (3.3)$$

DNS results comparison

Table 3.3 shows slight differences in terms of mean flow properties between the DNS of [Coleman et al., 1995] and our DNS results. In our case the friction-velocity Reynolds number Re_τ is smaller and accordingly the centerline temperature T_c is higher. These difference may be due to the different numerical method (spectral Fourier-Legendre space differentiation and third-order time integration for [Coleman et al., 1995]), but may also arise from the different definition of the forcing f_{pg} .

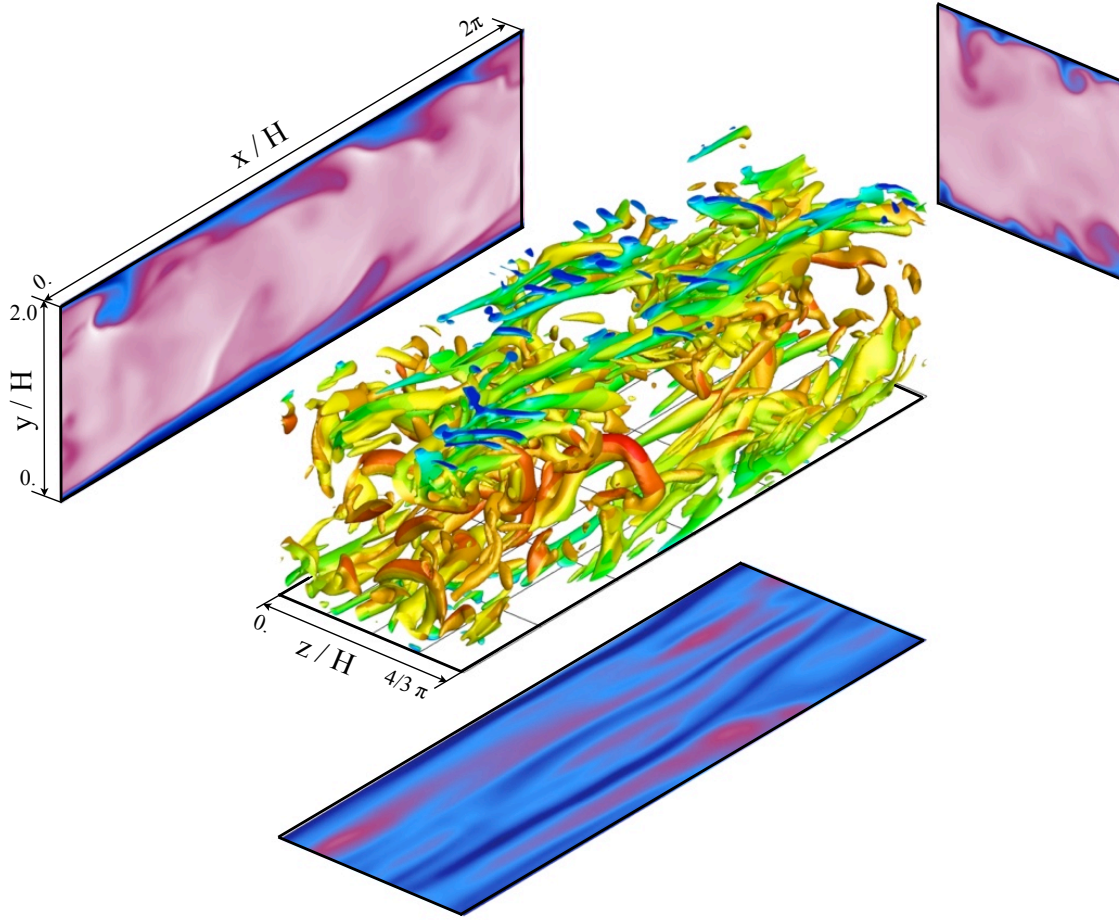


Figure 3.1.: Instantaneous flowfield obtained from the supersonic turbulent channel flow DNS. (center) Q-criterion iso-surface colored with streamwise velocity. (top) Instantaneous temperature field in the $x - y$ and $y - z$ plane. (bottom) Temperature fluctuations in the $x - z$ plane at $y^+ \approx 10$.

The comparison between the DNS computations in terms of mean van-Driest transformed streamwise velocity $\langle u_{1,VD}^+ \rangle$, given in Fig. 3.2(a), shows a perfect overlapping. A strong discrepancy is visible for the mean wall normal velocity $\langle u_2 \rangle$, given in Fig. 3.2(b). The centerline wall-normal velocity for the reference DNS of [Coleman et al., 1995] does not reach a zero value, clearly highlighting that these results cannot be considered as fully converged. Our computation, on the other hand, shows a zero value for the wall-normal velocity in the middle of the domain, clearly certifying that the averaging procedure has been conducted for a sufficient amount of time. Finally, Fig. 3.2(c) and Fig. 3.2(d) show the distribution of the mean temperature $\langle T \rangle$ and mean Mach number $\langle Ma \rangle$, respectively. The comparison has been carried out also in terms of Reynolds-stresses, shown in Fig. 3.3(a) and Fig. 3.3(b). Our DNS shows slightly higher values for fluctuations in the near wall region compared to

the results of [Coleman et al., 1995]. The maximum level of discrepancy, however, is kept below 3%.

A clear statement cannot be made concerning the origin of this small discrepancies between the DNS computations described above. Both the different numerical approach and the insufficient averaging time adopted in the work of [Coleman et al., 1995] could be indicated as sources of these small differences.

Implicit LES results

The original ALDM formulation has been compared with the extensions featuring the van-Driest (ALDM-VD) and the coherent structures (ALDM-CS) damping approaches. The analysis has been carried out for every grid resolution level. Table 3.3 shows the mean flow properties obtained for the implicit-LES computations performed using different grid resolutions. As expected, the worse prediction in terms of friction Reynolds number Re_τ is obtained for the original ALDM formulation without the addition of damping procedures. A certain increase is achievable when using the van-Driest based damping approach, which overall allows for an increment in terms of friction Reynolds number value of approximately 1% with respect to the unmodified formulation. The best performance is obtained when resorting to the coherent structures based damping formulation, which allows for an improvement of the prediction with respect to the original ALDM of approximately 4%. It is worth mentioning that the computation carried out using the ALDM-CS method on the lower resolution grid (L1), delivers a predicted value of the friction Reynolds number closer to the DNS result with respect to the other two computations carried out using the original ALDM and the ALDM-VD approaches on the higher resolution grid (L2). A similar trend is obtained for the mean centerline temperature $\langle T_c \rangle$, even if the deviation with respect to the DNS results is significantly smaller.

Figures 3.4(a) and 3.4(b) show comparisons between DNS and LES data for the mean streamwise velocity profile in van-Driest scaling $\langle u_{1,VD}^+ \rangle$ versus the wall coordinate $y^+ = y u_\tau (\rho_w / \mu_w)$. For both grid configurations L1 and L2, the underprediction of the friction velocity delivered by the original ALDM and the ALDM-VD approaches directly reflects on the van-Driest transformed velocity, which is overestimated in both the logarithmic and wake region. A significant improvement is clearly visible when adopting the ALDM-CS method which delivers the best prediction for both grid resolution levels.

Computational results for the Reynolds stresses are shown in Figs. 3.5(a) - 3.5(b) - 3.5(c) - 3.5(d). A similar trend is visible as before. Both the original ALDM and the ALDM-VD versions underpredict the Reynolds stresses with respect to the DNS reference results. Better agreement is achieved with the ALDM-CS formulation. The inset given in Figs. 3.5(a) and 3.5(b) shows the wall-normal and spanwise velocity fluctuations. In this case, the discrepancies with respect to the DNS data are stronger for the original ALDM and ALDM-VD version while the ALDM-CS approach delivers satisfactory results.

Values for the turbulent heat flux are also given in Fig. 3.6(a) and 3.6(b). In both

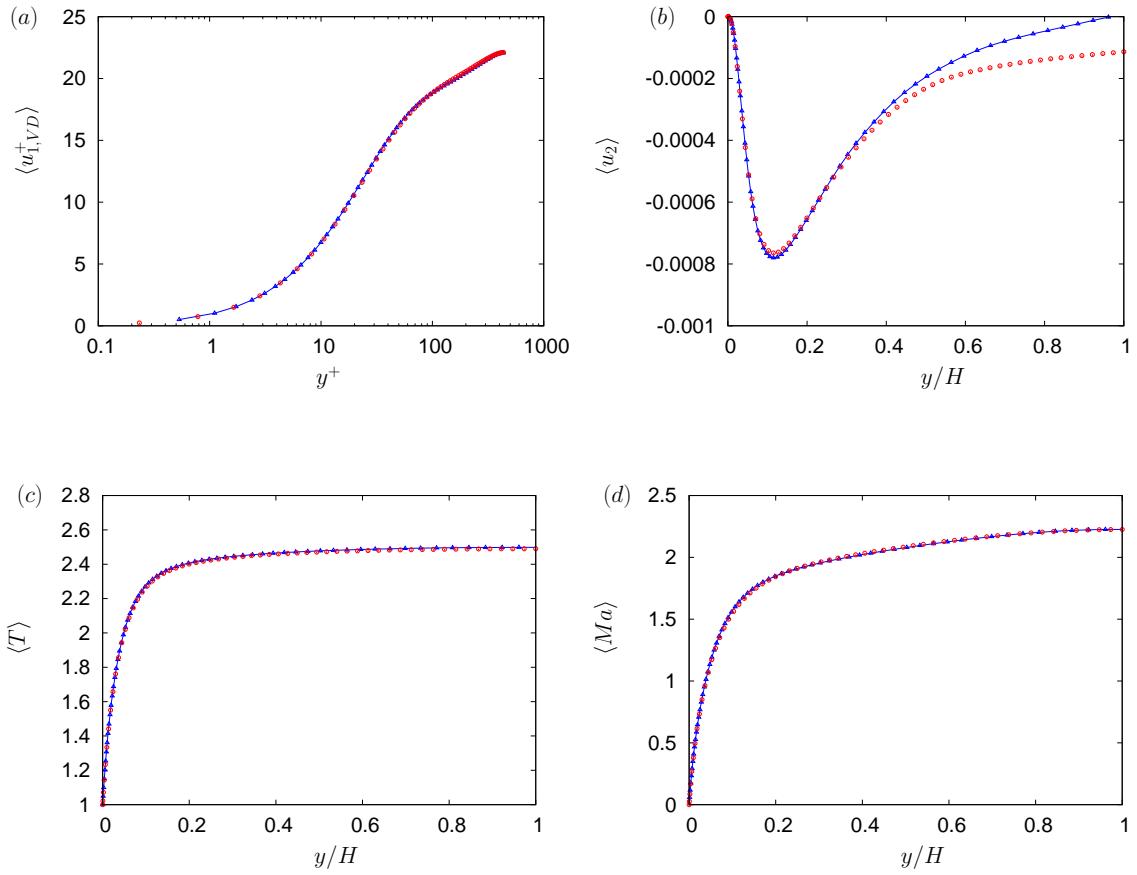


Figure 3.2.: DNS results comparison. (a) Mean van-Driest scaled velocity $\langle u_{1,VD}^+ \rangle$, (b) mean wall normal velocity $\langle u_2 \rangle$, (c) mean temperature $\langle T \rangle$, (d) mean Mach number $\langle Ma \rangle$.

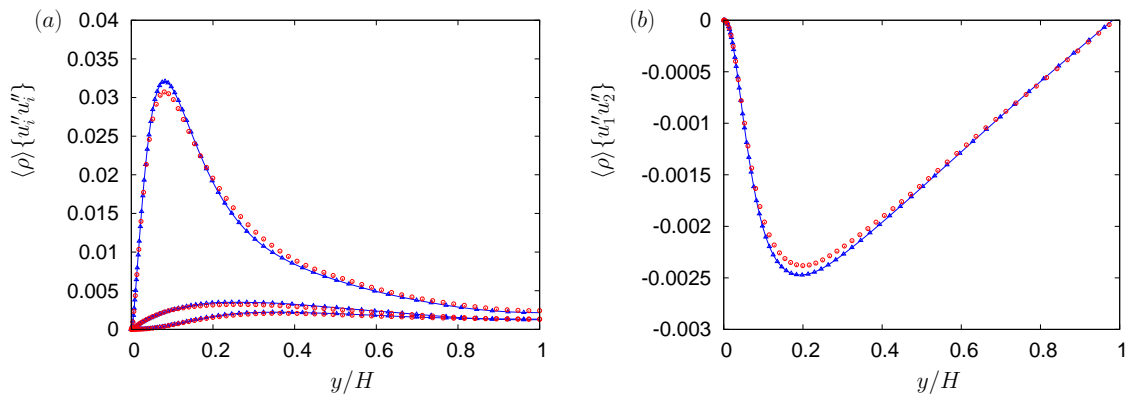


Figure 3.3.: DNS results comparison. Velocity fluctuations.

3. Numerical approach validation

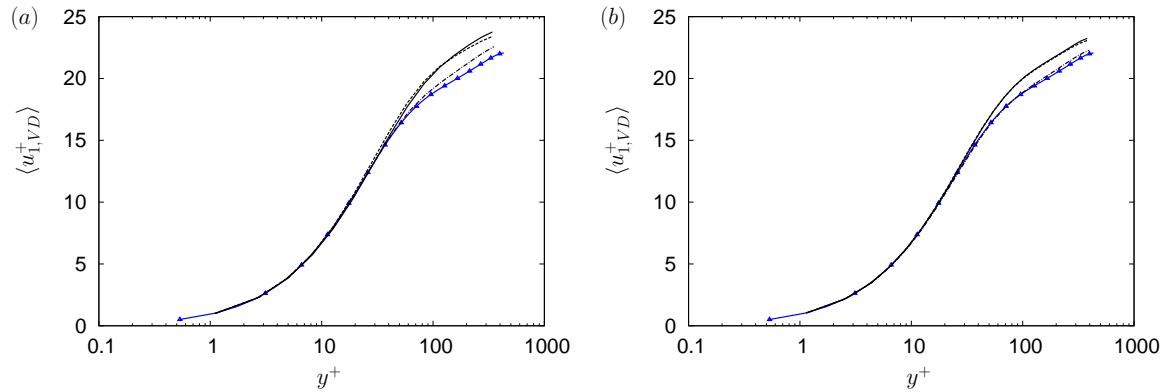


Figure 3.4.: Mean van-Driest transformed velocity $\langle u_{1,VD}^+ \rangle$ for the LES of a supersonic turbulent channel flow at $Re = 4880$ and $Ma = 3.0$. (a) L1 grid. (b) L2 grid.

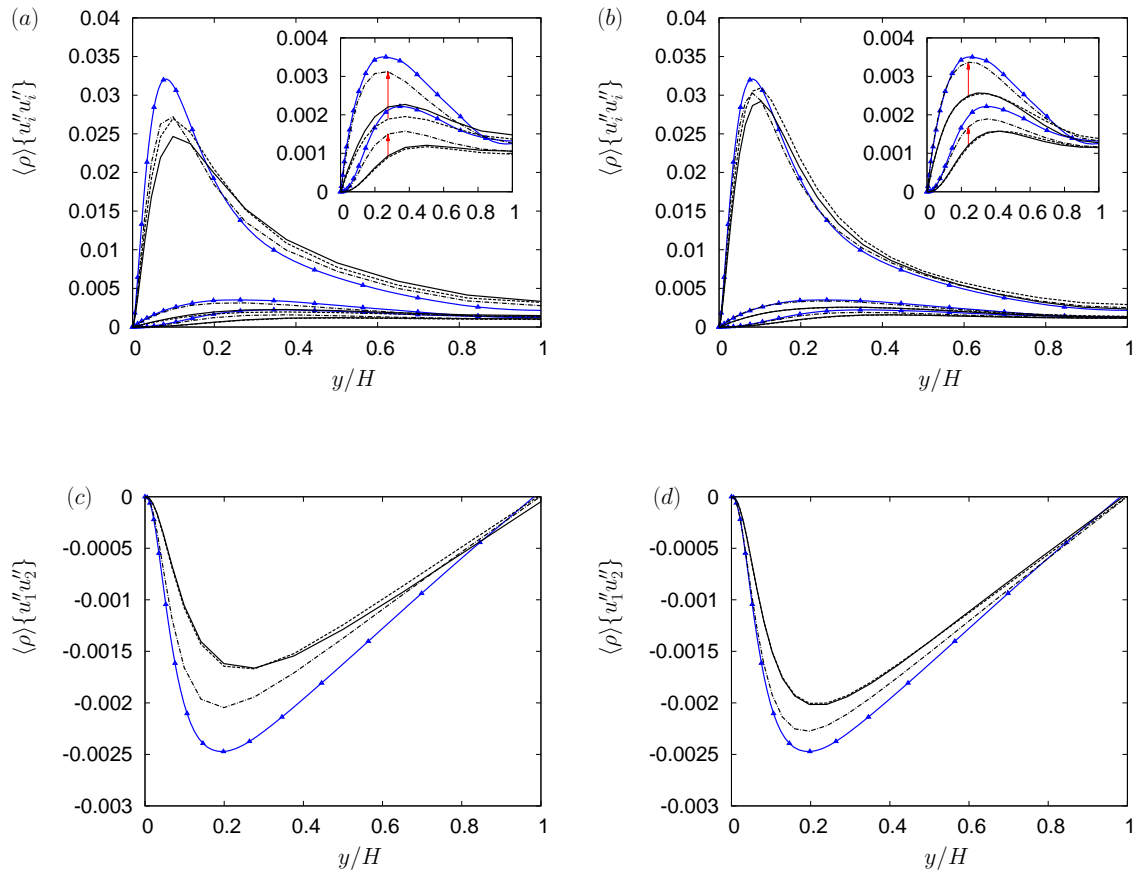


Figure 3.5.: (a)-(b) Streamwise, wall normal and spanwise velocity fluctuations for the L1 grid (left) and L2 grid (right). (c)-(d) Turbulent shear stress.

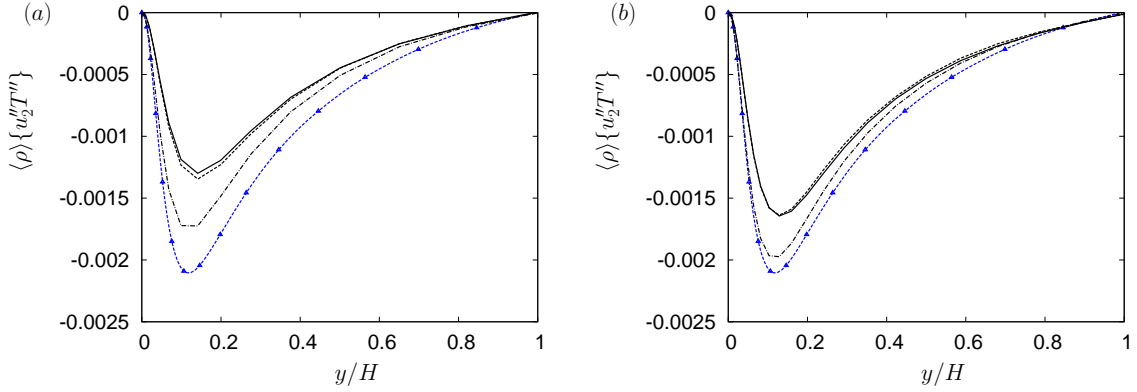


Figure 3.6.: Turbulent heat flux for the L1 grid (a) and L2 grid (b).

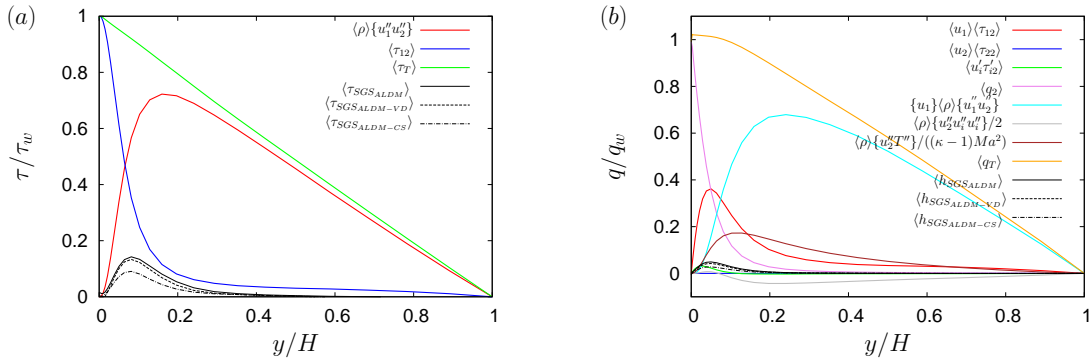


Figure 3.7.: Contribution of the sub-grid scale term to the global shear-stress balance (a) and to the total heat flux (b) for the L2 grid configuration.

cases the ALDM-CS version outperforms the original ALDM and the ALDM-VD approaches. It is also worth noticing that also in this case the computation carried out on the L1 grid using the ALDM-CS formulation is capable of delivering a better prediction than the one obtained from the original ALDM and ALDM-VD on the L2 grid. Finally, Figs. 3.7(a) and 3.7(b) show the contribution of the subgrid-scale term to the total shear stress balance and the total heat flux balance. The differences between the different ALDM formulations are located in the near-wall region ($y/H < 0.3$). The adoption of the ALDM-VD approach brings about only a moderate reduction of the dissipation provided by the implicit method. An improved reduction of the subgrid-scale term in the near-wall region is achieved when employing the ALDM-CS approach, which delivers a decrease of the peak value for the dissipation of around 40%. These results are consistent with the increased level of turbulent fluctuations obtained for the ALDM-CS formulation in the near-wall region.

3.3. Supersonic turbulent boundary layer flow

Further assessment of the implicit-LES modeling approach has been carried out by comparing the original ALDM formulation with the van-Driest and coherent structures damping procedures for the supersonic turbulent boundary layer flow configuration. A resolution study has been performed considering only the numerical setup consisting of the coupling of the original ALDM with the coherent structures damping approach.

3.3.1. Numerical method

The convective fluxes are discretized using the Adaptive Local Deconvolution Method. The viscous fluxes are discretized using a second-order central differences scheme. Time advancement is achieved by a third-order TVD explicit Runge-Kutta [Shu, 1988]. At the bottom of the computational domain, an isothermal no-slip boundary condition is imposed, with the wall temperature assumed to be equal to $T_w/T_{ref} = 1.717$, while an extrapolation based on Riemann invariants is adopted at the upper boundary. At the outlet, an extrapolation condition is used, and at the inlet, an inflow turbulent boundary condition, relying on a modified version of the digital-filter procedure proposed by [Touber, 2009]. Mean values and rms values needed for the digital filter procedure are directly extracted from the DNS database of [Pirozzoli and Bernardini, 2011]. Details about the filtering properties adopted in this study are given in Tab. 3.4.

3.3.2. Problem setup

The incoming boundary layer is spatially evolving at a freestream Mach number, $M_\infty = 2.0$, and an inlet Reynolds number, $Re_\tau^{in} = \rho_w u_\tau \delta_0^{in} / \mu_w = 251$ or $Re_\theta^{in} = \rho_\infty u_\infty \theta^{in} / \mu_\infty = 1121.0$ (where u_τ is the friction velocity, δ_0^{in} is the inflow boundary layer thickness, and θ^{in} is the momentum thickness at the inlet). The computational domain

Table 3.4.: Digital-Filter procedure parameters.

Velocity component	u_1	u_2	u_3
I_x in δ_1^{VD} ^a	10	4	4
$N_{F_y}^b = 2 I_y / \Delta_y$	35 ^c -65 ^d	45 ^c -85 ^d	30 ^c -40 ^d
$N_{F_z}^b = 2 I_z / \Delta_z$	15	15	30

(^a) van-Driest displacement thickness $\delta_1^{VD} = \int_0^\infty [1 - u_{1,VD}] dy$.
(^b) number of grid points derived from specified integral length scales I_y, I_z .
(^c) Filter length for the lower region $y \leq \delta_1^{VD}$.
(^d) Filter length for the upper region $y > \delta_1^{VD}$.

Table 3.5.: Lines and symbols for the different cases.

Case	Symbol
DNS [Pirozzoli and Bernardini, 2011]	○
LES (ALDM) ^a	—
LES (ALDM-VD) ^b	----
LES (ALDM-CS) ^c	· · ·

(^a) Original ALDM formulation for compressible flows as proposed in [Hickel, 2012].
(^b) ALDM with van-Driest formulation for wall-damping.
(^c) ALDM with coherent structures damping approach.

Table 3.6.: Grid resolutions study using ALDM-CS.

Case	Line	N_x	N_y	N_z	Δx^+	Δy^+	Δz^+	β^a
LES (L1)	—	320	170	86	40.0	0.8	15.0	4.7
LES (L2)	—	640	170	86	20.0	0.8	7.0	4.7
LES (L3)	—	320	170	172	40.0	0.8	8.0	4.7
LES (L4)	—	640	170	172	20.0	0.8	8.0	4.7

(^a) hyperbolic sine bunching law in the y -direction
 $y(i) = \sinh(\beta(i-1)/(N_y-1))/(\sinh \beta)$

used in this study has a size of $L_x \times L_y \times L_z = 50.0 \delta_0^{in} \times 6.0 \delta_0^{in} \times 4.8 \delta_0^{in}$ in the streamwise (x), wall-normal (y) and spanwise (z) directions, respectively. As shown in Tab. 3.6, different grid resolutions are used with uniformly spaced grid in the streamwise and spanwise directions, and clustered grid in the wall-normal direction based on an hyperbolic tangent function.

The flowfield is initialized using the inlet values. A series of approximately 200 characteristic times, $t_c = \delta_0^{in}/u_\infty$, is achieved to sweep the initial transient solution. Then, turbulence statistics are sampled and extracted at a constant time interval of $\Delta t_c = 0.2$ from a time series covering a total time span of $t_c^{tot} = 600$. By plotting the time evolution of the main boundary layer, such as the boundary layer thickness and the friction velocity, this sampling time is judged to be sufficient to reach a statistical convergence of the considered quantities.

3.3.3. Flow description

In turbulent boundary layer flows, the near-wall region is characterized by the presence of alternating streaks of high- and low-speed fluid. These streaks originate

3. Numerical approach validation

from elongated, counter-rotating streamwise vortices near the wall. These structures significantly contribute to the turbulence production, which occurs because of a bursting process where low-speed streaks gradually lift up from the wall, oscillate, and then break up violently, ejecting fluid away from the wall into the outer layer [Smits and Dussauge, 2006]. In order to show the turbulent nature of the flow in the near-wall region wall parallel slices of velocity and temperature fluctuations are shown in Fig. 3.8-(a) at $y^+ \approx 10$. This data are obtained from the LES computation carried out with the grid configuration L4 and using the ALDM combined with the coherent structures damping approach. As shown in the work of [Pirozzoli and Bernardini, 2011], Fig. 3.8-(a) shows typical alternating high- and low-speed streaks, which correspond to positive and negative velocity fluctuations, respectively. It is also worth to underline the large number of streaks in the spanwise direction (z), which is an indicator of the sufficient width of the domain in this direction. Indeed, a sufficient resolved number of streaks means that the flow is not confined in the spanwise direction, and that turbulence mechanisms are not inhibited by the domain extent [Jimenez and Moin, 1991]. Velocity fluctuations in the outer layer at $y^+ \approx 100$ are shown in Fig. 3.8-(b). At this location the flow features the presence of large scale structures which are responsible for the large-scale transport of turbulence in the outer layer [Smits and Dussauge, 2006]. Fig. 3.9 draws the Q iso-surface criterion in the second half of the domain colored by the u_1 velocity field. The figure shows highly turbulent structures inclined with respect to the wall in the downstream direction and featuring a strongly intermittent character.

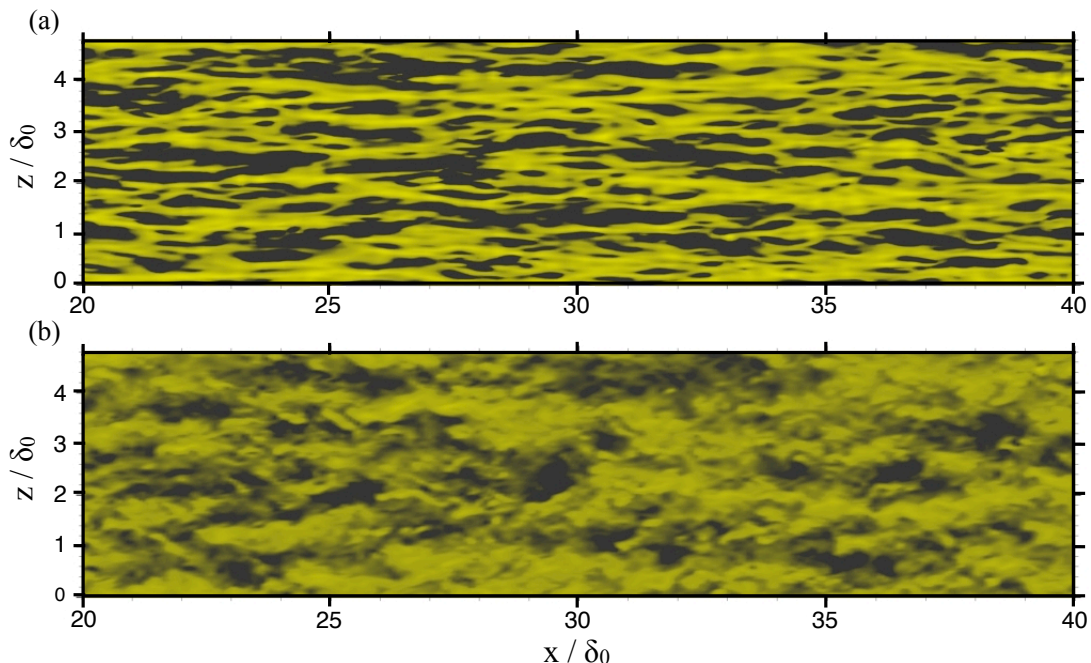


Figure 3.8.: (a) Instantaneous velocity fluctuations at $y^+ \approx 10$. (b) Instantaneous velocity fluctuations at $y^+ \approx 100$.

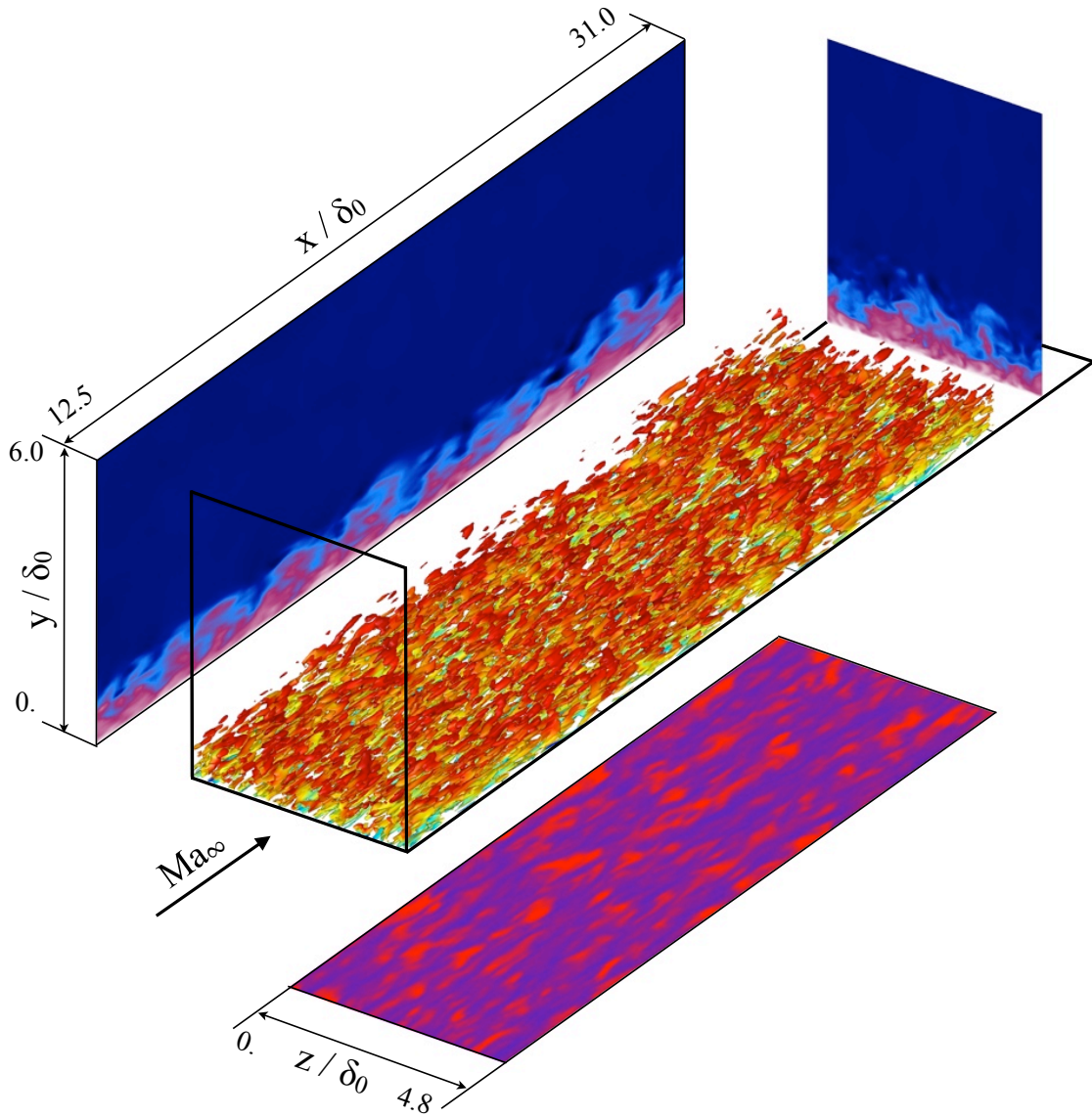


Figure 3.9.: Instantaneous flowfield obtained from the L4 grid using the ALDM-CS formulation. (center) Q-criterion iso-surface colored with streamwise velocity. (top) Instantaneous temperature field in the $x - y$ and $y - z$ plane. (bottom) Temperature fluctuations in the $x - z$ plane at $y^+ \approx 10$.

3.3.4. Turbulence statistics

In the following section, statistical quantities are obtained by time-averaging over a sampling period τ_s and spatial-averaging in the homogeneous direction z . A general Reynolds average quantity noted as $\langle \phi \rangle$ is defined as:

$$\langle \phi(x, y) \rangle = \frac{1}{L_z} \frac{1}{\tau_s} \int_{L_z} \int_{\tau_s} \phi(x, y, z, t) dz dt. \quad (3.4)$$

Wall properties

Figures 3.10(a)-3.10(b) show the incompressible skin-friction distribution, $C_{f_{inc}}$, as a function of the Reynolds number based on the incompressible momentum thickness $Re_{\theta_{inc}}$. Results are compared to formulas given by [Smits et al., 1983], Kármán-Schoenherr, as well as to DNS data of [Guarini et al., 2000], [Maeder et al., 2001], [Pirozzoli et al., 2004] and [Pirozzoli and Bernardini, 2011]. The skin-friction coefficient, $C_{f_{inc}}$, and the Reynolds number, $Re_{\theta_{inc}}$, are calculated using the van-Driest II theory for an isothermal wall ([Pirozzoli et al., 2004] and [Pirozzoli and Bernardini, 2011]), which is found to be a reliable transformation for collapsing data at different Mach flow regimes:

$$C_{f_{inc}} = F_C C_f \quad Re_{\theta_{inc}} = F_\theta Re_\theta, \quad (3.5)$$

with the transformation functions, F_C and F_θ , are:

$$F_C = \frac{T_w/T_\infty - 1}{\arcsin^2 \alpha} \quad F_\theta = \frac{\mu_\infty}{\mu_w} \quad (3.6)$$

where

$$\alpha = \frac{T_w/T_\infty - 1}{\sqrt{T_w/T_\infty (T_w/T_\infty - 1)}}. \quad (3.7)$$

The incompressible friction coefficient correlations used in Figs. 3.10(a) - 3.10(b) are given by:

$$C_{f_{inc,S}} = 0.024 Re_{\theta_{inc}}^{-1/4} \quad (3.8)$$

$$C_{f_{inc,B}} = 0.026 Re_{\theta_{inc}}^{-1/4} \quad (3.9)$$

$$C_{f_{inc,KS}} = \frac{1}{17.08 (\log_{10} Re_{\theta_{inc}})^2 + 25.11 (\log_{10} Re_{\theta_{inc}}) + 6.012}, \quad (3.10)$$

where the subscripts B , S and KS refer to the empirical correlations of Blasius, [Smits et al., 1983], and Kármán-Schoenherr, respectively.

Figure 3.10(a) shows that the the ALDM-CS delivers a slight overestimated value for the skin-friction coefficient, $C_{f_{inc}}$, when compared with empirical correlations and DNS data. The ALDM and ALDM-VD formulations tend also to overpredict the local friction coefficient and their difference with respect to the ALDM-CS formulation is around 1.5%, for the ALDM-VD, and 2.5%, for the ALDM original version, respectively. The grid sensitivity study, given in Fig. 3.10(b), shows that the ALDM-CS formulation delivers a value for the skin-friction coefficient which always lies in the region contained between the Blasius's and Kármán-Schoenherr's empirical relations. The increase of the resolution strongly reduces the difference with respect to the DNS data provided by [Pirozzoli and Bernardini, 2011]. Fig. 3.10(b) also shows that an increment of the resolution in the streamwise direction delivers a better improvement in terms of skin-friction coefficient prediction with respect to an increase of the resolution in the spanwise direction. By doubling the number of grid points in

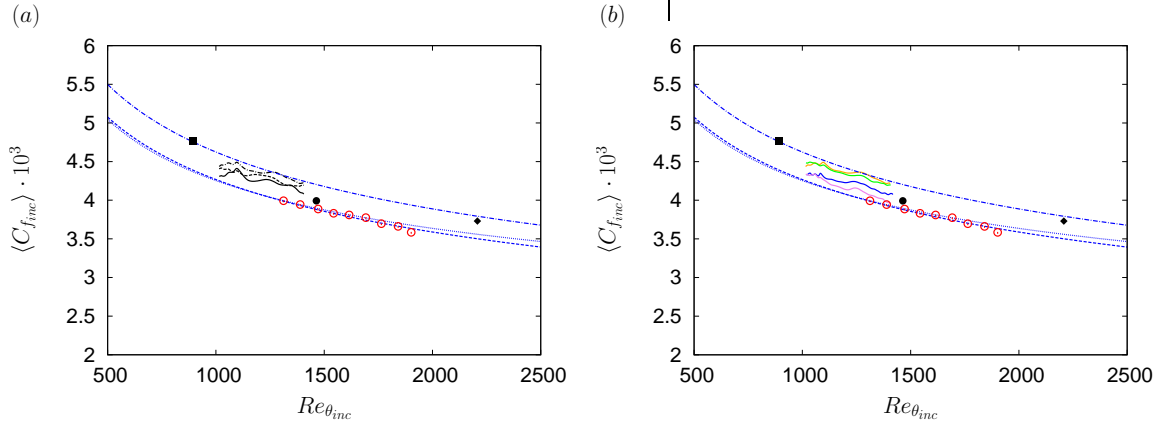


Figure 3.10.: Incompressible skin-friction coefficient $C_{f_{inc}}$ as a function of the Reynolds number based on incompressible momentum thickness $Re_{\theta_{inc}}$. (---) Blasius, (----) Smits, (.....) Kármán-Schoenherr. (○) [Pirozzoli and Bernardini, 2011] ($Ma = 2$), (■) ($Ma = 2.5$) [Guarini et al., 2000], (◆) ($Ma = 2.25$) [Pirozzoli et al., 2004], (●) ($Ma = 3.0$) [Maeder et al., 2001]. (a) Comparison between the different LES formulations with the L1 grid. (b) Grid sensitivity study.

the streamwise direction, we obtain a reduction of the $C_{f_{inc}}$ of around 4% while the increase of the number of grid points in the spanwise direction delivers a decrement of the skin-friction value which is found to be below 1%.

Mean flow properties

The van-Driest transformed mean streamwise velocity $\langle u_{1,VD}^+ \rangle$, which accounts for the variation of the mean flow properties aiming to collapse a compressible velocity profile with its incompressible counterpart, is shown as a function of y^+ in Figs. 3.11(a) and 3.11(b). In accordance with what has been shown for the compressible turbulent channel flow computation, we can see that an under-estimation of the friction velocity u_τ has a direct impact on the predictions obtained for the original ALDM and the ALDM-VD approaches. In the viscous sub-layer and up to the beginning of the buffer region ($y^+ < 10$), all models collapse on the DNS data. In the buffer region ($20 < y^+ < 100$) the slope of the profile is correctly reproduced by all the different models employed. However, a slightly better agreement with the DNS data is achieved for the ALDM-CS formulation. In the wake region ($y^+ > 100$) the ALDM-CS approach shows a slight underestimation of $\langle u_{1,VD}^+ \rangle$, while a better prediction is obtained from both the ALDM-VD and original ALDM approach.

Fig. 3.11(b) shows the sensitivity study carried out on the ALDM-CS approach. All of the predicted values collapse on the DNS prediction, even if a slight improvement of the results is obtained for higher resolution computations in the wake region.

3. Numerical approach validation

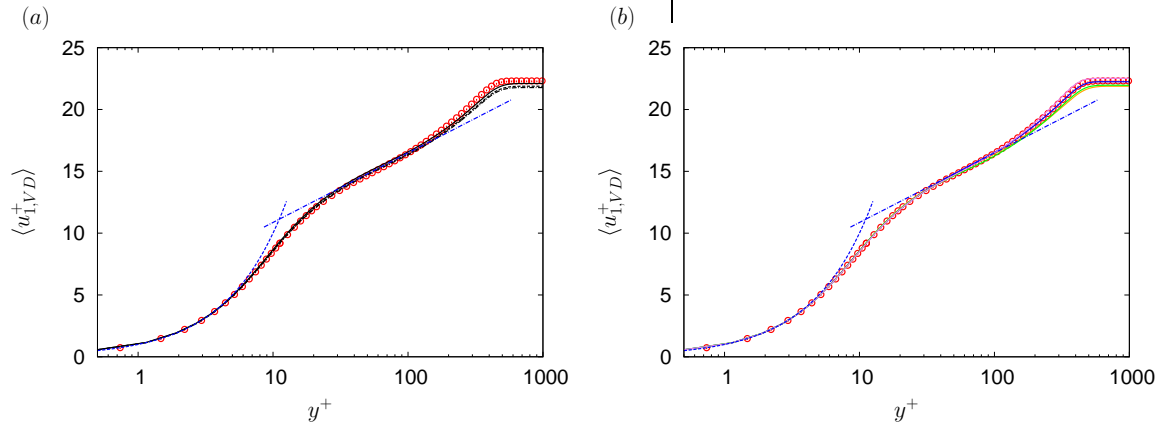


Figure 3.11.: Mean van-Driest transformed streamwise velocity $\langle u_{1,VD}^+ \rangle$ as a function of y^+ . (---) linear-law. (---) logarithmic-law $\log(y^+)/0.41 + 5.25$. (a) Comparison between the different LES formulations with the L1 grid. (b) Grid sensitivity study.

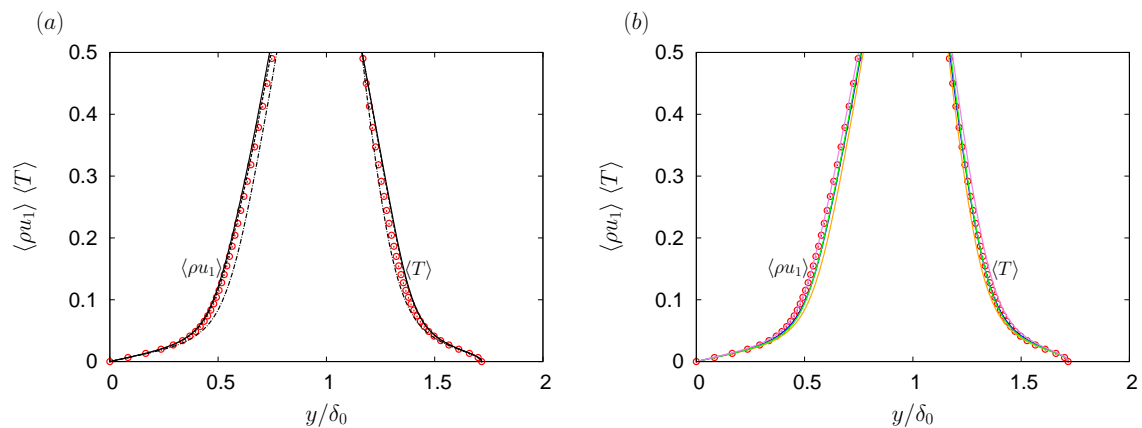


Figure 3.12.: Mean averaged mass flux $\langle \rho u_1 \rangle$ and temperature $\langle T \rangle$. (a) Comparison between the different LES formulations with the L1 grid. (b) Grid sensitivity study.

Distributions of the mean-averaged quantities as a function of y/δ_0 are plotted in Fig. 3.12(a). Overall, the predictions for both the averaged mass flux $\langle \rho u_1 \rangle$ and temperature $\langle T \rangle$ are satisfactory. The normalized temperature is slightly higher in the core for the original ALDM and the ALDM-VD formulation confirming the influence of the damping of the turbulent fluctuations in the near-wall region. The sensitivity study shown in Fig. 3.12(b) indicates how the increase of grid resolution does not have a strong influence on the first-order statistical moments prediction. Fig. 3.13(a) shows the normalized velocity fluctuations for the different LES approaches as a

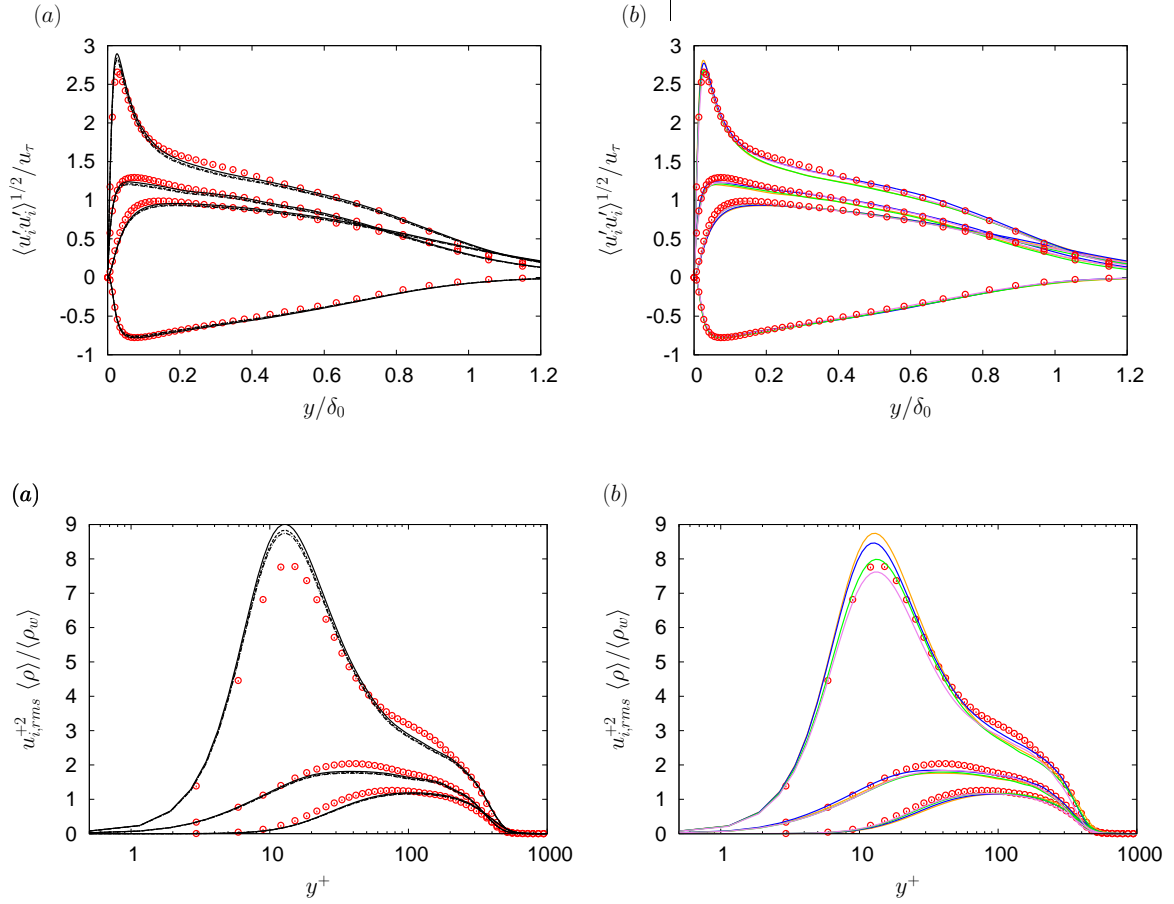


Figure 3.13.: Reynolds stresses. (a) Comparison between the different LES formulations with the L1 grid. (b) Grid sensitivity study.

function of y/δ_0 . All the formulations deliver a certain under-estimation of the velocity fluctuation in the outer-region. When considering Fig. 3.13(c), which shows the velocity fluctuations rescaled by means of the Morkovin hypothesis, we can see that the different formulations correctly predict the location of the peak in the near wall region but over-estimate the value of the streamwise velocity peak of around 10%. A considerable improvement in the second-order moment prediction for the ALDM-CS approach can be achieved by an increase in the resolution, as shown in Figs.3.13(b) and 3.13(d), which show the grid sensitivity analysis. The best results for the velocity fluctuations are obtained when increasing the resolution in the spanwise direction.

Higher-order moments, such as the skewness of the velocity fluctuations, can be calculated for better analysis of the turbulence nature from statistics view-point. By

3. Numerical approach validation

definition, the skewness coefficient of a given fluctuation of a quantity ϕ' is given as:

$$S(\phi') = \frac{\langle \phi'^3 \rangle}{\langle \phi'^2 \rangle^{3/2}} \quad (3.11)$$

Fig. 3.14(a) shows the prediction in terms of velocity skewness $S(u'_1)$ obtained for the several implicit-LES approaches considered. Apart from the near-wall deviation of the skewness coefficient, the turbulence behavior is found to be nearly Gaussian, with $S(u'_1) \approx 0$ (slightly negative). A similar behavior can be seen for the skewness of the temperature fluctuation. In this case the grid resolution study shows a slight improvement in the prediction accuracy of the skewness factors for velocity and

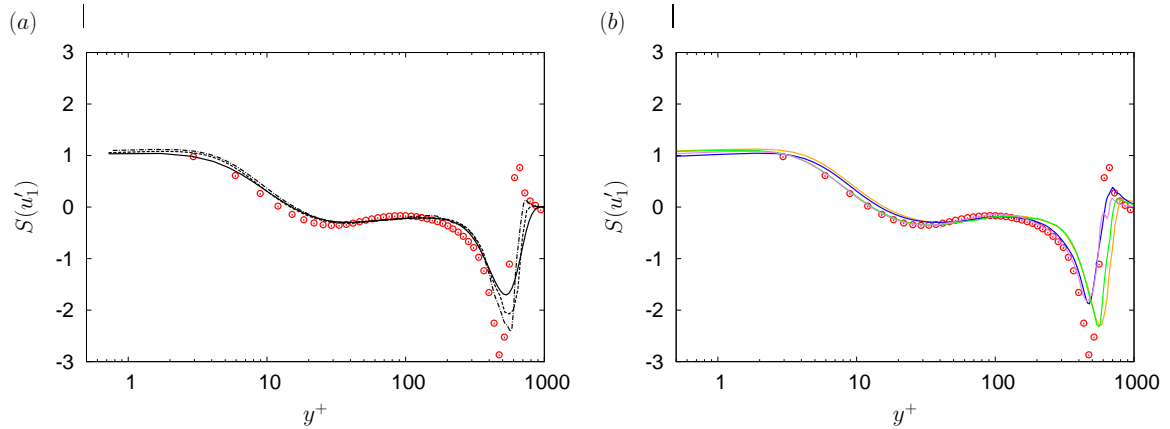


Figure 3.14.: Streamwise velocity u_1 skewness. (a) Comparison between the different LES formulations with the L1 grid. (b) Grid sensitivity study.

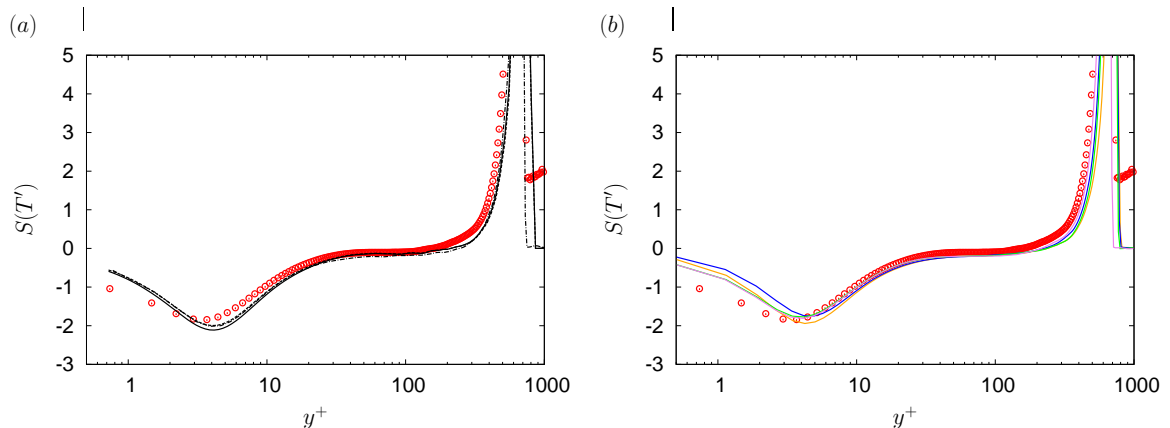


Figure 3.15.: Temperature T skewness. (a) Comparison between the different LES formulations with the L1 grid. (b) Grid sensitivity study.

temperature. It has to be noted that a large dataset of snapshots has to be gathered in order to achieve the convergence of the results concerning the skewness factors.

3.4. CIIM validation cases

In order to perform the validation of the conservative immersed interface method several test cases have been taken into account. A thorough analysis of the accuracy of interface interaction model has been carried out by considering viscous laminar flows. Computations with stationary and moving boundaries problems are performed. For discretization in space a 5th-order WENO scheme with a local Lax Friedrichs numerical flux function [Jiang and Shu, 1998] is used for the convective terms and a second-order accurate Central Difference Scheme (CDS) for the viscous terms. Time advancement is performed using a third-order explicit three step Runge-Kutta scheme [Shu, 1988].

First, results for simulations of steady and unsteady low Mach number laminar flows over a circular cylinder are presented. We consider laminar flows in steady and vortex-shedding regimes for Reynolds numbers in the range between $Re_D = 40$ and $Re_D = 150$. A rather low Mach number, $Ma = 0.3$, has been chosen to meet with incompressible nature of the experimental data. The flow over a circular cylinder is a suitable validation test case, since the flow field exhibits different regimes depending on the Reynolds number, and the curved boundary is challenging for Cartesian grid methods. Furthermore, a huge amount of reference data is available from literature.

Afterwards, the focus is moved towards the laminar boundary layer flow over a compression corner at $Ma = 6.06$. More details about the flow configuration will be given in the dedicated section. The aim of this computation is to validate the immersed interface method also in the supersonic regime where compressibility effects play an important role.

A final validation of the presented method is achieved by computing the flow in a square surface cavity located in a low Reynolds number $Ma = 8.9$ external flow.

3.4.1. Steady flow over a circular cylinder at $Re_D = 40$

At $Re = 40$ laminar separation occurs on the leeward side of the cylinder, generating a pair of vortices that are symmetrically attached to the cylinder. The computational domain and grid adopted for the calculation are shown in Figs. 3.16 Fig. 3.17, respectively. At the inflow boundary the freestream values of the conservative variables are prescribed, while a linear extrapolation boundary condition is used at the outflow. On the upper and lower wall a slip boundary condition is imposed. A sponge layer of length $L_s = 5D$ is applied at the inflow and at the outflow boundary to absorb spurious waves. The sponge layer drives the solution variables towards the free-stream values.

The present case has also been used to analyze the convergence order of the immersed interface method. Computations have been carried out on four grids with different resolutions. All grids have uniform spacing and square cells in the region occupied by the cylinder. Points from the outer region of the computational domain are then clustered towards this inner square region by means of a linear distribution. Details about the different grid resolutions are given in Table 3.7. The solution

Table 3.7.: Grid sizes and number of points n along the diameter.

$N_x \times N_y$	n
140×80	20
280×160	40
420×240	60
560×320	80

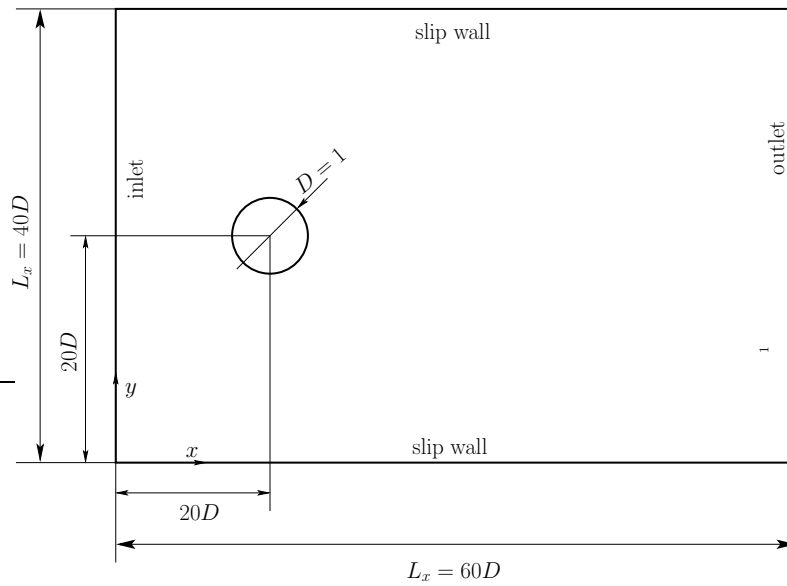


Figure 3.16.: Computational domain for the flow over a circular cylinder.

from the finest grid is taken as reference for the error estimation. This result is in good agreement with the DNS data. The peak position of both factors is correctly recovered by the LES, whereas their magnitudes are slightly over-estimated.

Fig. 3.18 shows the velocity contours and the mean streamlines. The geometrical properties of the symmetrical vortices, as defined in Fig. 3.18, and the drag coefficient C_D , are summarized in Table 3.8. Experimental and numerical results from the literature are also given for comparison. The present results are in good agreement with the references. In Fig. 3.19 the surface pressure coefficient $C_p = 2 \cdot (p - p_\infty) / (\rho_\infty U_\infty^2)$, computed directly from the interface interaction pressure, is compared with experimental and numerical results. Fig. 3.20 shows the error in terms of the drag coefficient C_D for the coarser grids with respect to the finest grid. The results confirm second order convergence for integral quantities.

3. Numerical approach validation

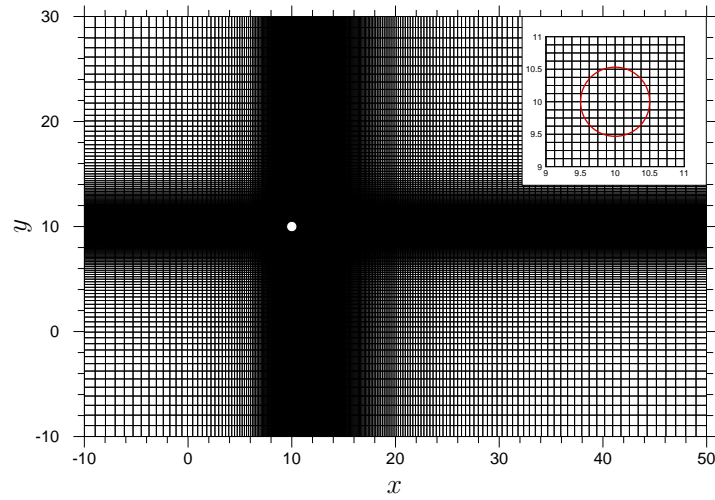


Figure 3.17.: Computational grid for the flow over a circular cylinder at $Re = 40$, $n = 40$. In the local zoomed region every 5th line is shown.

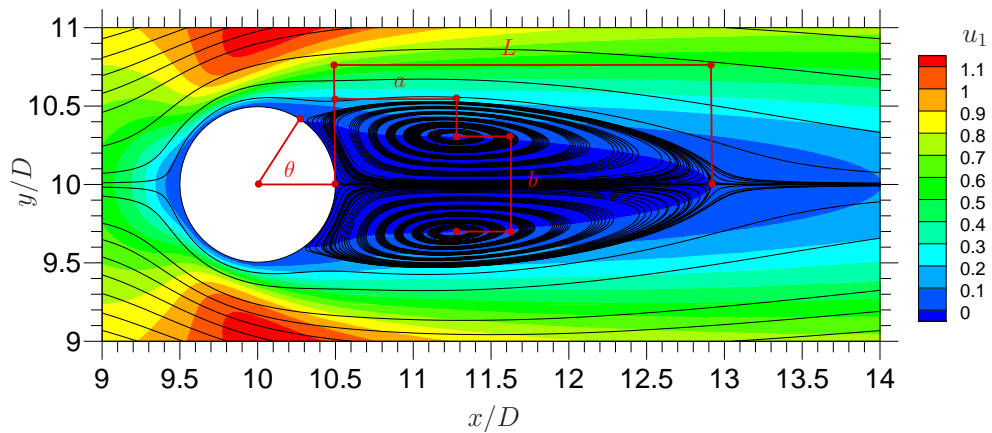


Figure 3.18.: Streamwise velocity and streamlines for the flow over a circular cylinder at $Re_D = 40$.

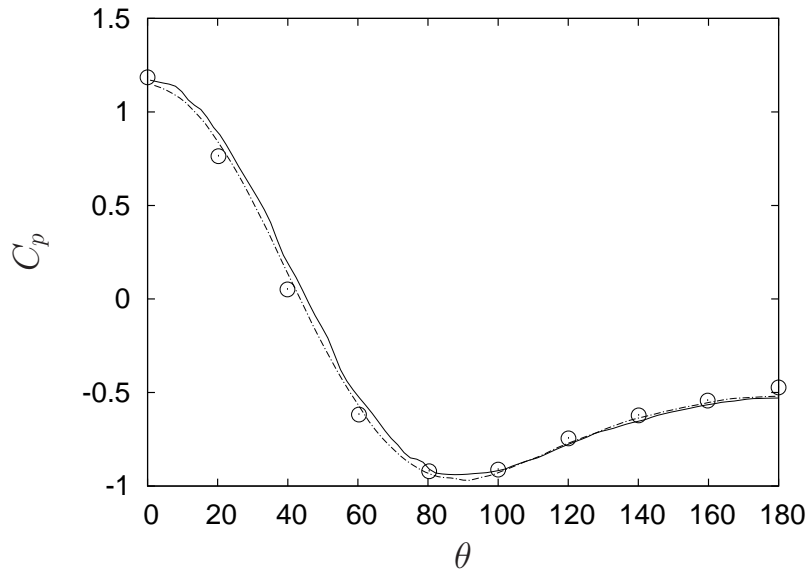


Figure 3.19.: Pressure coefficient C_p along the surface of a circular cylinder at $Re = 40$ ($\theta = 0$ in the stagnation point; \circ : experimental data Grove et al. [Grove et al., 1998], $---$: numerical computation using body-fitted from Tseng and Ferziger [Tseng and Ferziger, 2003], $—$: present method, $n = 80$).

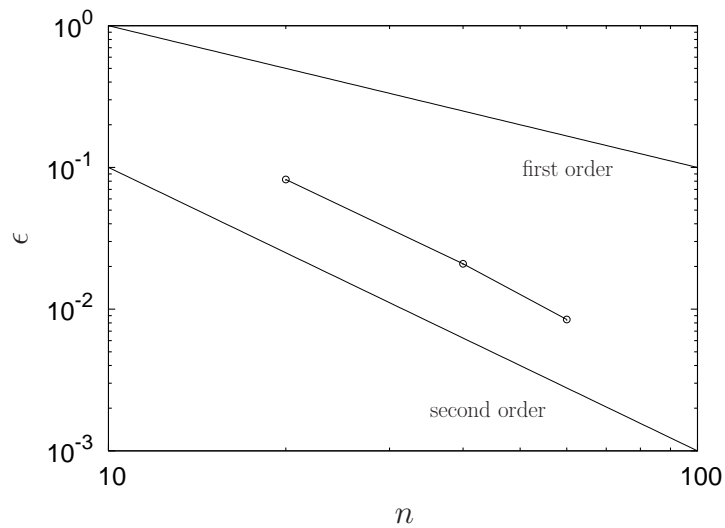


Figure 3.20.: $— \circ$ Error in C_D for the flow past a circular cylinder at $Re_D = 40$.

3. Numerical approach validation

Table 3.8.: Steady flow past a circular cylinder at $Re_D = 40$.

	L	a	b	θ	C_D
Fornberg [Fornberg, 1980] ^b	2.24	-	-	55.6°	1.50
Dennis and Chang [Dennis and Chang, 1970] ^b	2.35	-	-	53.8°	1.52
Coutanceau and Bouard [Coutanceau and Bouard, 1977] ^a	2.13	0.76	0.59	53.8°	-
Tritton [Tritton, 1959] ^a	-	-	-	-	1.59
Linnick and Fasel [Linnick, 2003] ^c	2.28	0.72	0.60	53.6°	1.54
De Palma et al. [De Palma et al., 2003] ^c	2.28	0.72	0.60	53.8°	1.55
Tseng and Ferziger [Tseng and Ferziger, 2003] ^c	2.21	-	-	-	1.53
Hartmann et al. [Hartmann et al., 2008] ^d	2.24	-	-	-	1.53
Present ^d ($n = 80$)	2.34	0.74	0.60	54.6°	1.58

^a Experimental data

^b Numerical result using body fitted grid method

^c Numerical result using an immersed boundary method

^d Numerical result using a Cartesian cut-cell method

Table 3.9.: Grid sizes and number of points n along the diameter.

$N_x \times N_y$	n
360×200	40
620×400	80

3.4.2. Unsteady flow past a circular cylinder at $Re_D = 100$

At $Re_D = 100$ the flow becomes unsteady and the cylinder wake oscillates exhibiting a wavy structure known as the von Kármán vortex street. The computational domain and the boundary conditions are the same as in the $Re_D = 40$ case. The grid has a similar topology as the one used in the previous case, the only difference is that the equidistant spacing region in the core is extended in downstream direction to account for the vortical structures in the cylinder wake.

Two computations are carried out with different grid resolutions. The properties of the grids are given in Table 3.9.

Fig. 3.21 shows the velocity contours and the mean streamlines, The drag coefficient C_D , the maximum lift coefficient C_L^{max} and the Strouhal number St are summarized in Table 3.10. Experimental and numerical results from the literature are also given for comparison. The results for the finest grid case are in good agreement with the references.

3.4.3. Vortex induced vibration of a 2-D elastically mounted cylinder

The flow over a single elastically mounted cylinder has been studied numerically by [Borazjani et al., 2008]. This case is chosen to validate the immersed interface method for moving boundary problems and viscous laminar flows. As shown in

Table 3.10.: Unsteady flow past a circular cylinder at $Re_D = 100$.

	St	C_D	C_L^{max}
Williamson [Williamson, 1996] ^a	0.164	-	-
Linnick and Fasel [Linnick, 2003] ^b	0.166	1.34 ± 0.009	± 0.333
De Palma et al. [De Palma et al., 2003] ^b	0.163	1.32 ± 0.010	± 0.331
Tseng and Ferziger [Tseng and Ferziger, 2003] ^b	-	$1.42 \pm -$	-
Hartmann et al. [Hartmann et al., 2008] ^c	0.164	$1.35 \pm -$	± 0.334
Present ^c ($n = 40$)	0.166	1.40 ± 0.015	± 0.341
Present ^d ($n = 80$)	0.166	1.38 ± 0.013	± 0.331

^a Experimental data

^b Numerical result using an immersed boundary method

^c Numerical result using a Cartesian cut-cell method

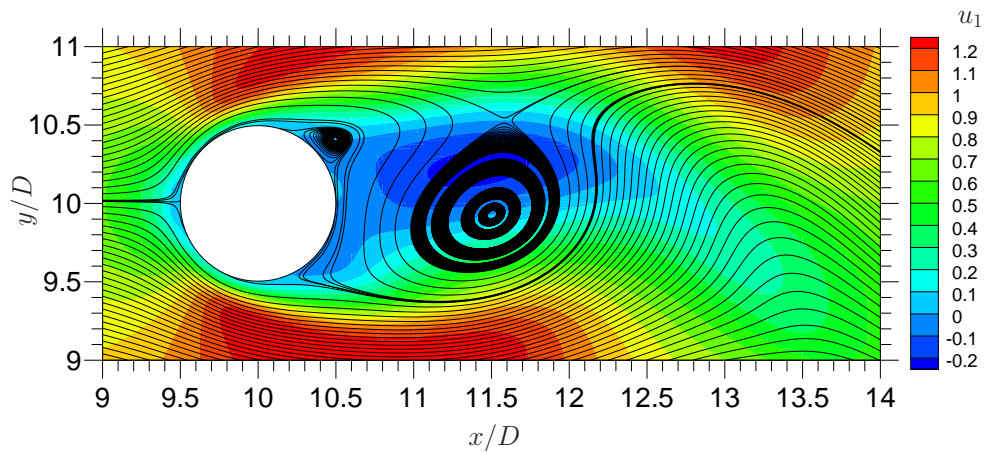


Figure 3.21.: Streamwise velocity and streamlines for the flow over a circular cylinder at $Re_D = 100$.

3. Numerical approach validation

Fig. 3.22a, a circular cylinder is mounted in a uniform flow with one degree of freedom in the y -direction, allowing for free vibration perpendicular to the flow. The equation that governs the cylinder motion in non-dimensional form is

$$\frac{\partial^2 Y}{\partial t^2} + \frac{1}{U_{red}^2} Y = \frac{1}{2M_{red}} C_Y, \quad (3.12)$$

where Y is the coordinate of the cylinder position along the y -axis normalized by the cylinder diameter D , C_Y is the lift coefficient per unit spanwise length and the reduced velocity and mass have the following definition:

$$U_{red} = \frac{U}{fD} \quad M_{red} = \frac{M}{\rho D^2}, \quad (3.13)$$

with M being the cylinder mass, K the stiffness factor of the spring and f the eigen frequency. Large-amplitude vibrations of the cylinder are induced when the eigen frequency of the cylinder falls within the so called “lock-in” region [Blevins, 1990], i.e., if the vortex-shedding frequency matches the eigen frequency [Sarpkaya, 2004, Williamson and Goverdhan, 2004]. In order to investigate the “lock in” phenomenon, we perform simulations where the Reynolds number is fixed to $Re_D = 150$ and the reduced mass of the system is set to $M_{red} = 2$ while the eigen frequency of the system is modified by varying the reduced velocity U_{red} with increments of 1 within the range $4 \leq U_{red} \leq 7$. The coupling between the fluid and the structure is done through a loose coupling strategy. The lift coefficient is computed from surface forces and the governing equation of the structure 3.12 is integrated explicitly in time without subiteration for the coupling. Two computational grids are used for the computations. The topology and the extension of the grids are the same as the ones used in the computations at $Re_D = 40$. Details about the total number of points $N_x \times N_y$ and about the actual resolution, expressed in terms of the number n of points contained in the cylinder diameter, are given in Tab. 3.11. We use the same boundary conditions as in the previous cases. The time history of the calculated cylinder location for the case with $U_{red} = 4$ and $M_{red} = 4$ is shown in Fig. 3.22 and the vorticity distribution for an instantaneous solution of the flow field is given in Fig. 3.23.

Table 3.11.: Grid details for the vortex induced vibration test case.

$N_x \times N_y$	n
140 × 115	25
280 × 230	50

Fig. 3.24 shows the variation of the maximum displacement of the cylinder $max(Y)$ for different values of U_{red} . Values in the range between $U_{red} = 4$ and $U_{red} = 7$ produce vibrations with a maximum amplitude of approximately half of the cylinder diameter. To validate the new method, Fig. 3.24 also shows results from [Borazjani et al., 2008], who also used an immersed boundary method. At lower resolution the immersed interface method underestimates the maximum displacement of the cylinder. Our method provides results that are in good agreement with those of [Borazjani et al., 2008] when the same resolution as in the reference is adopted.

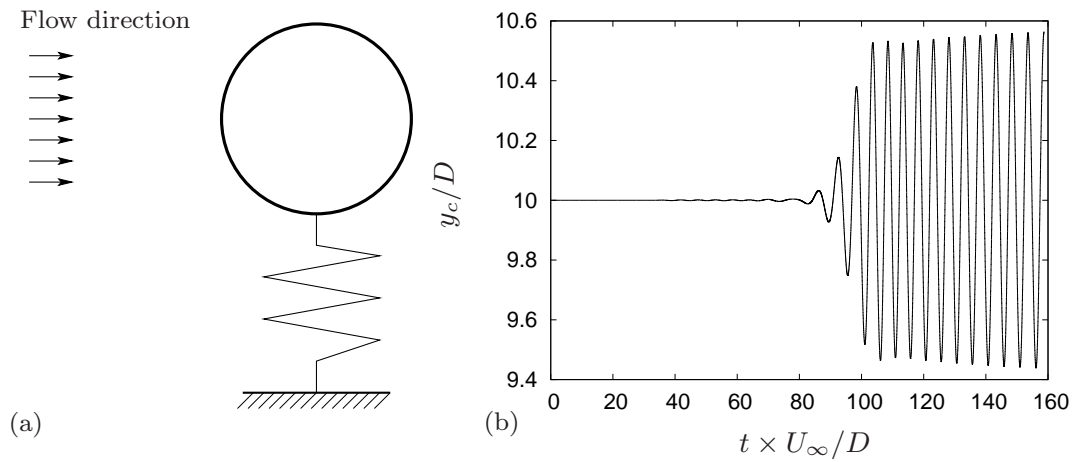


Figure 3.22.: (a) System description. (b) — Time history of the cylinder vertical position for the following paramters setting: $M_{red} = 2$, $U_{red} = 4$.

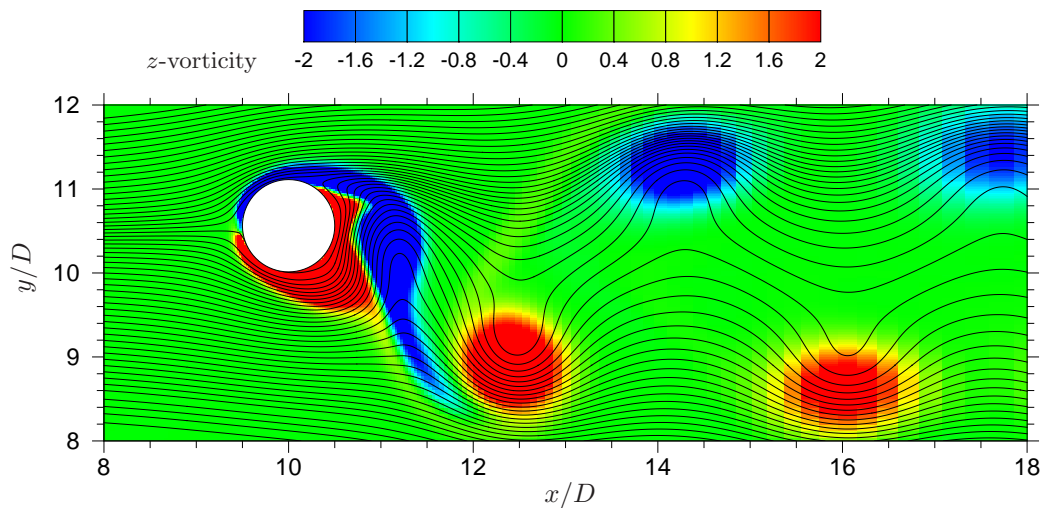


Figure 3.23.: Istantaneous z -vorticity countour in the vicinity of the cylinder and streamlines for the following paramters setting: $M_{red} = 2$, $U_{red} = 4$.

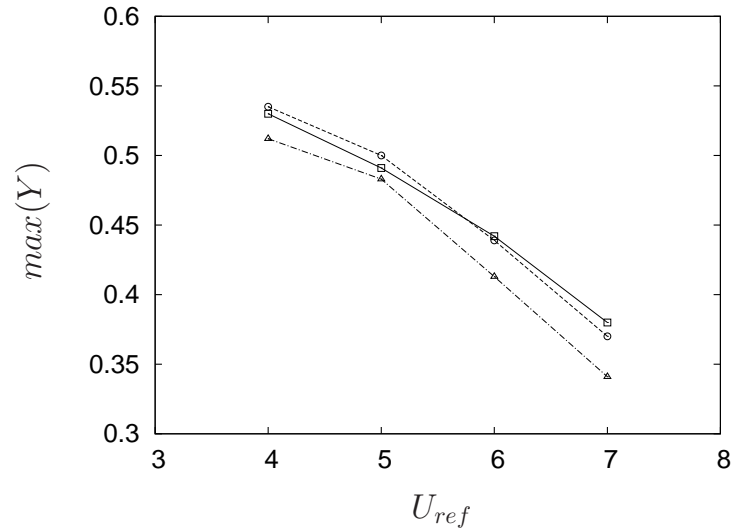


Figure 3.24.: Maximum amplitude variations for the CURVIB method of [Borazjani et al., 2008] (— \square) and for the immersed interface method (— \circ : $n = 50$, — \triangle : $n = 25$.)

3.4.4. Laminar boundary layer flow over a compression corner at $Ma = 6.06$

In this test case we consider a $Ma = 6.06$ laminar flow over a compression corner, according to an experimental investigation carried out by Lewis et al. [Lewis et al., 1968]. In such flow configuration the adverse pressure gradient generated by the shock leads to the separation of the boundary layer.

The Reynolds number based on freestream conditions and on the distance L_c between the model leading edge and the location of the corner is $Re_{L_c} = 1.5 \cdot 10^5$ and the compression corner angle is $\alpha_c = 10.25^\circ$. An adiabatic and an isothermal condition, with a temperature ratio $T_w/T_\infty = 1.7$, are considered for the surface of the experimental model.

The present experiment has been chosen for numerical computation since it allows us to test the immersed interface method in the compressible regime. The isothermal wall test case is also fundamental in order to validate the term X^{ht} of the interface interaction model.

The computational domain adopted for the computation extends from $x/L_c = 0.4$ to $x/L_c = 2.0$ in the streamwise direction and from $y/L_c = 0$ to $y/L_c = 0.6$ in the wall normal direction. Two grids were used for the computation, both characterized by a refinement towards the central region. Details about the grids are given in Table. 3.12. The same number of points within the incoming boundary layer thickness n_{δ_0} has been chosen for both, the adiabatic and the isothermal case, requiring a higher grid stretching factor in the isothermal case due the thinner incoming boundary layer.

Table 3.12.: Grid details for the hypersonic compression corner flow test case. Total number of cells N_p and cells for incoming boundary layer thickness n_{δ_0} .

Grid name	N_p	n_{δ_0}
level 1	~ 75000	20
level 2	~ 250000	40

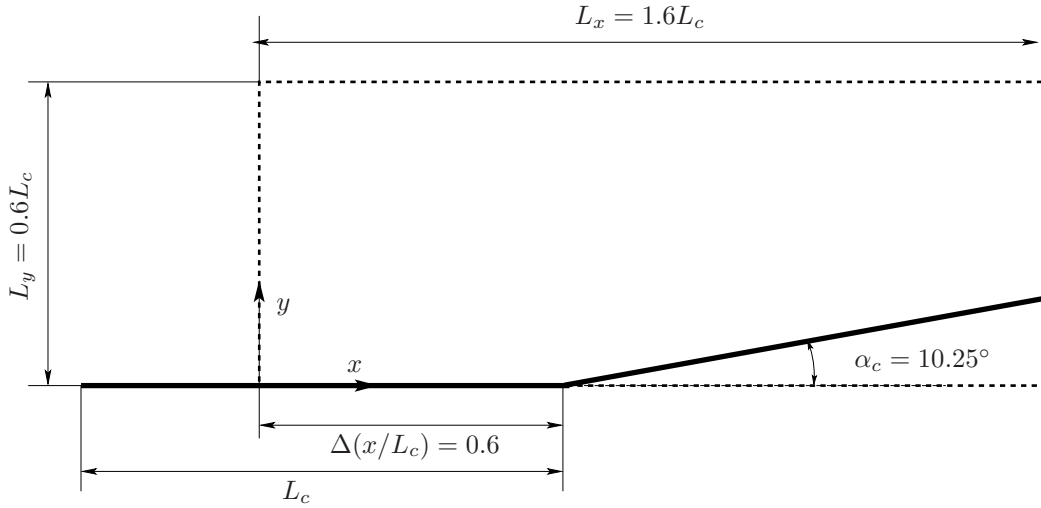


Figure 3.25.: Computational box for the laminar boundary layer over a compression corner.

At the inflow boundary the laminar similarity solution is prescribed. At the outflow and at the upper boundary a linear extrapolation boundary condition is used. The compression corner geometry is imposed by the immersed interface method.

Fig. 3.26 shows the contour plot of the pressure together with streamlines highlighting the extension of the recirculation region for the adiabatic wall case. Figs. 3.27 (a)-(b) show the comparison between experimental and numerical results for the wall pressure distribution along the wall. For both cases the lower resolution computation delivers a shorter recirculation region and underestimates the pressure in the core region. Furthermore, a certain oscillation of the pressure signal can be seen after the reattachment in the lower resolution computation. Such oscillations are mainly due to the coarsening of the grid in the downstream region of the compression corner. The higher resolution computation shows a good agreement with experimental data. Moreover, the higher resolution computation does not exhibit any oscillation of the pressure signal in the downstream region.

3.4.5. Laminar cavity flow at $Ma = 8.9$

We consider a $Ma = 8.9$ laminar flow over a hollow body of revolution which contains a cavity. Geometrical details about the hollow test model used to carry out

3. Numerical approach validation

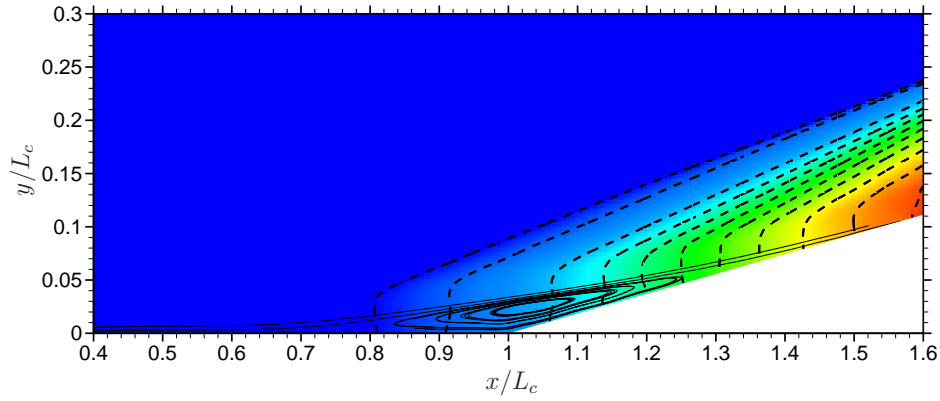


Figure 3.26.: Pressure contours and streamlines showing the recirculation region for the adiabatic wall case.

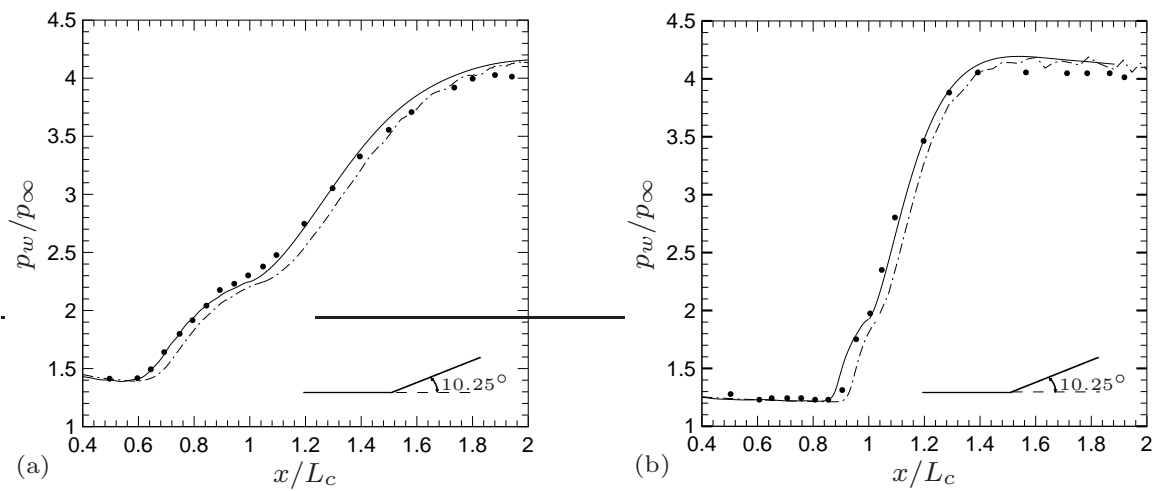


Figure 3.27.: Pressure distribution along the ramp surface. (a) Adiabatic wall case:
 • Experimental data [Lewis et al., 1968]; level 1 grid ---; level 2 grid — . (b) Isothermal wall case:
 • Experimental data [Lewis et al., 1968]; level 1 grid ---; level 2 grid — .

the experimental investigation that we adopted as reference for our computations can be derived from the work of Jackson et al. [Jackson et al., 2001]. Several cavity configurations are considered in the experimental and numerical analysis of Jackson et al. [Jackson et al., 2001]. For our validation purpose we focus only on the square cavity configuration. The Reynolds number based on the freestream conditions and on the cavity edge D is $Re_D = 238500$. The model surface is assumed to be isothermal with a temperature ratio $T_w/T_\infty = 4.93471$. The computational domain, shown in Fig. 3.28, extends from $x/D = -1.7$ to $x/D = 14$ in the x -direction and from $y/D = 0$ to $y/D = 4$ in the y -direction. Two different grids are used for the computation which are characterized by a different refinement level in the proximity of the hollow body surface. The coarse mesh (level 1) has minimum cell dimension in wall normal distance within the cavity region of $\Delta x_{min}/D = 0.0035$ and the fine mesh (level 2) is characterized by $\Delta x_{min}/D = 0.001$. A close up view of the level 2 grid in the cavity region is given in Fig. 3.29. At the inflow freestream values are imposed. At the streamwise outflow a linear extrapolation procedure is applied, while at the top a boundary condition based on riemann-invariants extrapolation is adopted. The model geometry is treated as an isothermal wall boundary and described through the immersed interface method.

An instantaneous snapshot of the computed Schlieren-type visualization (Fig. 3.4.5 a) reveals similarities with the experimental picture (Fig. 3.4.5 b). A shock wave originating from the leading edge of the model is clearly visible in both figures. Fig. 3.31 shows a comparison in terms of computed local Mach number profile for the fore-body boundary layer in a position located $0.4 \Delta x/D$ upstream of the cavity leading edge. Tab. 3.13 gives a comparison in terms of displacement and momentum thickness. A good agreement is found for both local and integral features of the boundary layer. A special focus is given to the flow inside the cavity. Fig. 3.32 shows the streamline pattern within this region obtained from the level 2 grid. The flow is characterized by a main central vortex with two secondary vortices located at the lower corners of the cavity. Another small secondary vortex is visible near the top of the front wall. This vortex system is in a good agreement with computational result shown in Fig. 12 of the work of Jackson et al. [Jackson et al., 2001]. A small difference can be found in the lower-right secondary vortex which extends less to the left side than the one from the reference.

A final comparison is shown in Fig. 3.33 (a)-(b) between numerical and experimental results concerning the surface pressure and heat transfer distribution for the cavity and parts of the fore-body and after-body. The abscissa s/D , represents a wetted distance along the body surface being zero at the top-rear corner of the cavity.

Table 3.13.: Computed laminar boundary layer data at $x/D = 7.6$.

	δ^*/D	θ/D
Numerical reference data [Jackson et al., 2001]	0.1052	0.00672
Present(level 1 grid)	0.1104	0.00693
Present(level 2 grid)	0.1075	0.00681

3. Numerical approach validation

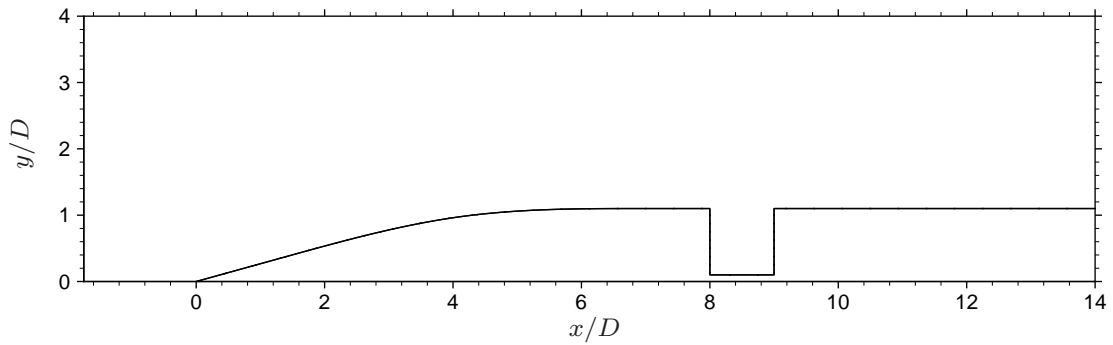


Figure 3.28.: Computational domain for the cavity and the region external to the body of revolution. The body of revolution is described by the zero levelset contour line.

More details about the calculation of the abscissa s/D can be found in the reference [Jackson et al., 2001]. A good agreement between experimental and numerical results is found for both quantities and a good mesh independence of the results is also clearly visible.

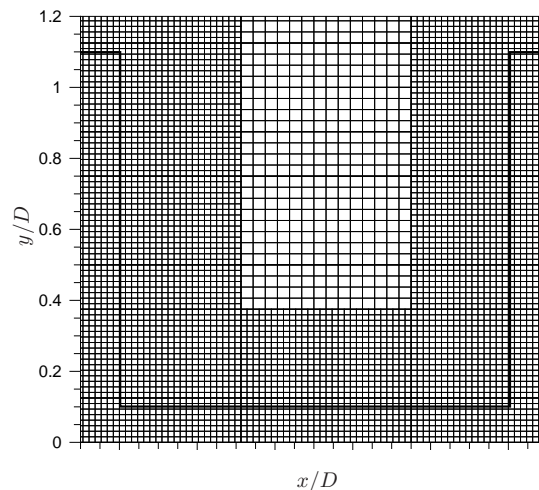


Figure 3.29.: Detail of the computational grid in the cavity region. Each 20th line is shown.

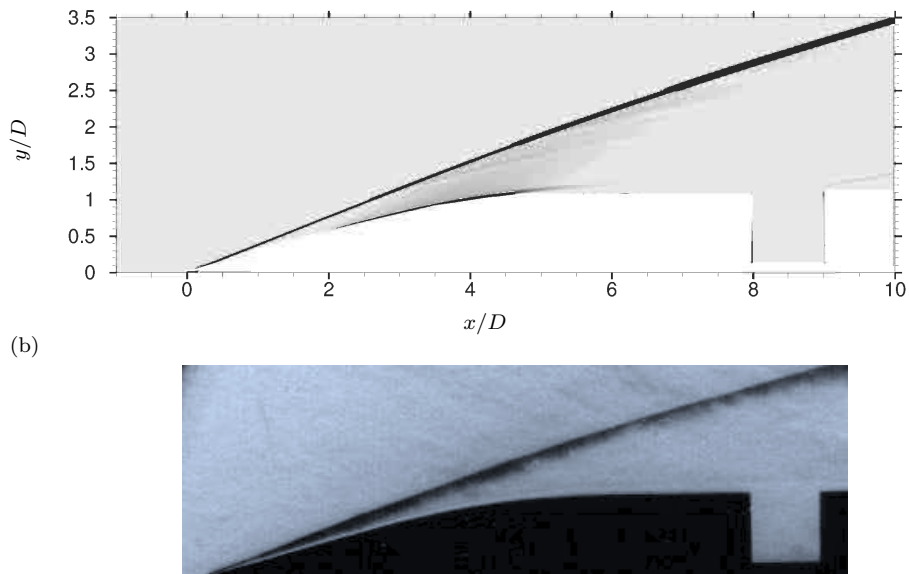


Figure 3.30.: Instantaneous representation of the flow by the Schlieren-type visualization. (a) The computed density gradient magnitude $\|\nabla\rho\|$ and (b) experimental Schlieren visualization [Jackson et al., 2001].

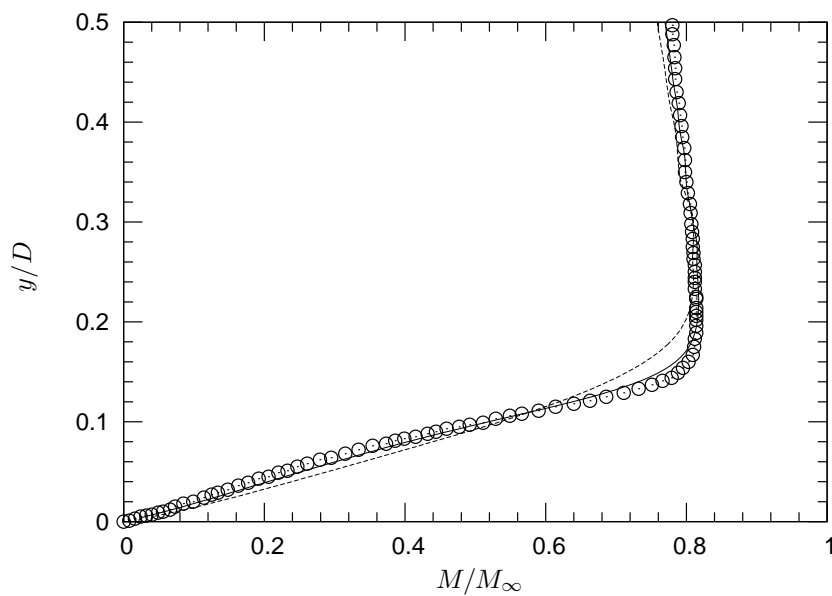


Figure 3.31.: Computed local Mach number profile at $x/D = 7.6$. ---- level 1 grid; — level 2 grid; ◦ numerical reference data [Jackson et al., 2001].

3. Numerical approach validation

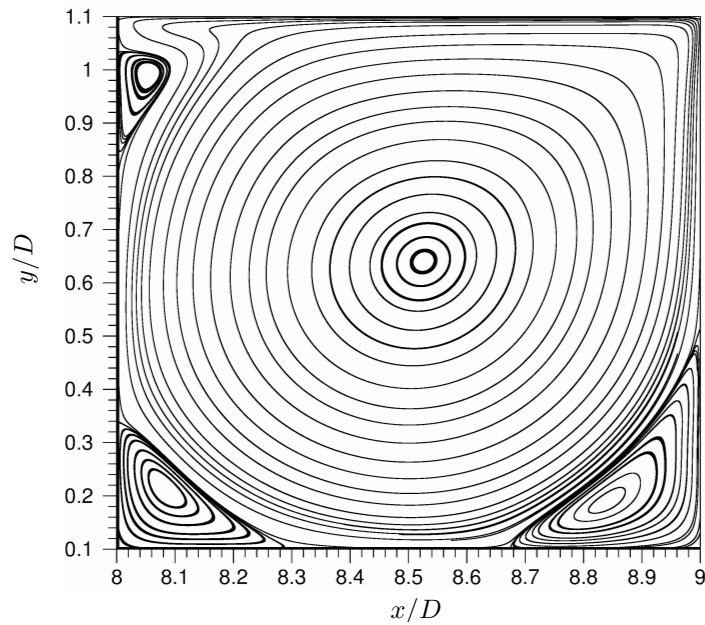


Figure 3.32.: Cavity streamlines pattern. The flow over the cavity is from left to right and the main cavity vortex has a clockwise circulation.

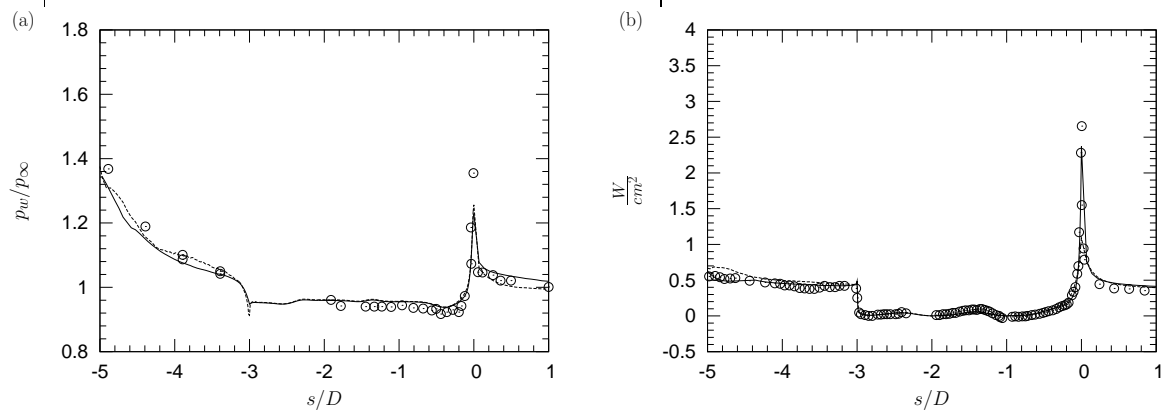


Figure 3.33.: (a) Surface pressure distribution. (b) Surface heat transfer distribution. ---- level 1 grid; — level 2 grid; \circ experimental reference data [Jackson et al., 2001].

4. Compression-Expansion corner flow

4.1. Flow configuration

Several experimental works [Zheltonodov and Yakovlev, 1986, Zheltonodov et al., 1990, Zheltonodov, 1991] were dedicated to the investigation of the essential flow phenomena taking place in compression-decompression ramp flows. A sketch of the main aspects of the flow is given in Fig. 4.1. The undisturbed incoming turbulent boundary layer is deflected at the compression corner. This causes the generation of a compression shock which penetrates the boundary layer with the penetration depth being dependent on the local Reynolds number. For sufficiently large deflection angles the adverse pressure gradient within the boundary layer results in a region of mean-flow separation near the corner. A detached shear layer travels above the separation region and reattaches in the inclined part of the compression ramp. A λ -shock system is generated near the separation region. The forward foot of the λ -shock originates from the region of flow separation, and the rearward foot from the region of flow reattachment. Further downstream, the reattached boundary layer reaches the decompression ramp and passes through the Prandtl-Meyer expansion. Even further downstream, the boundary layer relaxes again towards a developed zero-pressure-gradient boundary layer.

In Fig. 4.1 the separation and the reattachment positions are indicated by S and R , respectively. In the inset 1, the process of turbulence amplification by the interaction with a rapid compression within the boundary layer is depicted. Note also that the shock foot spreads out towards the wall due to reduced local Mach number and to turbulent diffusion, at the same time the shock foot location experiences a backward and forward motion in the streamwise direction (inset 2). After the reattachment at the deflected part of the compression ramp, a turbulent boundary layer is re-established. Experimental results support the existence of pairs of large counter-rotating streamwise vortices in the reattachment region as well as in the reverse flow of the separation zone (inset 3). Inset 4 shows the damping of turbulent fluctuations by the interaction with the Prandtl-Meyer expansion at the expansion corner. Fig. 4.2 gives a general overview on the flow field obtained from the large-eddy simulation. The temperature field shown on the left side clearly highlights the thickening of the boundary layer after the interaction and the shedding of structures after the decompression corner. Iso-surfaces of the Q -criterion are shown in the middle to show the turbulent structures in the near-wall region. Finally, a contour of the streamwise velocity fluctuations in the vicinity of the wall is given on the right side. This last view highlights the strong modification undergone by the turbulent

structures in the vicinity of the wall when interacting with the shock and with the centered-expansion.

4.2. Experimental setup

In the present work we compare our results with the experimental data from [Zhel-tovodov et al., 1990]. For the first time the whole compression-expansion ramp was taken into account. The experiments were performed using two models having the same shape but different linear scales. The larger model was used for a detailed investigation of the mean flow with a free-stream Mach number of $Ma_\infty = 2.88$ and a Reynolds number based on the incoming boundary layer thickness of $Re_{\delta_0} = 132840$. The turbulence characteristics are investigated using the small model with a free-stream Mach number of $Ma_\infty = 2.95$ and $Re_{\delta_0} = 63560$. A description of the test model used for the high Reynolds case is given in Fig. 4.3, together with its actual dimensions. The experimentally obtained flow field and the measurement stations are sketched in Fig. 4.4 for both configurations of the 25° compression-expansion ramp. In the present work, the conditions of the large model are chosen, but a comparison is also carried out with the turbulence data obtained from the small model by scaling them with the local boundary layer thickness. The present work aims at assessing the prediction quality of the employed numerical technique by directly matching the experimental parameters. Given the successful validation, the computational results provided a reliable numerical database for the analysis of different issues such as turbulence evolution and interaction with compression and rarefaction waves, features of near wall structures and characteristics of the shock-system unsteadiness.

4.3. Numerical setup

The computational domain, shown in Fig. 4.5, has the extents $L_x = 41.25 \delta_0$, $L_y = 12 \delta_0$ and $L_z = 4 \delta_0$. The computational grid, shown in Fig. 4.6, has been generated with an adaptive mesh refinement procedure which guarantees that the first point in the wall-normal direction at the inlet, with respect to the ramp geometry, is located at $y^+ \approx 2.2$. As a reference for possible comparison with other types of grids, a detailed description of the grid in the inflow boundary is given. The total number of points in wall normal direction in the inflow plane is 300. Six successive steps with a refinement factor of 2 are employed. 60 points are employed in the region $0. < y/\delta_0 < 0.25$. 60 points in the region between $0.25 < y/\delta_0 < 0.75$. 45 points in the region $0.75 < y/\delta_0 < 1.5$. 45 points in the region $1.5 < y/\delta_0 < 3.0$. 45 points in the region $3.0 < y/\delta_0 < 6.0$ and 45 points in the region $3.0 < y/\delta_0 < 12.0$. Such resolution was found to be enough to reproduce the experimental results in the first reference section E1 with sufficient accuracy. A total number of 32.5×10^6 grid points are used to discretize the computational domain. The grid spacing in the streamwise

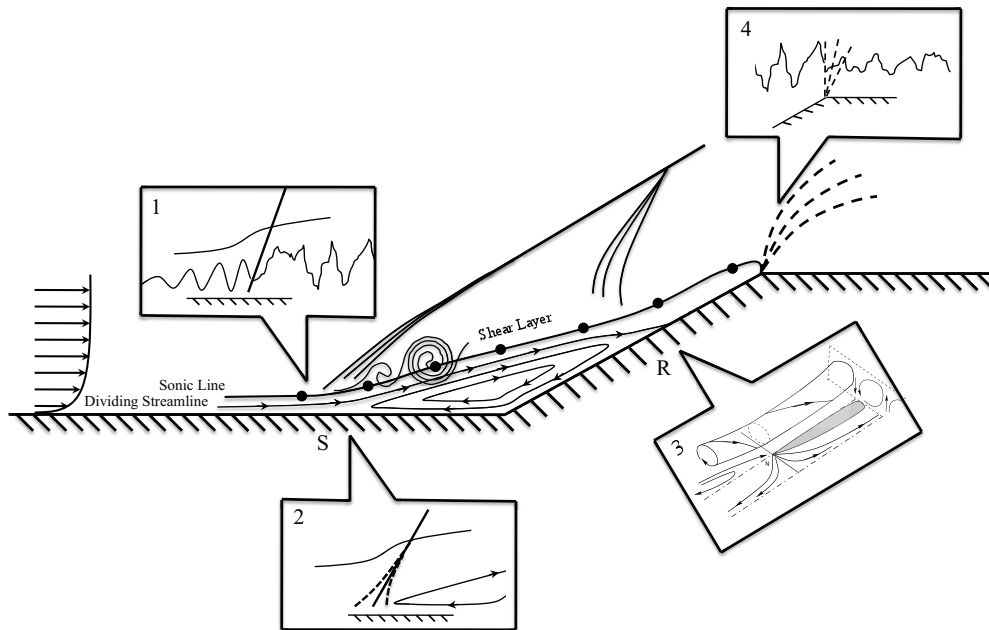


Figure 4.1.: Main flow phenomena of the compression-expansion ramp flow.

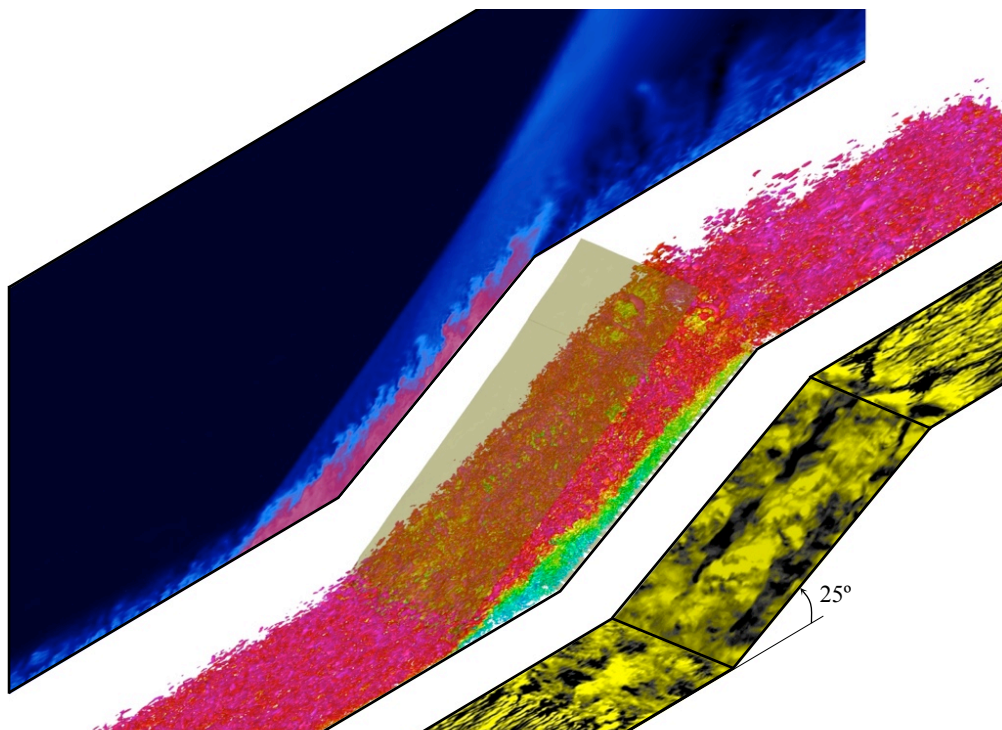


Figure 4.2.: Global view of the compression-expansion ramp flow. (left) Temperature field. (middle) turbulent structures visualized by means of Q-criterion isosurface, together with the shock visualized as pressure isosurface. (right) streamwise velocity fluctuations in the vicinity of the wall.

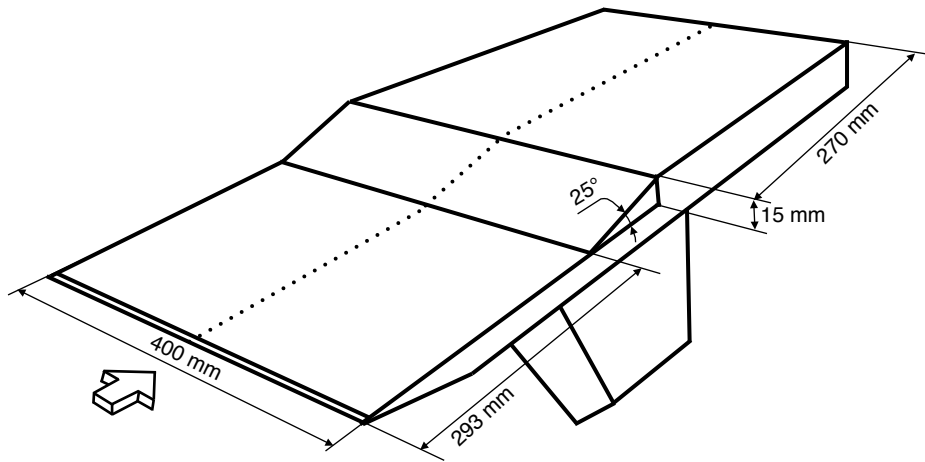


Figure 4.3.: Experimental test model.

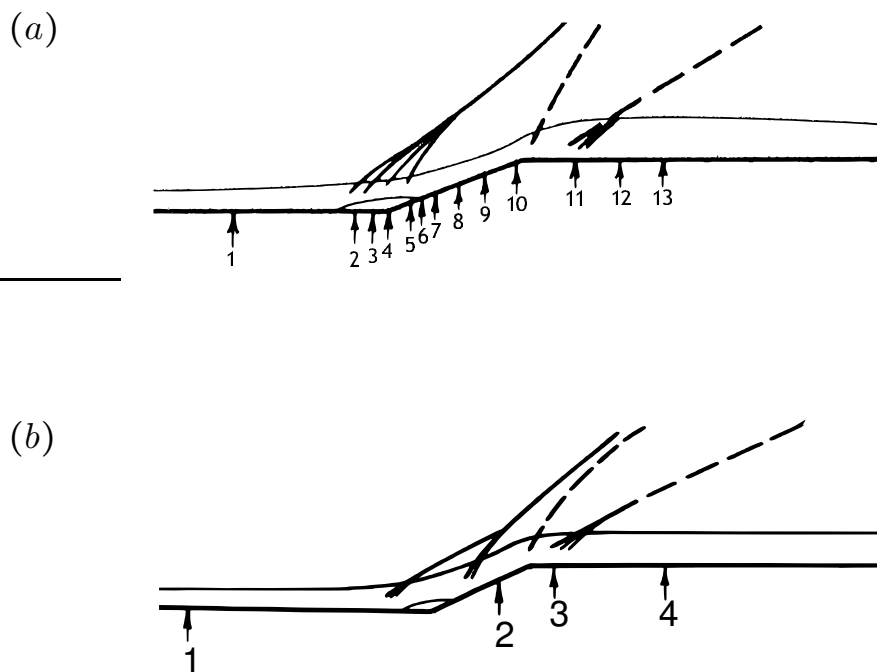


Figure 4.4.: Experimental measurement sections for the large (a) and small (b) model.

Table 4.1.: Streamwise location of the measurement stations.

Large Model		Small Model	
Station	x/δ_0	Station	x/δ_0
E1	-8.05	T1	-15.42
E2	-2.93	T2	4.41
E3	-1.95	T3	7.93
E4	-1.22	T4	14.98
E5	1.22		
E6	2.68		
E7	3.05		
E8	4.15		
E9	5.73		
E10	7.56		
E11	12.20		
E12	15.24		
E13	19.15		

direction is $\Delta x^+ \approx 52.9$ and in the spanwise direction a resolution of $\Delta z^+ \approx 25.7$ is adopted.

4.4. Incoming supersonic turbulent boundary layer

The correct description of the features of the incoming turbulent boundary layer plays a key role in the downstream evolution of the flow. The extent of the separation zone, for example, depends directly on the level of turbulence in the incoming boundary layer. Based on this evidence a first flat-plate boundary-layer simulation is carried out in order to estimate the transition length needed by the flow to recover the modeling errors introduced by the digital filter procedure adopted in the inflow boundary. For this simulation the domain is rectangular with a streamwise extent $L_x = 20$, a wall normal extent of $L_y = 4$ and a spanwise extent equal to the one adopted in the compression-expansion ramp configuration of $L_z = 4.0$. In this case the grid has been generated with an adaptive mesh refinement procedure which guarantees the same resolution as the one achieved in the full configuration ($\Delta x^+ = 52.9, y_{min}^+ = 2.2, \Delta z^+ = 25.7$). The prescribed mean turbulent boundary layer profile and turbulence intensities for the digital filter procedure were obtained from an earlier temporal simulation under the same flow conditions. After a start up transient of about $100 \delta_0/U_\infty$ time units, the simulation was continued for about $150 \delta_0/U_\infty$ gathering statistics with a sampling interval of $0.02 \delta_0/U_\infty$. The streamwise station located at $x = 11.95$ showed the best agreement with the reference experimental station E1. A detailed comparison of mean-flow characteristics between experiment and computation in the reference section E1 is shown in Table 4.2. The comparison is

4. Compression-Expansion corner flow

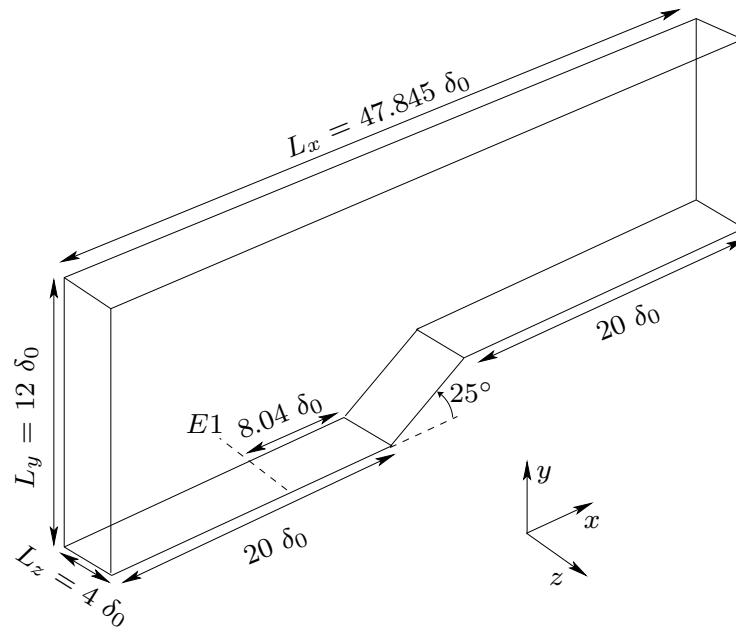


Figure 4.5.: Computational domain of the present LES.

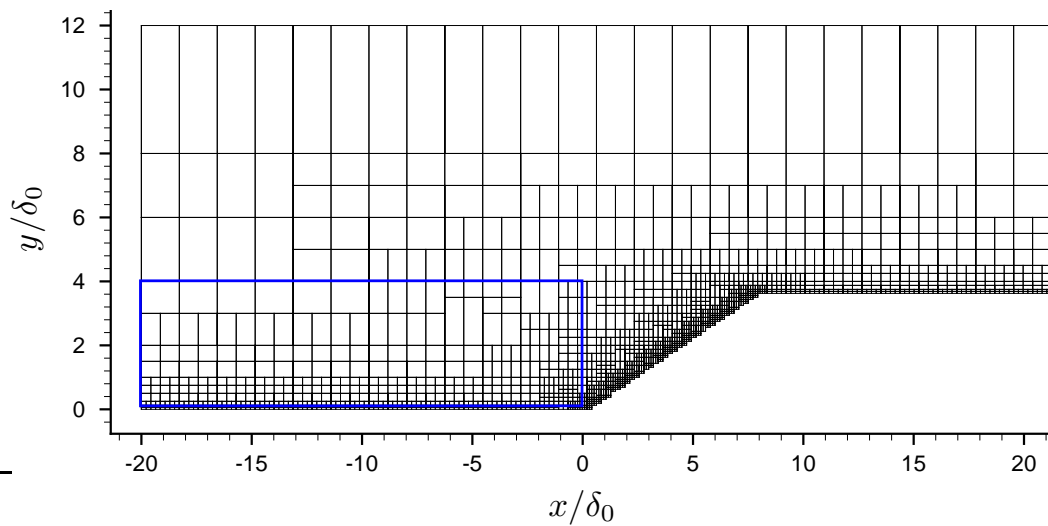


Figure 4.6.: Computational grid of the present LES (not every line is shown).
— Sub-domain adopted for the incoming turbulent boundary layer computation.

Table 4.2.: Summary of mean-flow parameters for the flat-plate boundary layer simulation.

	δ_0	δ_1	δ_2	H_{12}	Re_{δ_0}	Re_{δ_2}	$C_f \cdot 10^3$
Experiment	1.0	0.349	0.073	4.78	132840	4924	1.47
Computation	1.0	0.314	0.079	3.97	132846	5385	1.41

carried out in terms of displacement and momentum thickness δ_1 and δ_2 , Reynolds number based on free-stream velocity, momentum thickness and viscosity at the wall, Re_{δ_2} and shape factor, H_{12} . The agreement of the mentioned quantities between computation and experiment is good. Fig. 4.7(a) shows the skin-friction evolution obtained for the digital filter. The technique produces a transient of about 8 reference lengths. The wall-normal distribution of mean Mach number, temperature, velocity, and density are compared with the experimental data in Fig. 4.7(b). In the bulk, the computed velocity profile agrees well with the experimental data, and minor discrepancies can be observed for the density and temperature profiles. Fig. 4.8 shows the autocorrelation coefficients in the spanwise direction $R_{\alpha\alpha}(z/\delta_0)/R_{\alpha\alpha}(0)$ for the considered grid in the position $x/\delta_0 = 11.95$ and local $y^+ = 150$. The figure shows that the correlations for the velocity components and density decay towards zero thus ensuring that the computational domain in the spanwise direction is sufficiently wide not to inhibit the turbulence dynamics. The Van-Driest-transformed velocity profiles are shown in Fig 4.9(a) for both experimental and numerical results. Both profiles agree well with the logarithmic law of the wall $U_{VD}^+ = \log(y^+)/0.4 + 5.25$. A certain deviation from the logarithmic behavior is visible for the first two experimental values. Turbulence statistics at the same streamwise station are shown in Fig. 4.9(b). In order to compare our results with DNS data of an incompressible turbulent boundary layer by [Spalart, 1988], we adopted the compressibility correction by [Huang et al., 1995]. To further proof the validity of the results, a set of experimental values of C_f versus Re_{δ_2} taken from [Fernholz and Finley, 1977, Fernholz and Finley, 1981], together with the Kármán-Schönerr friction coefficient prediction law and our computed value, are shown in Fig. 4.4. The computed C_f lies below the value predicted by the empirical correlation but is well within the uncertainty range of the experimental measurements.

4.5. Time-averaged flow characteristics

4.5.1. Wall pressure and skin-friction coefficient

The mean wall pressure, normalized by its mean value at the station $E1$, constantly increases during the shockwave/boundary layer interaction with a plateau inside the separation zone. It later drops to the initial values after interacting with the expansion fan (Fig. 4.11(a)). The mean skin-friction exhibits the typical behavior for a

4. Compression-Expansion corner flow

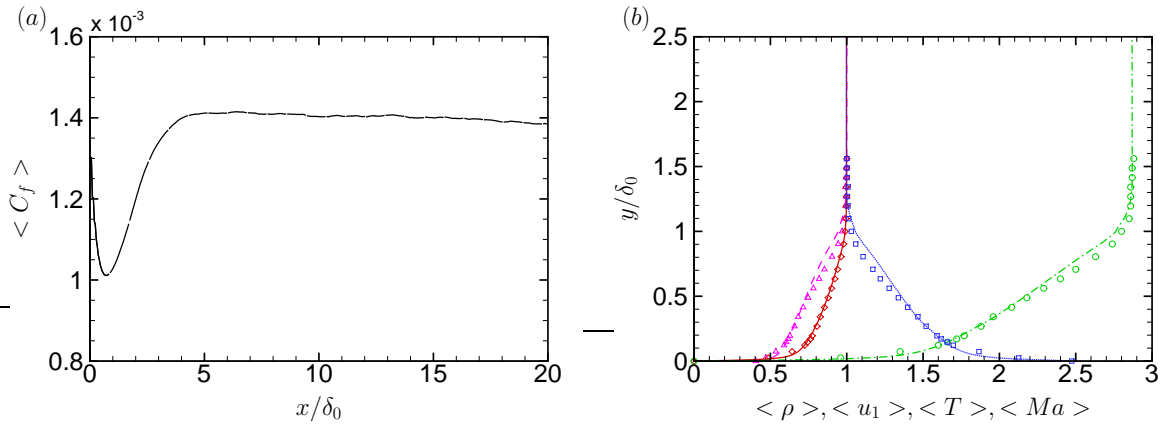


Figure 4.7.: (a) Friction coefficient evolution in the streamwise direction — . $E1$ section location ---- . (b) Wall normal distribution of the mean flow for the incoming boundary layer at the station E1. Mach number (LES -.-.- , experiment \circ); temperature (LES , experiment \square); velocity (LES — , experiment \diamond); density (LES -.-.- , experiment \triangle).

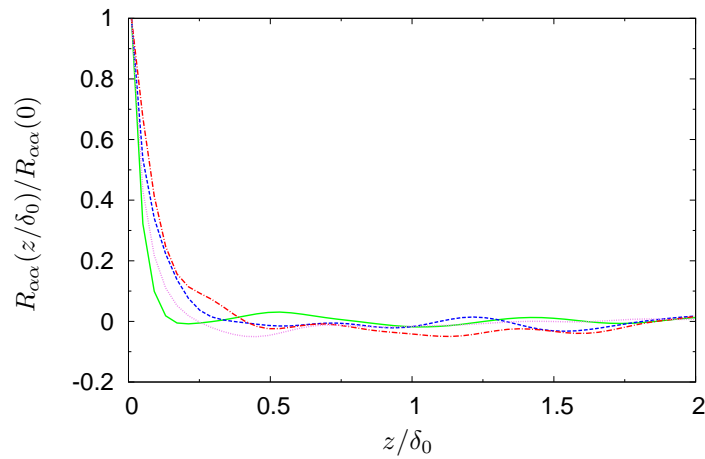


Figure 4.8.: Distribution of the two-point correlations in the spanwise direction at $x/\delta_0 = 11.95$ and $y^+ \approx 150$. — $\alpha = u_1$; - - - $\alpha = u_2$; - . - $\alpha = u_3$; . . . $\alpha = \rho$.

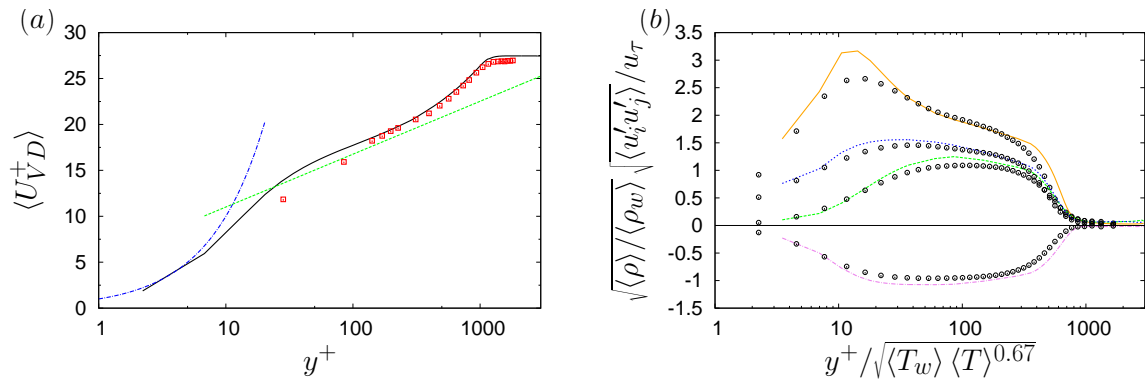


Figure 4.9.: (a) Van-Driest transformed mean-velocity profile at the station $E1$. \square , experimental (computed using the skin-friction coefficient C_f measured in the experiment). —, LES. - - -, linear law. ····, log-law $\log(y^+)/0.4+5.25$. (b) Turbulence statistics at the station $E1$. Lines denote LES data shown in inner-layer scaling using the compressibility correction of [Huang et al., 1995] and symbols represent DNS data of [Spalart, 1988]. — $\langle u'_1 u'_1 \rangle$; — $\langle u'_2 u'_2 \rangle$; — $\langle u'_3 u'_3 \rangle$; — $\langle u'_1 u'_2 \rangle$.

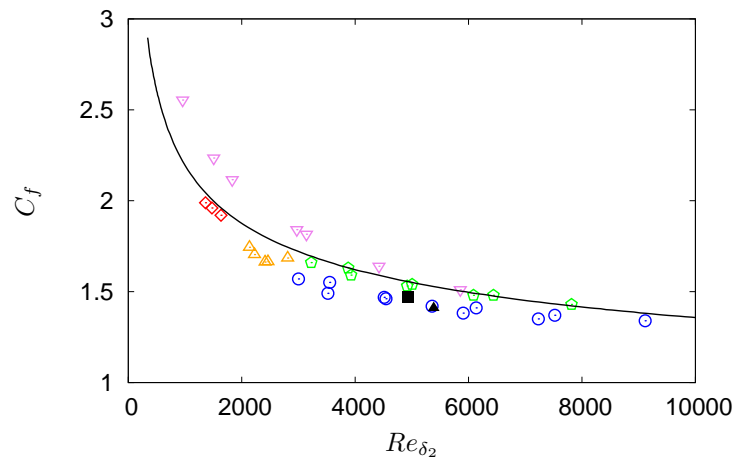


Figure 4.10.: Friction coefficient dependence on Re_{δ_2} . \blacktriangle , LES. \blacksquare , experiment. \blacktriangledown , Stal-mach CAT5802 ($M_\infty = 2.75$). \blacklozenge , Laderman & Demetriades CAT7702 ($M_\infty = 3.0$). \blacktriangle , Maier CAT7003 ($M_\infty = 2.9$). \blacklozenge , Mabey et al. CAT7402 ($M_\infty = 2.8$). \circ , Mabey et al. CAT7402 ($M_\infty = 3.0$). — Kármán-Schönerr $C_f - Re_{\delta_2}$ correlation.

separated flow (Fig. 4.11(b)). The initial decrease at $x/\delta_0 = -20$, is due to the synthetic turbulence technique adopted for the generation of the inflow data. A transient of about $5\delta_0$ is needed for the flow to recover then the modeling errors introduced by the digital filter procedure. A slight decrease along the flat plate is then visible, since the incoming boundary layer grows and the local Reynolds number increases ($x/\delta_0 < -6$). The friction coefficient drops, and near the separation point S assumes negative values inside the reverse flow region ($-4.5 < x/\delta_0 < 2.0$). It rises again after the reattachment point R to values which are slightly above the incoming ones on the upper surface. The spikes near the compression and the decompression corners are related to limited resolution of the corner singularity, where steep gradients of flow variables occur over a short distance.

4.5.2. Comparison of mean velocity profiles

Figure 4.12 gives a description of the mean flow evolution in terms of the mean streamwise velocity component. The colored dashed lines represent minimum and maximum values in the spanwise direction for each station. The velocity considered for the comparison in the stations $E5$ to $E10$ has been computed by projecting the local velocity in parallel direction to the deflected part of the ramp. The undisturbed incoming turbulent boundary-layer profile in section $E1$ evolves into a profile with weak reverse flow slightly downstream of the separation point (section $E2$). Further downstream, the reverse flow becomes stronger (sections $E3 - E5$). At section $E6$ the boundary layer re-attaches while still showing a momentum deficit in the wake. This re-established attached boundary layer develops towards an undisturbed profile further downstream (sections $E7 - E10$). After the expansion fan the boundary layer becomes thicker and recovers similar features to the undisturbed incoming condition (sections $E11 - E13$). Taking into account the spanwise variation of the computed mean velocity, experimental and numerical data generally agree well. In section $E5$ the computation predicts lower values of negative velocity with respect to the experimental data. Such discrepancy is evident also in the data of [Loginov et al., 2006] and can be explained by accounting for difficulties in measuring the reverse flow and also taking under consideration that the accuracy and the reliability of experimental data are reduced near the location of the zero velocity. With respect to the data of [Loginov et al., 2006] a better prediction is achieved for the section $E2$. Our computation clearly shows a region of incipient separation and a better agreement in the region inside the boundary layer. In section $E8$, a clear disagreement is visible in the outer region. This region of the flow is coincident with the position of the second stem of the λ -shock system which exhibits a highly unsteady character. It is known that the accuracy of the static pressure measurements is reduced in regions characterized by unsteady shocks.

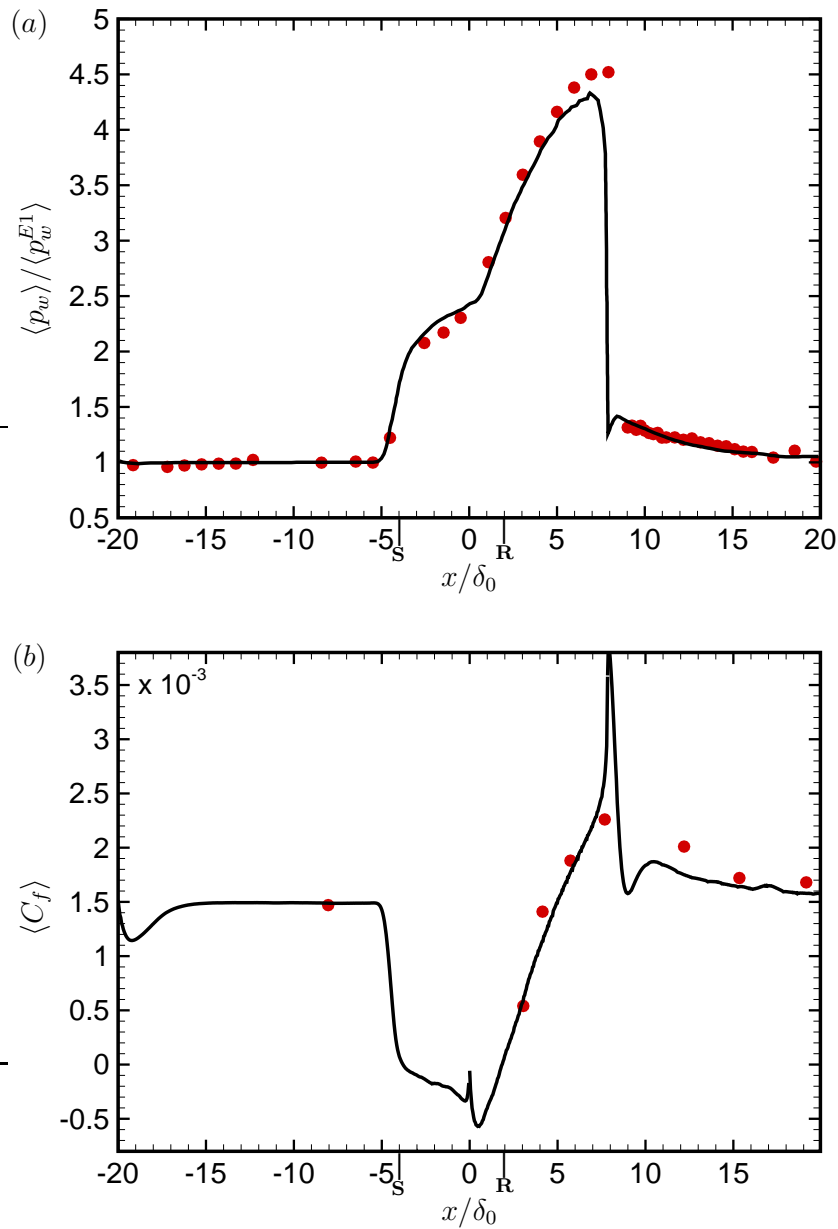


Figure 4.11.: (a) Averaged wall-pressure and (b) skin-friction coefficient distributions in the streamwise direction. \circ , reference experiment; — current LES averaged in time and over the spanwise direction. Symbols S and R indicate the mean separation and reattachment points.

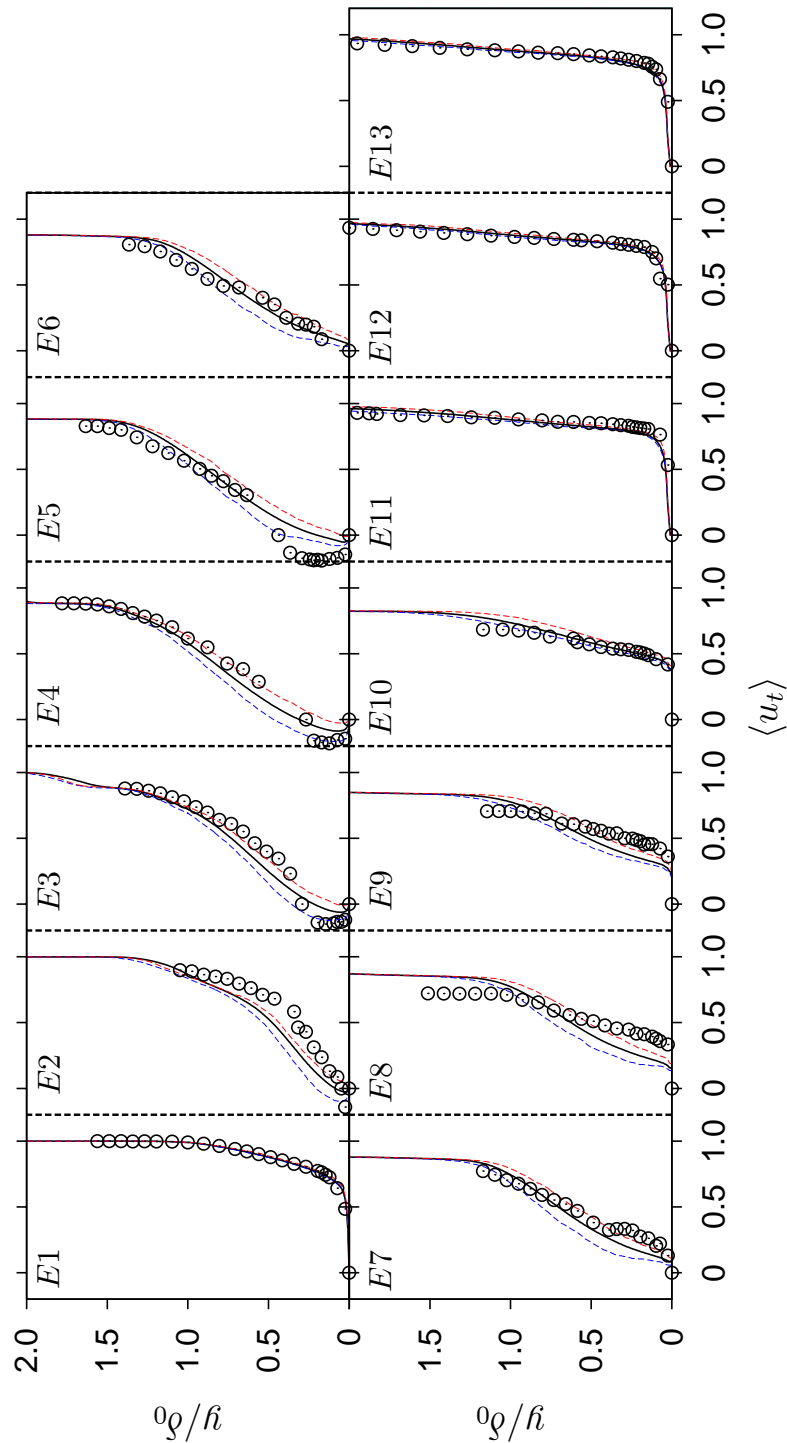


Figure 4.12.: Velocity profiles at stations E1-E13. \circ , reference experiment; —, current LES averaged in time and over the spanwise direction. - - - Maximum values along the spanwise direction. - - - Minimum values along the spanwise direction.

4.5.3. RMS profiles comparison

A comparison of the root-mean-square (RMS) values of velocity $\sqrt{\langle u'u' \rangle}$ and density $\sqrt{\langle \rho'\rho' \rangle}$ fluctuations is shown at the downstream stations $T1 - T4$ in Fig. 4.13. The data refer to the lower Reynolds number experiment carried out on the small model, as mentioned in Sec. 4.1. The locations of the measurement sections $T1 - T4$ are shown in Tab. 4.1. The measurement technique allowed only to record relative changes of the RMS values where data of the undisturbed boundary layer serve as reference. In this work we tried to mimic the experimental procedure of [Zhel-tovodov and Yakovlev, 1986] by normalizing the computational data with the respective maxima in section $T1$. Since the first section $T1$ is located outside of the computational domain, its values are compared to turbulence data extracted from section $E1$, which refers to an undisturbed zero pressure gradient turbulent boundary layer. In the first section the near-wall maxima of the velocity RMS distributions is not captured by the experiment due to the lack of near-wall resolution. In section $T2$ we can see that the interaction with the shock causes an amplification of density fluctuations by a factor of about 3, which agrees well with previous numerical observation [Adams, 2000, Loginov et al., 2006]. For what concerns the velocity fluctuations in the same location, a higher amplification factor is predicted by the computation with respect to the provided experimental values. In section $T3$ discrepancies in the location of the maxima for both the velocity and density fluctuations are visible. Such differences are due to the different flow topology since the experimental measurements were conducted on a model that was scaled with respect to the one considered in the simulation. In the last section $T4$ the agreement for the velocity fluctuations is quite good but also in this case the near wall maxima could not be captured by the experiment. For the density fluctuations same discrepancies due to flow topology could be detected.

4.5.4. Görtler-like vortices

Despite the flow geometry being two-dimensional, the interaction between the boundary layer and the shock breaks spanwise homogeneity. Fig. 4.14 shows a snapshot of the streamwise velocity fluctuations field in a plane parallel to the compression-expansion ramp wall at $y^+ \approx 12$. The colourmap is set in order to highlight the region of the flow with a velocity excess. On the left side of the domain we can see the typical streaky structures of a turbulent boundary layer. Such structures are then destroyed by the interaction with the shock. After the boundary layer reattachment location, a pattern which is related to two streamwise evolving structures is clearly visible. Such structures are indicators of the presence of a pair of counter-rotating streamwise vortices, often called Görtler-like vortices. This pattern extends along the entire deflected part of the ramp and disappears after the passage through the decompression corner. A zig-zag pattern is visible after the second corner which is caused by the passage of these vortical structures through the plane considered for the analysis. Afterwards the typical streaky structures of the incoming undisturbed

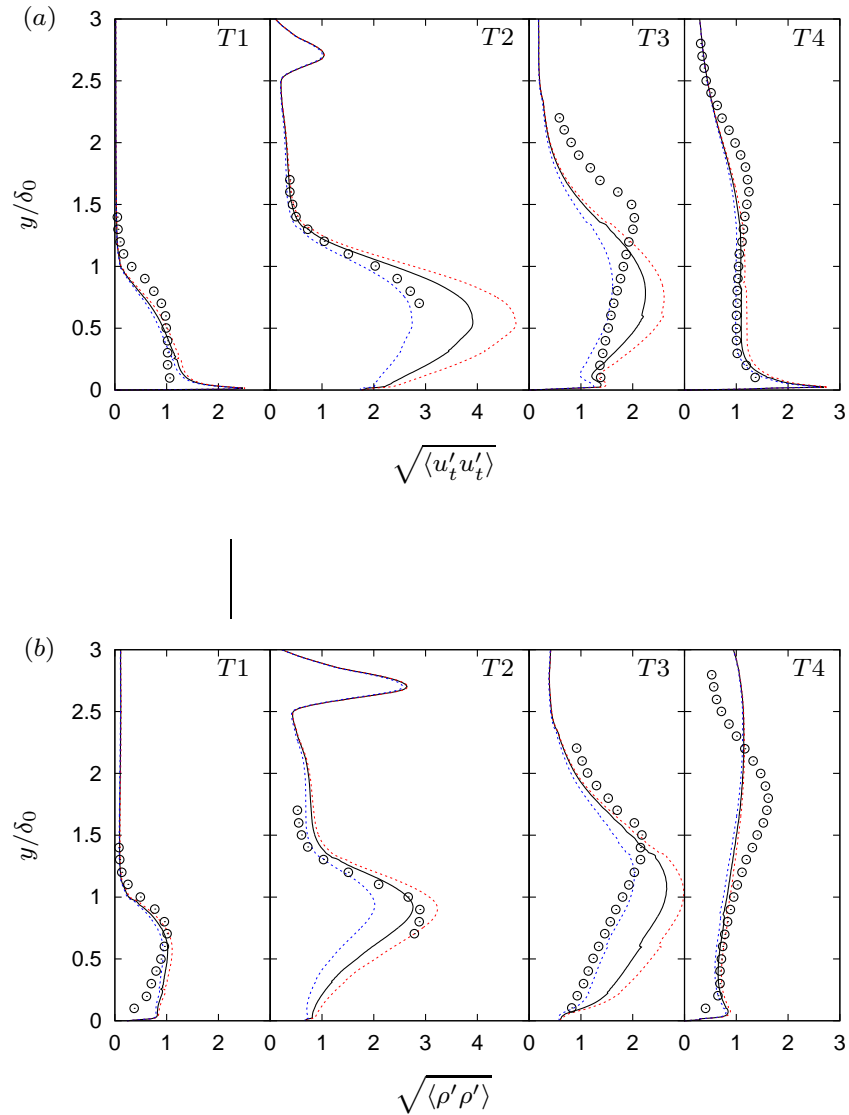


Figure 4.13.: Root-mean-square profiles of the velocity (a) and density (b) fluctuations at stations T1-T4. \circ , reference experiment; —, current LES averaged in time and over spanwise direction. - - - Maximum values along the spanwise direction. - - - Minimum values along the spanwise direction.

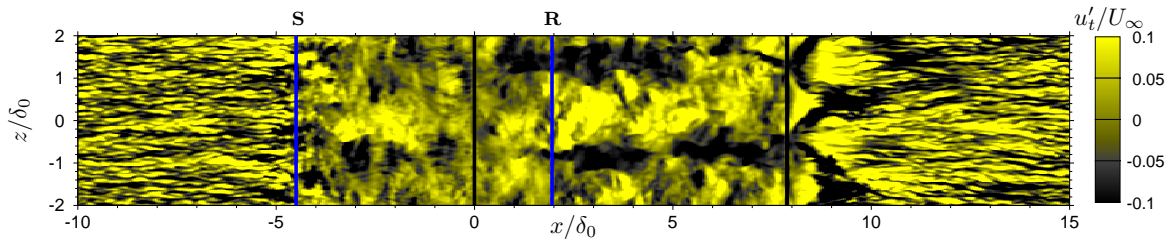


Figure 4.14.: Instantaneous snapshot of u'_t/U_∞ at $y^+ \approx 12$. Symbols **S** and **R** indicate the mean separation and reattachment points.

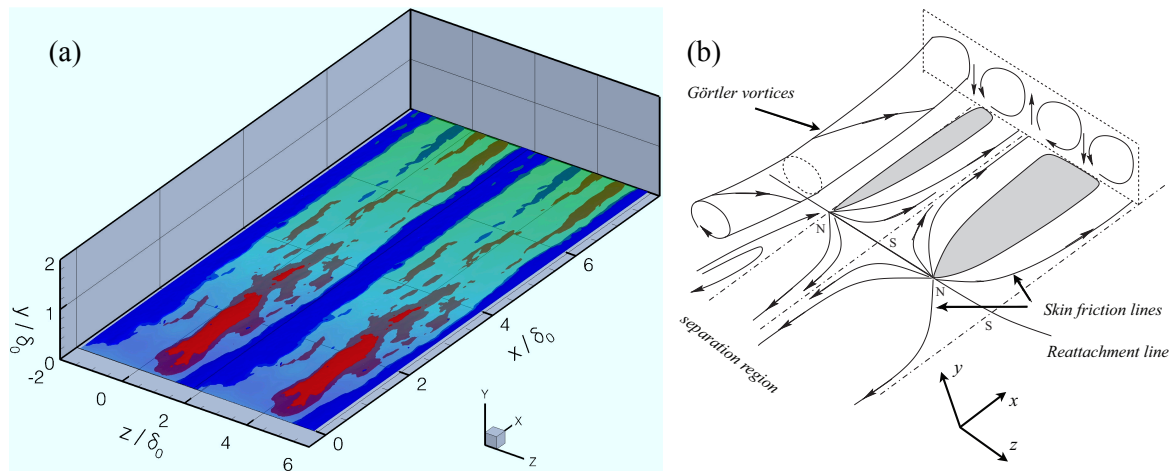


Figure 4.15.: (a) Isosurface of streamwise vorticity. The clockwise rotation is represented by the blue color. Anti-clockwise rotation is given in the red color. (b) Sketch of the main features characterizing the Görtler vortices.

boundary layer are recovered.

Further evidence of the presence of a pair of streamwise vortices is given by considering Fig. 4.15(a) which shows isosurfaces of the time averaged vorticity component in the direction parallel to the deflected part of the compression ramp. Since the circulation of these vortices is rather small, it is quite difficult to extract them from the background turbulence. Based on this consideration, the vorticity filtered by interpolation on an equidistant grid for the purpose of visualization. Positive rotation is indicated in red and negative rotation in blue. In order to highlight the clockwise vortex evolving along the streamwise direction, the periodic computational box has been duplicated in the spanwise direction.

The presence of these streamwise vortices significantly affects the properties of the mean flow and turbulence structure [Lüdeke et al., 2004, Floryan, 1991, Inger, 1977, Zheltovodov and Yakovlev, 1986, Loginov et al., 2006]. Considering the previous Figures 4.12 and 4.13, an increase of the spanwise variation is clearly visible in the region where the Görtler vortices are detected. Such a variation has to be taken into account when performing a comparison with the experimental values

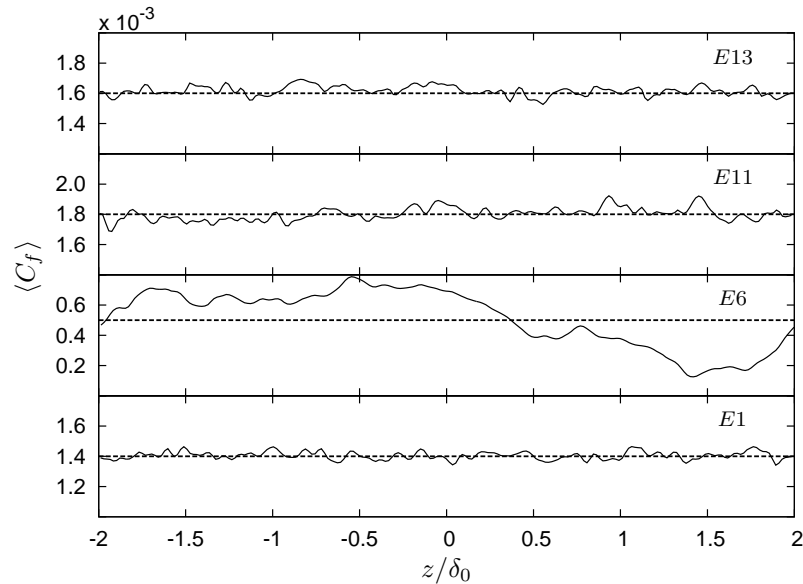


Figure 4.16.: Distribution of the mean skin-friction coefficient at the wall in the spanwise direction. — , averaged in time; ---- , averaged in time and over spanwise direction.

which refer to measurements taken along the symmetry plane of the model. The spanwise inhomogeneity of the mean C_f , caused by Görtler-like vortices is shown in Fig. 4.16. The amplitude of the variation increases from $\pm 0.06 \times 10^3$ in the undisturbed boundary layer at the station $E1$ to $\pm 0.3 \times 10^3$ in the section $E6$ just after the reattachment. After the decompression corner the amplitude of the variation becomes less pronounced, decreasing from $\pm 0.3 \times 10^3$ to $\pm 0.1 \times 10^3$ at station $E11$. The distribution becomes more uniform without extrema suggesting that the streamwise vortices decay while passing through the expansion fan. The isosurfaces of vorticity are also supporting this conclusion. Further downstream at station $E13$ the variation reduces almost to the undisturbed value of $\pm 0.08 \times 10^3$. Generally, the evolution of the streamwise vortices further downstream is an open question. For a compression corner at hypersonic speeds at $Ma_\infty = 6$ they extend only for a short distance downstream of the concave region [Simeonides, 1993].

The effects of the presence of the Görtler-like vortices are clearly evident when we consider Fig. 4.17(a), which shows the surface-streamline pattern in the vicinity of the reattachment region. Such a figure is a computational analogue of the experimental oil-flow visualization, shown in Fig. 4.17(b), obtained from the experiments of [Zhel'tovodov and Yakovlev, 1986]. In Fig. 4.17(a) a solid line represents the reattachment line given by the contour of $\langle C_f \rangle = 0$, which features a significant variation

in the spanwise direction. The pattern of distinct saddle and node points located along the reattachment line is seen in both the numerical and experimental figures. In accordance with what is shown in the sketch given in Fig. 4.15 (b), streamwise oriented convergence and divergence lines develop, respectively, from the saddle and node points not only downstream (after the reattachment) but also upstream (into the reverse flow in the separation zone). The position of the convergence lines is approximately $z/\delta_0 \approx -1.0$ and $z/\delta_0 \approx 1.0$, and the position of the divergence lines is approximately $z/\delta_0 \approx 0$ and $z/\delta_0 \approx 2.0$. The convergence lines can be related to cross-flow uplift and the divergence lines to cross-flow downwash, so that they represent footprints of two-pairs of counter-rotating streamwise vortices. In agreement with previous experimental and numerical observations [Floryan, 1991, Loginov et al., 2006] the spanwise width of each vortex pair is about $2\delta_0$. As in the case of [Loginov et al., 2006] the computational domain size in the spanwise direction is $4\delta_0$ with periodic boundary conditions applied in the homogeneous direction. Such an approach allows for capturing flow structures with spanwise periodicity of $4\delta_0$ at most. Therefore, it is not possible to exclude the existence of structures with larger spanwise periodicity, although there is no experimental evidence for such structures.

4.5.5. Turbulence evolution

The interaction of turbulence with a shock wave results in a decrease of turbulence length scales and an increase in turbulent fluctuations [Larsson and Lele, 2009, Ardonneau et al., 1979, Adams, 2000]. The interaction of turbulence with a Prandtl-Meyer expansion, on the other hand, results in a decrease of the turbulent fluctuations. For the considered compression ramp, the process of turbulence amplification through the compression shock and turbulence damping through the expansion fan is visualized in Figs. 4.18(a) and 4.18(b), where we show profiles of the RMS values of the fluctuating velocity $\sqrt{\langle u'_i u'_i \rangle}$ and density $\sqrt{\langle \rho' \rho' \rangle}$ at the same locations that were considered for the comparison of the mean velocity profiles. The velocity fluctuations for the stations $E5$ to $E10$ have been projected on the ramp parallel directions, as done before for the mean velocity profiles. All quantities are normalized with the incoming free-stream quantities. Thick solid lines denote the time- and spanwise-averaged values, while dashed lines refer to the spanwise minimum and maximum values. Concerning the velocity fluctuations, we observe the typical distribution for an equilibrium turbulent boundary layer at the location $E1$ with the characteristic peak located in the near wall region. As we move behind the shock interaction at position $E2$, the peak moves away from the wall towards the shear-layer. From position $E3$ onwards, a secondary peak is visible, which reflects the unsteadiness of the oblique shockwave. The same qualitative distribution is maintained up to section $E10$.

For section $E11$, which is located after the decompression corner, a profile similar to the one of the incoming undisturbed boundary layer is recovered with a slightly higher level of turbulence in the outer part. This enhanced turbulent content in the

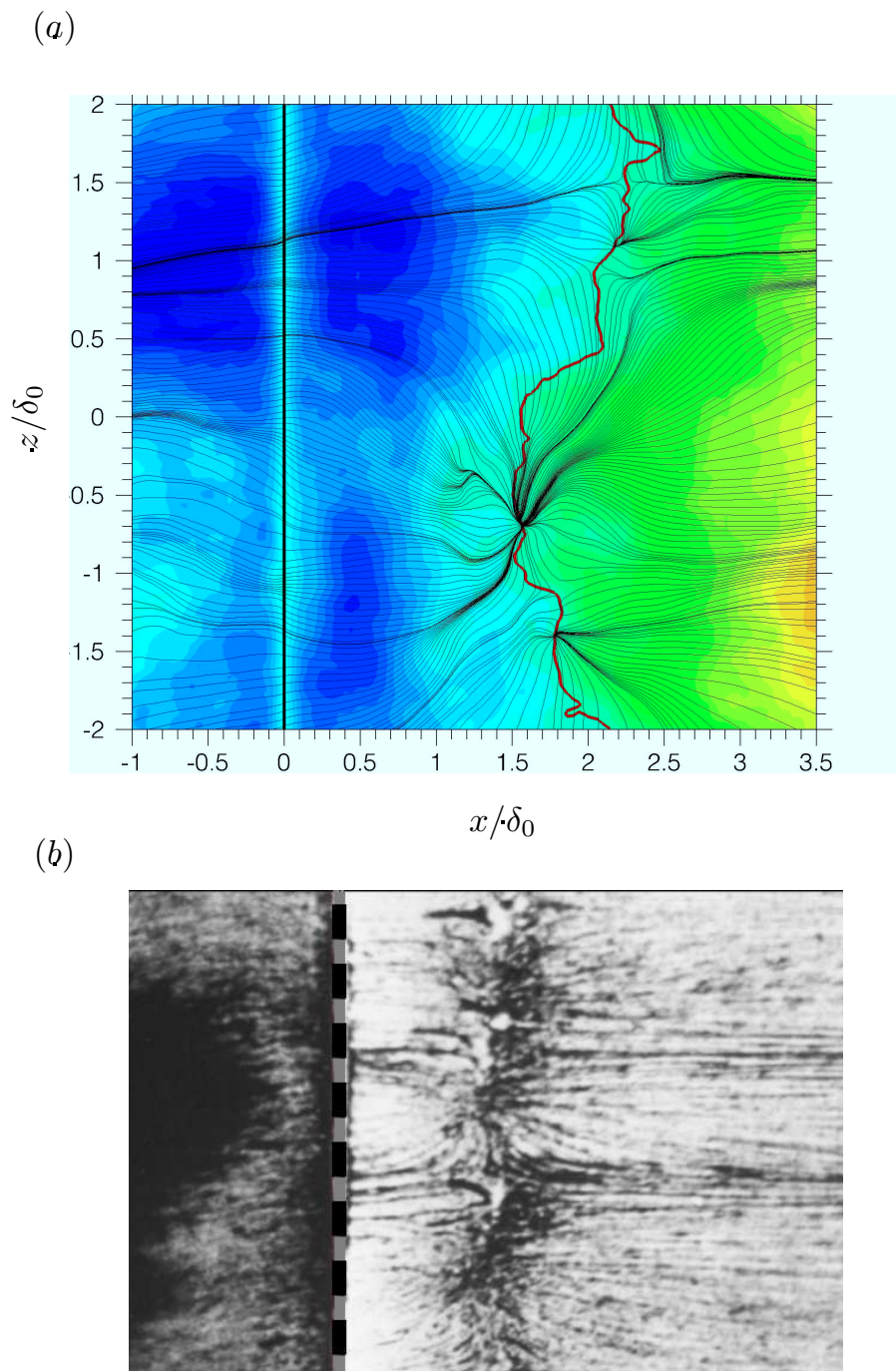


Figure 4.17.: (a) Numerical surface streamlines pattern. Contours of the time averaged local friction coefficient are shown. The thick solid line indicates the location of $\langle C_f \rangle = 0$ where the boundary layer reattaches. (b) Oil-flow visualization from the experiment [Zhel'tovodov and Yakovlev, 1986]. The thick dashed line indicates the position of the corner.

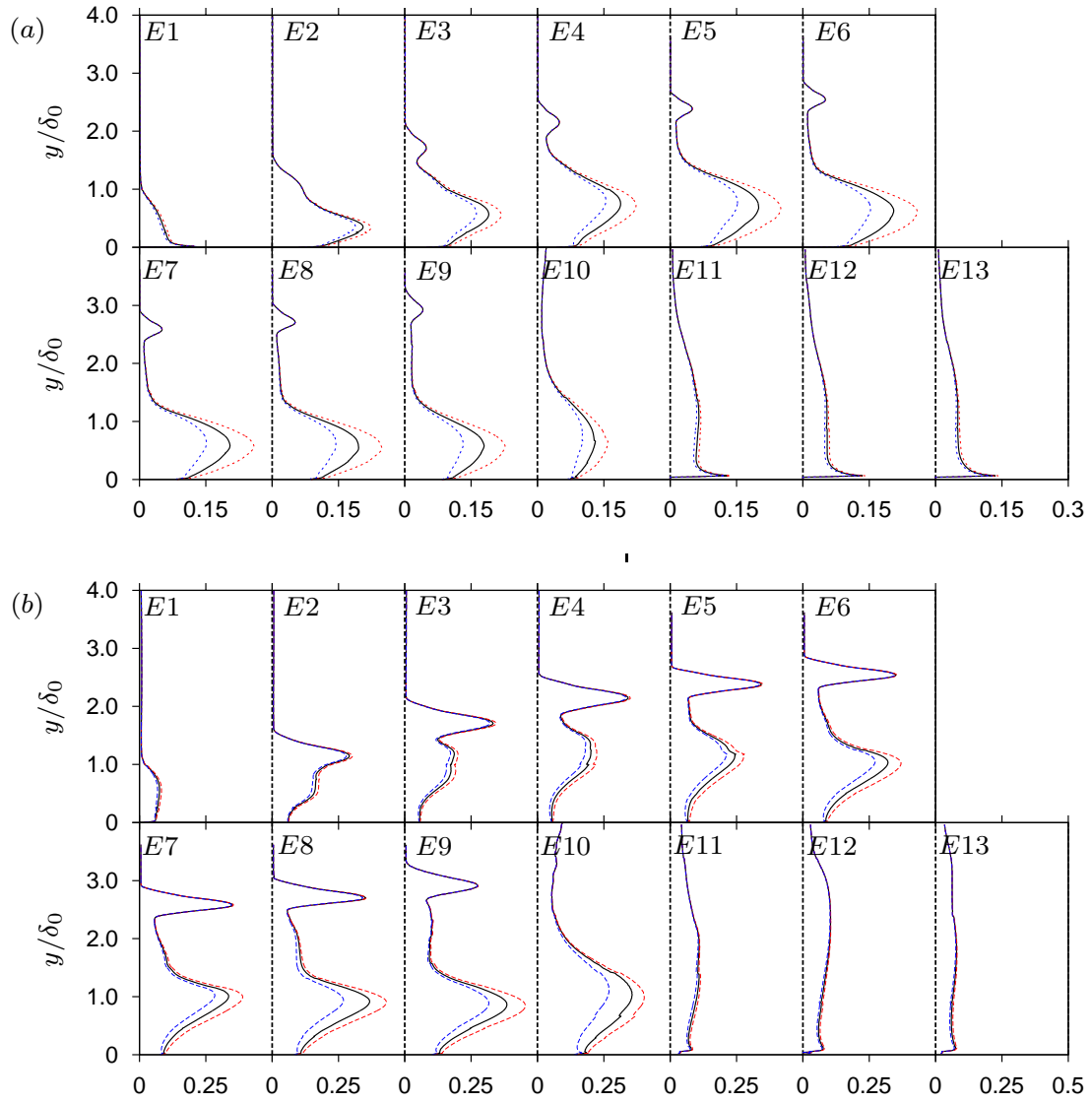


Figure 4.18.: (a) Streamwise velocity fluctuation $\sqrt{\langle u'_t u'_t \rangle}$, (b) Density fluctuations $\sqrt{\langle \rho' \rho' \rangle}$. --- Maximum values along the spanwise direction. --- Minimum values along the spanwise direction.

outer boundary layer is due to structures that originate in the shear layer and shed downstream after the Prandtl-Meyer expansion. For the density fluctuations, similar amplification effects are visible as for the velocity fluctuations. The secondary peak due to the shockwave unsteadiness has a higher value than the peak produced by the shear layer in section *E2*. Moving downstream, the first peak due to the shear layer increases while the second peak due to the shockwave motion decreases. This means that the amplitude of the shockwave movement decreases away from the wall.

In Figs.4.19(a) and 4.19(b), we show the Reynolds normal stress $\tau_{11} = \langle \rho u'' u'' \rangle$, the Reynolds shear stress $\tau_{12} = \langle \rho u'' v'' \rangle$ and the structure parameter $-\tau_{12}/\tau_{11}$ for all analysis stations. In agreement with previous findings of [Adams, 2000] and [Loginov et al., 2006], the maximum Reynolds normal-stress moves away from the wall to the detached shear layer downstream of the interaction at *E2* and stays there until section *E10* is reached. Downstream of the Prandtl-Meyer expansion a profile similar to the one of the incoming boundary layer is recovered in section *E11*, with slightly higher turbulence values in the outer region. The maximum Reynolds normal-stress is amplified by a factor of 4 while passing through the interaction from section *E1* to section *E2*. This amplification factor is in good agreement with the DNS results of [Adams, 2000]. The passage through the Prandtl-Meyer expansion reduces the Reynolds normal-stress to approximately the same value as in the incoming boundary layer. Again we find a slightly higher level in the outer region. In the same interval the maximum Reynolds shear-stress is amplified by a factor of around 10. This value is lower than what was estimated in the DNS of [Adams, 2000]. It agrees, however, very well with the range given by [Smits and Muck, 1987] for experiments on the 20° compression ramp configuration. A reason for this discrepancy could be related to the high Reynolds number of the present LES, which results in the flow conditions that are more similar to the experiments of [Smits and Muck, 1987].

The Prandtl-Meyer expansion has similar effects on the Reynolds shear-stress as on the Reynolds normal-stress discussed above. Fig. 4.19(c) shows the structure parameter $-\tau_{12}/\tau_{11}$, which indicates the level of anisotropy of the turbulence. In the incoming boundary layer it predicts a value of around 0.15, which agrees well with what has been shown by [Adams, 2000] and by [Loginov et al., 2006]. Peaks in the anisotropy can be found close to the shockwave and at lower intensity in the shear layer zone.

In Fig. 4.20 we show the Reynolds stress anisotropy maps for selected streamwise stations. As mentioned above, the interaction between boundary layer, flow separation and shock wave results in different amplification levels for the individual components of the Reynolds stress tensor. The corresponding change in anisotropy is characterized by the anisotropy tensor

$$b_{ij} = \frac{\langle \rho u_i'' u_j'' \rangle}{2\langle \rho \rangle \langle k \rangle} - \frac{1}{3} \delta_{ij}. \quad (4.1)$$

A representative picture of the turbulence state can be obtained by investigating the

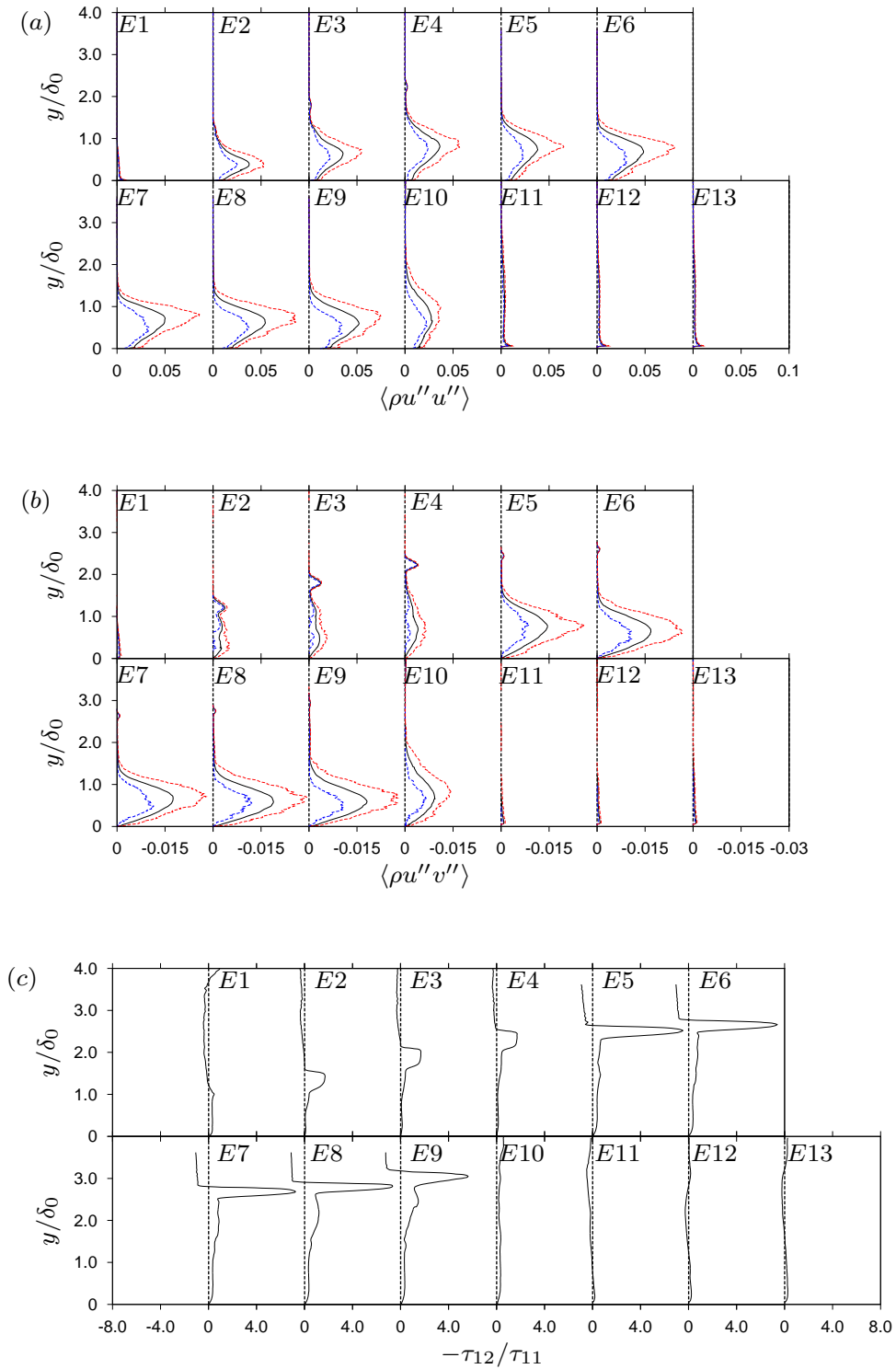


Figure 4.19.: (a) Reynolds normal stress $\tau_{11} = \langle \rho u_1'' u_1'' \rangle$, (b) Reynolds shear stress $\tau_{12} = \langle \rho u_1'' u_2'' \rangle$ and (c) the structure parameter $-\tau_{12}/\tau_{11}$ at measurements sections. --- Maximum values along the spanwise direction. -.- Minimum values along the spanwise direction.

evolution of the second and third invariant of this tensor

$$II_b = b_{ij}b_{ji}, \quad III_b = b_{ij}b_{jk}b_{ik}. \quad (4.2)$$

[Lumley, 1978] has shown that all realizable flow fields must lie inside an anisotropy invariant map, whose vertices constitute the asymptotic states of turbulence: one component turbulence, two component axisymmetric turbulence, and three dimensional isotropic turbulence.

In the incoming turbulent boundary layer (Fig. 4.20(a)) a two-component turbulent state is observed in the vicinity of the wall that evolves towards isotropic conditions away from the wall. These findings are in agreement with the DNS of [Pirozzoli et al., 2010a] and [Shahab et al., 2011]. A different behavior is found within the recirculation region (Fig. 4.20(b)). Turbulence in the separated flow closely resembles an isotropic state near the wall ($0.1 < y/\delta_0 < 0.2$). Further away from the wall it evolves towards an axisymmetric expansion state inside the detached mixing layer. The adverse pressure gradient acting along the compression ramp drives the turbulent fluctuations towards an axisymmetric compression state, as can be seen in Figs. 4.20(c) and 4.20(d) close to the wall. In the outer region, the anisotropy tensor indicates axisymmetric expansion, which is representative for the reattached shear layer that travels along the wall after the reattachment point. After passing the Prandtl-Meyer expansion, the turbulence slowly recovers a two-component state in the near wall region, which is similar to the incoming undisturbed turbulent boundary layer (Fig. 4.20(e)). The outer part of the boundary layer is however affected by the persisting shear layer and shows some evidence of axisymmetric expansion. In the station $E13$ (Fig. 4.20(f)), the turbulence state of the incoming boundary layer is almost recovered although the influence of the shear layer in the outer region is still visible.

4.6. Shock-system features

An instantaneous snapshot of the computed Schlieren-type visualization (Fig. 4.21(a)) reveals similarities with the experimental picture (Fig. 4.21(b)). The undisturbed boundary layer (1) is affected by the separation shock (2). The interaction results in the appearance of a reverse flow region (3) and of a separated shear layer (4) with traveling shocklets (5) above it. The compression in the reattachment region leads to the generation of the unsteady second stem (6) of the λ -shock configuration. The spanwise variation of the shock position causes some smearing of the shock position in the interaction region after averaging in the spanwise direction. The rearward stem of the λ -shock originating from the reattachment region features an highly unsteady character. As visible from an animation of a set of numerical Schlieren visualizations which is available as a supplement to the online version of the paper (<http://dentaku.aer.mw.tum.de/pub/grilli/SchlierenMovie.gif>), there are phases in which the second stem is clearly visible as unique structure and phases in which it is distributed in a series of shocklets. The animation also clearly highlights

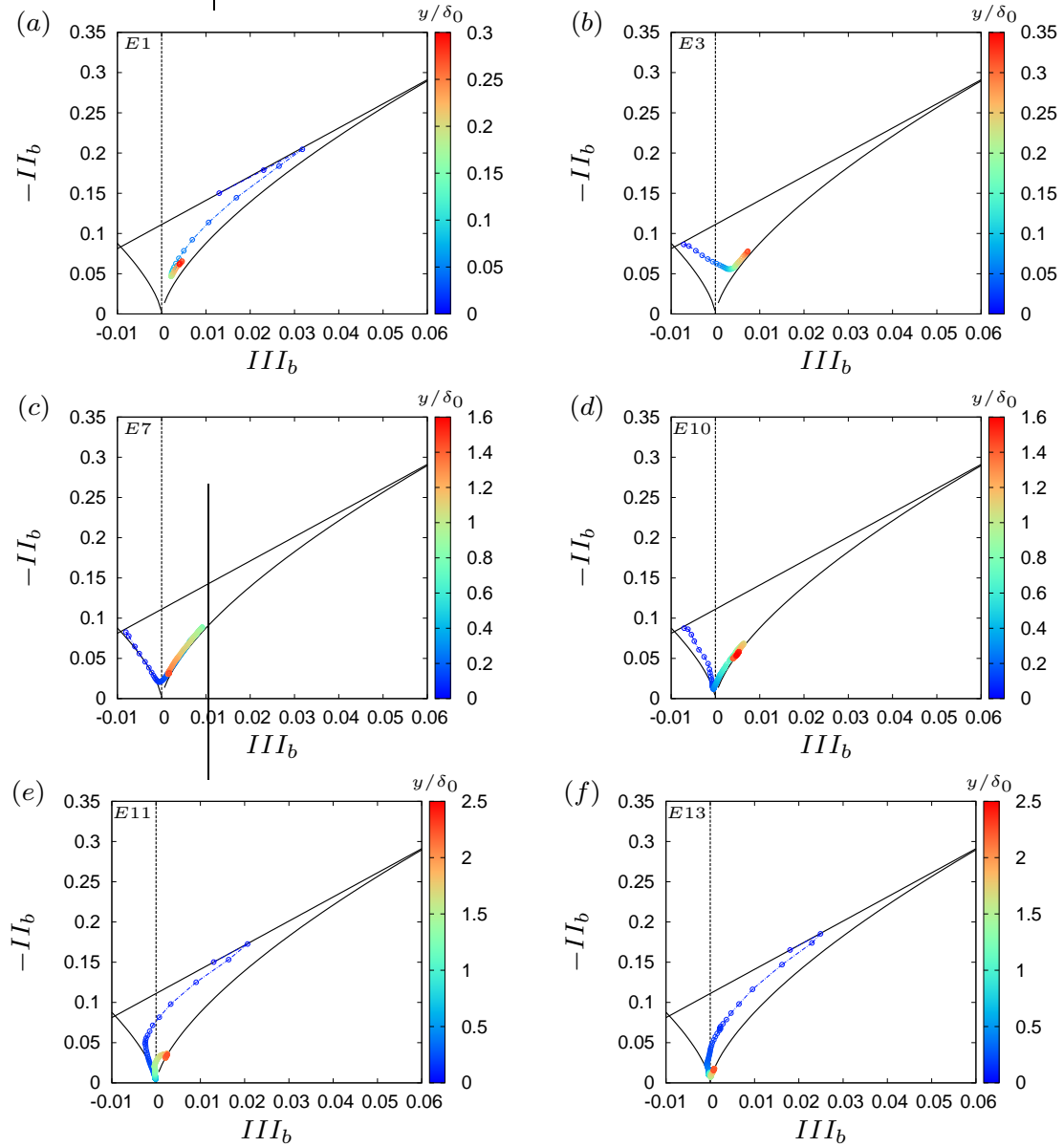


Figure 4.20.: Reynolds stress anisotropy invariant map evaluated at different stations. (a) station $E1$ $x/\delta_0 = -8.05$, (b) station $E3$ $x/\delta_0 = -2.93$, (c) station $E7$ $x/\delta_0 = 3.05$, (d) station $E10$ $x/\delta_0 = 7.56$, (e) station $E11$ $x/\delta_0 = 12.20$, (f) station $E13$ $x/\delta_0 = 19.25$. The color map indicates the distance from the wall y/δ_0 .

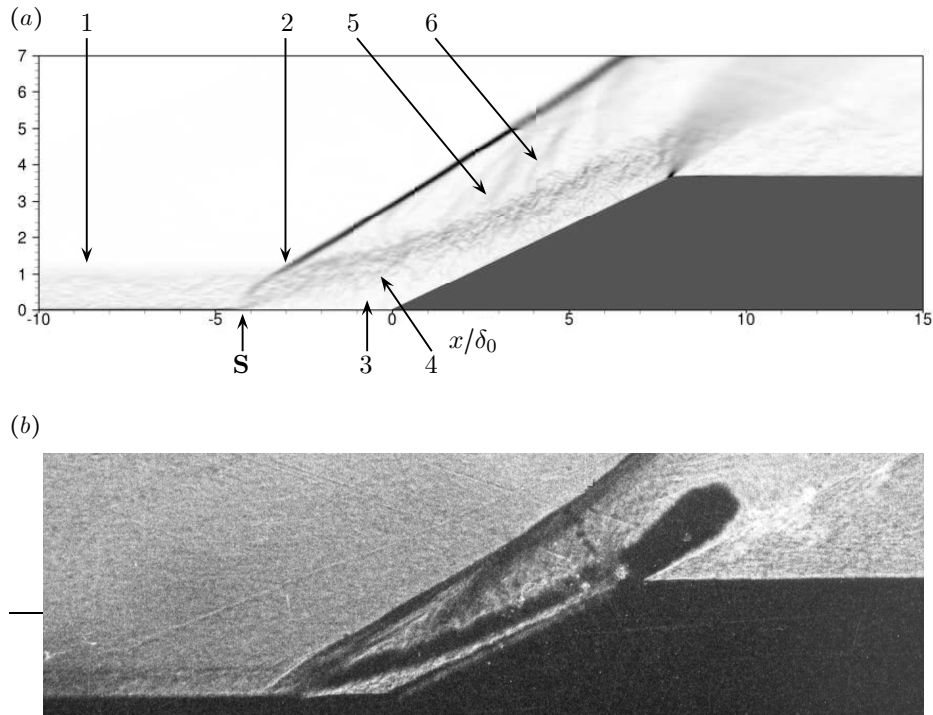


Figure 4.21.: Instantaneous representation of the flow by the Schlieren-type visualization. The computed density gradient averaged in spanwise direction $\|\nabla\rho\|$ (a) and experimental Schlieren visualization (b).

the unsteady motion of the shock system and the shedding of compression waves behind the main shock. As visible from the video, such compression waves travel in the region between the shear layer and the main oblique shock and then collapse in the second stem of the λ -shock, but they are not visible anymore as organized structures after passing through the Prandtl-Meyer expansion. The presence of such traveling shocklets is found to be responsible for the plateau region with high level of density fluctuations, that is visible in the Fig. 4.13(b), between the two peaks related to the shear layer and to the unsteady shock, respectively.

The most important feature of the shock-system is the low frequency unsteady motion featured by the main oblique shock. Evidence of the shock motion can be obtained by considering an instantaneous contour of the magnitude of the gradient of pressure on a streamwise-spanwise plane located at $y/\delta_0 \approx 0.1$, as given in Fig. 4.22. The figure shows the shock located upstream of the dashed line, which represents the mean shock location. The detected amplitude of the streamwise movement of the

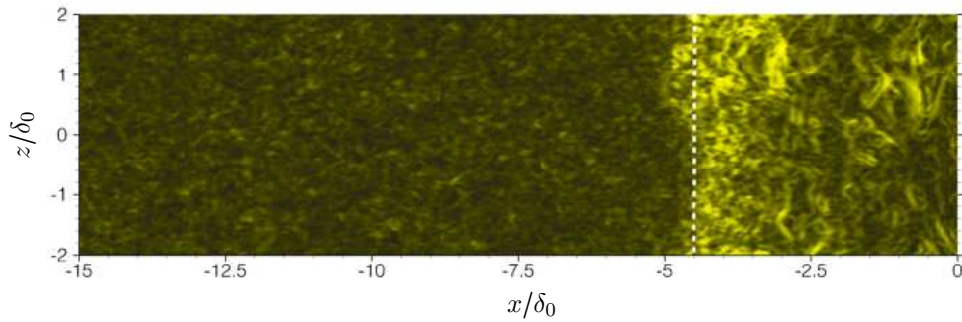


Figure 4.22.: Instantaneous snapshot of $\|\nabla p\|$ at $y/\delta_0 \approx 0.1$. The dashed line indicates the mean shock location.

shock is roughly $1 \delta_0$ at this wall-normal coordinate. In the considered timeframe, the shock is wrinkled along the spanwise direction, with an amplitude of about $0.5 \delta_0$, in accordance with what has been previously shown by [Wu and Martin, 2008]. An animation of a set of visualizations of the pressure gradient magnitude in the considered plane has been analyzed, showing that the shock is most of the time not wrinkled in spanwise direction. The presence of this instantaneous sharp corrugation of the shock could therefore be related to a local modification of the recirculation bubble located downstream or, as mentioned in the work of [Wu and Martin, 2008], to the presence of a low-speed structure in the incoming boundary layer, which is responsible for the upstream movement of the shock.

4. *Compression-Expansion corner flow*

5. Analysis of the unsteady shockwave behavior

In this chapter the unsteady features of the shockwave turbulent boundary layer interaction are investigated in order to extract the main properties of the mechanism that yields the low-frequency shock unsteadiness. For this purpose, the results from the computation presented in chapter 4 are analyzed by means of the Dynamic Mode Decomposition (DMD) [Schmid, 2010]. Characteristics of the shock motion are first analyzed in terms of wall-pressure data, after which a modal analysis is presented.

5.1. Wall pressure data analysis

We start by analyzing LES wall-pressure signals from 130 pressure probes placed along the median line of the wall. The probes are equally distributed within a region that extends from $x/\delta_0 = -6.5$ (upstream of the shock foot position) to $x/\delta_0 = 0$ (the ramp corner) with a spacing of $\Delta x/\delta_0 = 0.05$. The pressure signals have been recorded for each time-step. Figure 5.1(a) shows wall-pressure signals at three different positions, highlighting the characteristics of the shock motion. In the incoming boundary layer at $x/\delta_0 = -6.45$, the normalized magnitude is around unity with only small fluctuations. At $x/\delta_0 = -4.5$, the signal fluctuates between 1 and 2, showing peaks which are due to the motion of the shock. At position $x/\delta_0 = -0.25$, which is located in the separation region, the mean-pressure value increased to a value of 2.5, but distinct peaks are no longer visible. Nonetheless, we observe an increase of the pressure-fluctuation amplitude which corresponds to turbulence amplification by the shock. The corresponding weighted power spectral densities are plotted in Fig. 5.1(b). At the shock foot the peak frequency is $0.0039U_\infty/\delta_0$. Given the amount of available data from the simulation, a total number of 3 cycles of shock motion are considered in the present analysis. A Strouhal number $St_L = fL/U_\infty$ can be defined, where L is the length of the mean separation bubble ($L = 6.0\delta_0$ in the present LES), and gives $St_L = 0.0234$ which is consistent with the range of St_L indicated by [Dussauge et al., 2006].

The unsteady character of the interaction zone is further illustrated by the analysis of the wall-pressure spectra, shown in Fig. 5.2 as a function of the Strouhal number and the streamwise coordinate direction. Upstream of the interaction, the spectra show typical features of turbulent boundary layers with the dominant peak located at $St \approx 1$. A qualitative change is observed near the foot of the shock (highlighted with a dashed line in the figure), where substantial energy at lower frequencies is

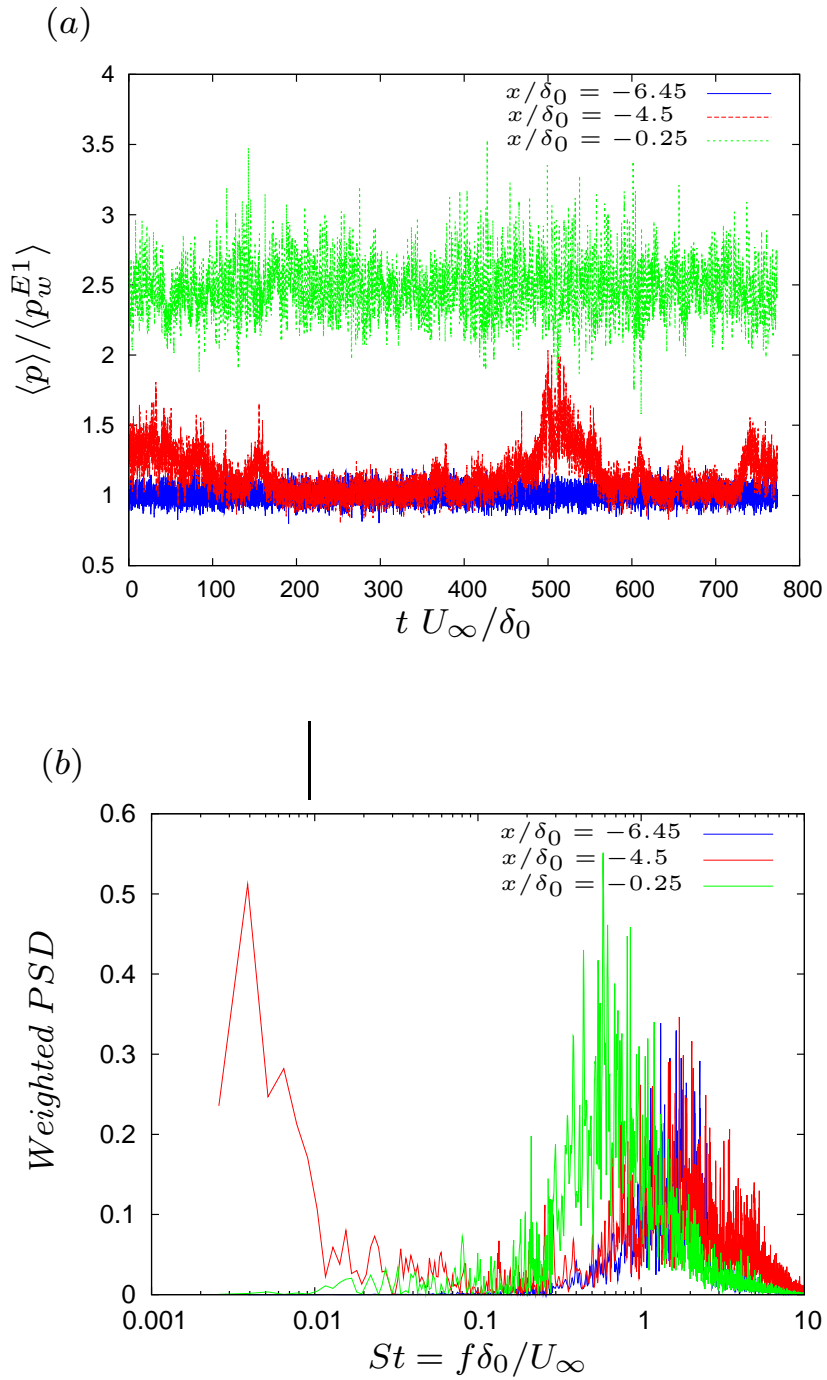


Figure 5.1.: (a) Wall-pressure signals and (b) corresponding weighted power spectral density at different streamwise locations relative to the ramp corner.

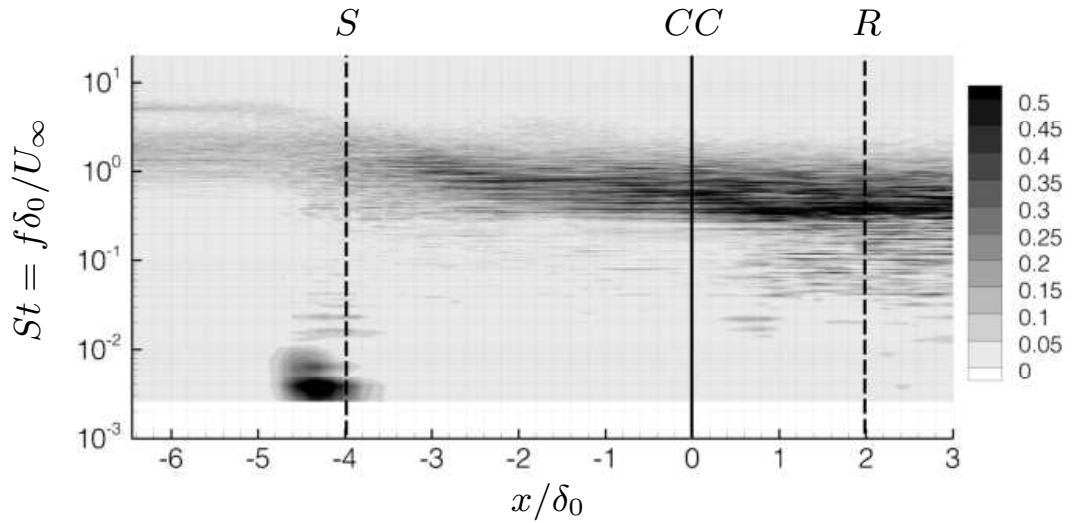


Figure 5.2.: Contours of the weighted power spectral density of wall-pressure in the St - x/δ_0 -plane. The power spectral density is normalized such that their integral over frequency is unity. Thirty contours levels have been used; the dashed vertical lines indicate the location of the separation S and reattachment point R respectively. The solid line indicates the position of the corner CC .

found, which confirms the low-frequency nature of the unsteadiness in this region. The low-frequency peak disappears when moving towards the center of the separation region and, approaching the reattachment location, the energy is evenly distributed over three decades of Strouhal numbers. This behavior is in good agreement with results reported by [Dupont et al., 2006].

5.2. Dynamic Mode Decomposition

Dynamic Mode Decomposition is a technique that allows for a modal analysis of a data sequence, without resorting to a numerical solver or an underlying model [Schmid, 2010, Schmid, 2011]. In the case of a linearized flow (i.e. a flow of small perturbation about a steady base flow), the extracted structures are equivalent to global eigenmodes. For a nonlinear flow, the decomposition produces modes that express the dominant dynamic behavior captured in the data sequence. Defining a temporal linear operator \mathbf{A} which advances our snapshot basis $\mathbf{V}(t)$ such that $\mathbf{V}(t^{n+1}) = \mathbf{A}\mathbf{V}(t^n)$, the DMD algorithm is able to extract approximate eigenvalues and eigenmodes of a reduced-order representation of the linear operator \mathbf{A} from

the data sequence. For sufficiently long sequences, each DMD-mode is then linked to a single temporal frequency [Rowley et al., 2009]. In this manner, DMD differs from the Proper Orthogonal Decomposition which generally does not yield direct information concerning the frequency of the detected modes. This feature makes DMD analysis particularly suited to the present study, since our goal is to focus on low-frequency unsteadiness. The DMD-algorithm has thus been applied to temporal snapshots of the spanwise-averaged flow variables in a subdomain containing the interaction region and the recirculation bubble. The box used for the DMD extraction has the exact dimensions of the contour plot shown in Fig. 5.5. The box extends in the range $-4.5 < x/\delta_0 < 2.4$ in the streamwise direction and in the range $0 < y/\delta_0 < 2$ in the wall normal direction. A total number of 770 snapshots, equispaced in time with $\Delta t U_\infty/\delta_0 = 1$ (allowing for a resolvable Strouhal number of 0.5), have been processed. The choice of sampling interval has been motivated by our aim of extracting the low-frequency unsteadiness; the high-frequency part of the spectrum is under-sampled. The eigenvalues λ of the reduced-order representation of the linear inter-snapshot mapping \mathbf{A} are shown in Fig. 5.3(a). All eigenvalues fall on the unit circle, which is expected for a saturated system. Fig. 5.3(b) shows the amplitude distribution for the detected modes, plotted versus the dimensionless frequency. The Strouhal number of the maximum-amplitude mode is found to be 0.00282, which is in good agreement with the value obtained from the Fourier-analysis of the wall-pressure data.

In order to assess whether the modes detected in the low-frequency regime are affected by aliasing, the DMD analysis has been performed successively decreasing the number of considered snapshots. A first analysis was carried out considering a total number of snapshots equal to 385 equispaced in time with $\Delta t U_\infty/\delta_0 = 2$ (allowing for a maximum resolvable Strouhal number of 0.25). In the second analysis a total number of snapshots equal to 257 equispaced in time with $\Delta t U_\infty/\delta_0 = 3$ (allowing for a maximum resolvable Strouhal number of 0.125). Fig. 5.2 shows the amplitude distribution of the modes obtained through the dynamic mode decomposition in the three different cases. It can be concluded that aliasing is negligible for the low frequency DMD modes that are considered in the next part of this analysis.

In addition, it has also been verified that the superposition of all the obtained DMD modes recovers a flowfield approximately resembling that of the full LES.

A reconstruction of the flow-field based on the four most dominant modes (labeled in Fig. 5.3(b)) has been carried out where the flow-field evolution of each mode has been recovered based on its frequency and amplitude and then added to the mean flow; Fig. 5.5 shows the result, displayed at four time instants. The mean position of the shock and the mean recirculation region are indicated by dashed lines. The choice of the number of modes to be considered was based on the decrease of the error norm obtained by adding another mode to the reconstruction. The norm was computed as $\sum_{t=0}^{t=2T} |s^{i+1}(t) - s^i(t)|/|s^i(t) - s^1(t)|$, where i equals the number of modes considered, and T is the period of the mode having the highest amplitude. With four DMD modes the error norm for the reconstructed fields is below 15%. The reconstructed flow exhibits a breathing motion, with the separation bubble expanding and shrinking periodically, and the shock moving forward-backward accordingly.

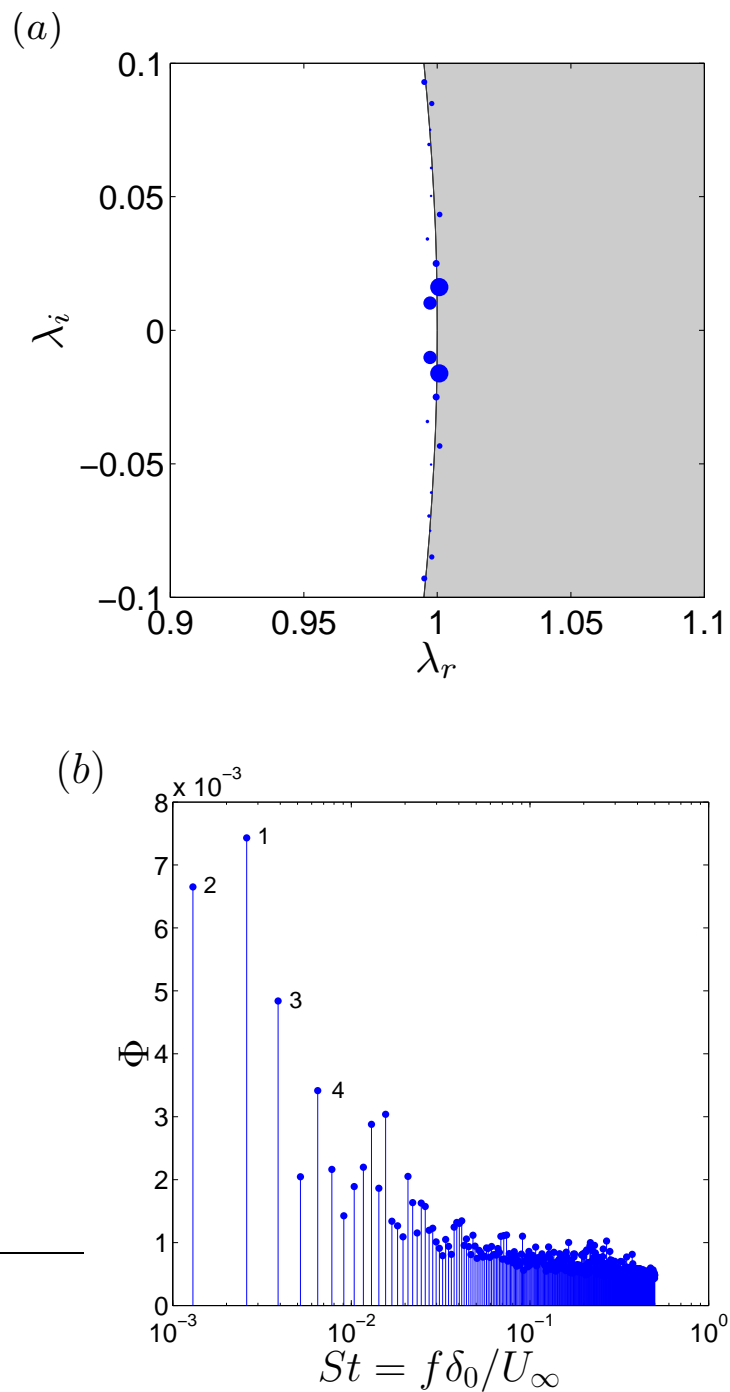


Figure 5.3.: (a) Close-up view of the eigenvalue distribution of the inter-snapshot mapping in the complex plane, detected by the DMD method. (b) Amplitude distribution of the detected modes.

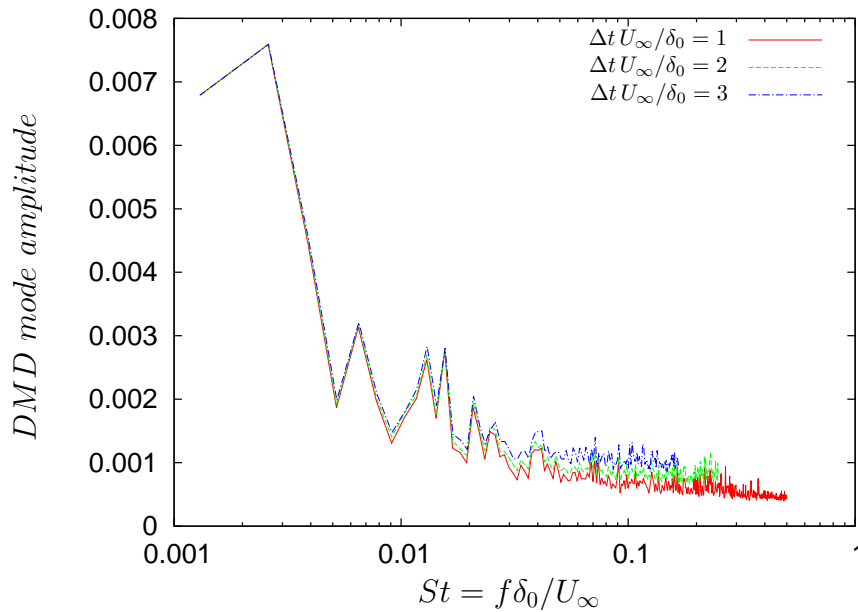


Figure 5.4.: Amplitude distribution of the detected modes with decreasing number of snapshots. — $\Delta t U_\infty/\delta_0 = 1$, - - - $\Delta t U_\infty/\delta_0 = 2$, - · - $\Delta t U_\infty/\delta_0 = 3$

Due to the low-frequency nature of the selected modes, no structures reminiscent of turbulence can be detected in the reconstruction.

In order to further investigate the features of the low-frequency unsteadiness, the shock location and the mass of the recirculation region versus time have been determined for the reconstructed flow. The four most dominant modes have successively been added one after the other to the mean flow, and mass of the recirculation region as well as the shock displacement have been computed for each resulting flowfield. The shock position was tracked away from the wall at $x/\delta_0 = -1.95$ and $y/\delta_0 = 1.75$. This location allows for a more precise definition of the shock position, since here is sharply developed and less affected by boundary-layer turbulence. The exact position of the shock was determined by computing the location of the maximum density gradient in x -direction. It should be noted that the extent of the shock motion reduces while moving away from the wall. Hence the extent of the shock motion as reported in the Fig. 5.6(b) is lower than typical shock-excursion values reported for the shock foot. An estimate of the actual value of the shock-motion amplitude in the proximity of the wall can be extracted from Fig. 5.2, where the region indicating high levels of energy in the low frequency regime extends from $x/\delta_0 = -4.75$ to $x/\delta_0 = -3.5$, giving a value for the shock-motion amplitude of $1.25 x/\delta_0$. The mass of the reverse flow region has been computed by considering the region of the flow where the u -velocity is negative. As can be seen in Fig. 5.6(a), the superimposition of the modes confirms a temporal asymmetry in the

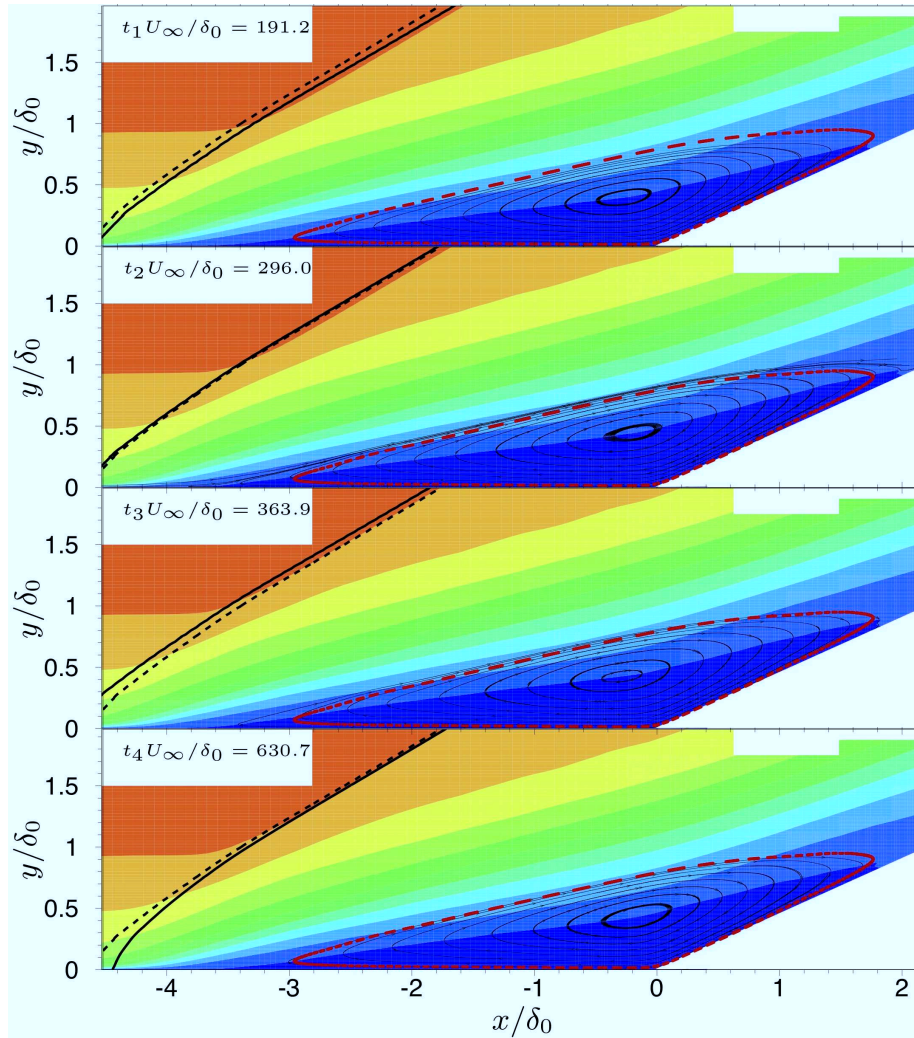


Figure 5.5.: Four snapshots from a reconstruction of the flow fields from a linear combination of the four most dominant dynamic modes. — Instantaneous oblique shock position. - - - - Mean oblique shock position. - - - - Mean recirculation region domain.

expansion-contraction cycle of the bubble and the oscillatory behavior of the shock. With all four modes superimposed on the mean flow, we observe that the mass increase in the recirculation region occurs significantly faster than the subsequent mass loss. Simultaneously, the downstream displacement of the shock is slower than its upstream motion. This is consistent with the model proposed by [Piponniau et al., 2009], in which contractions of the bubble stem from a mass entrainment process involving the shear layer above the recirculation region, whereas the dilations correspond to a large mass flux in the reverse direction, needed to maintain the recirculation region. In addition, a clear delay between changes of the recirculation region and the motion of the shock can be detected; the instants in time of respective minima and maxima are indicated in Fig. 5.6(a). An animation of the reconstructed flow field by the four dominant modes, available at the following link (<http://dentaku.aer.mw.tum.de/pub/grilli/LowFrequencyShockMotion.avi>), clearly highlights the modification of the separation bubble as the main driver of the shock motion.

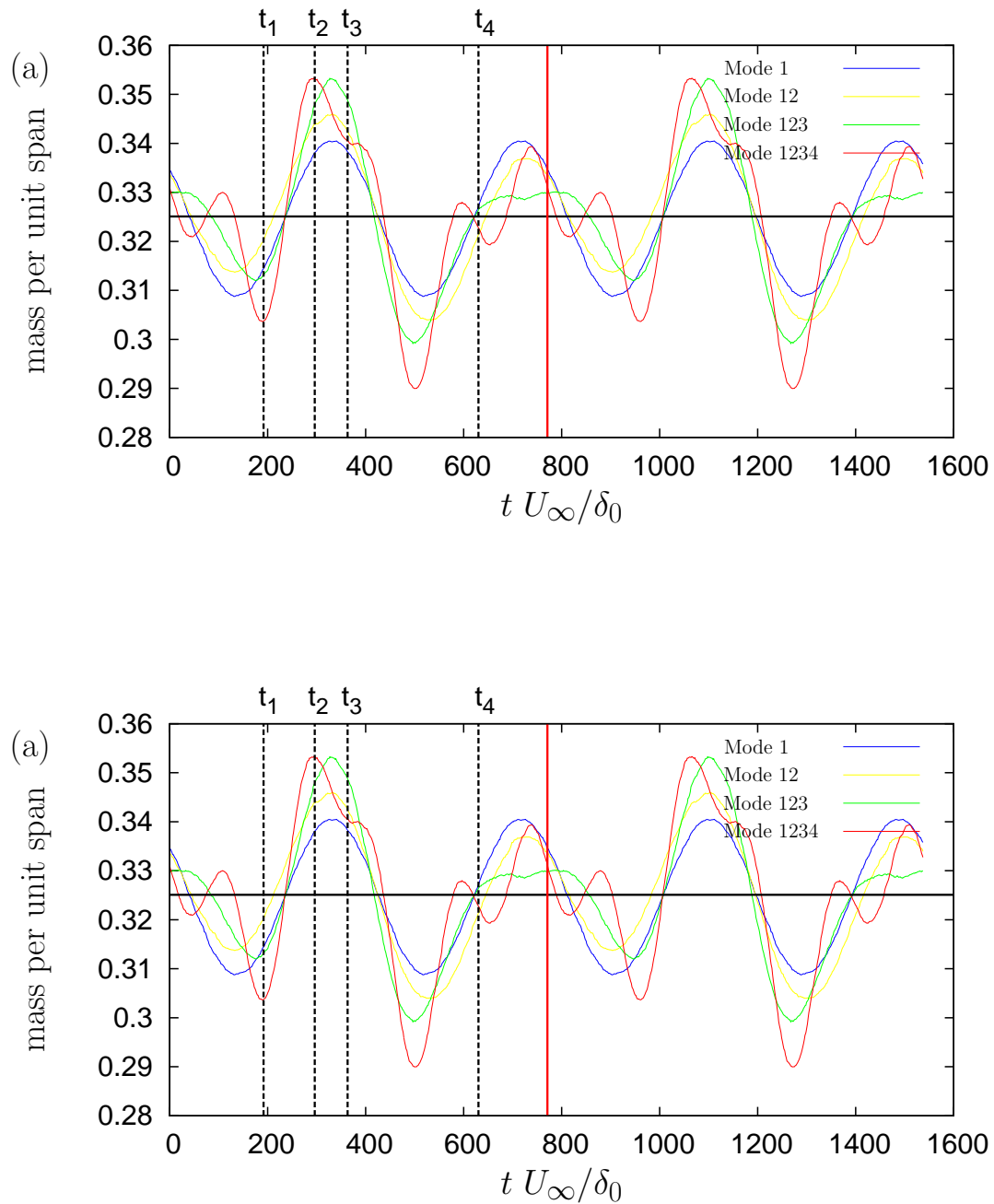


Figure 5.6.: (a) Temporal evolution of the mass (per unit span) of the reverse-flow region; (b) shock location versus time. Each variable has been extracted from a reconstructed flow-field sequence based on the four most dominant dynamic modes.

6. Conclusions

The shockwave turbulent boundary layer interaction (SWTBLI) is one of the most prevalent phenomena occurring in high-speed flight. From an engineering point of view, this phenomenon can have a significant impact on aircraft or rocket performance. The interaction of the shock with the turbulent boundary layer causes the separation of the boundary layer and the subsequent formation of a recirculation region. The main characteristic of such an interaction is the low-frequency unsteadiness of the shock producing amplified wall pressure fluctuations which, in turn, can cause strong buffeting of the underlying structure, eventually leading to failure due to fatigue.

In order to investigate this problem by means of large-eddy simulation, a numerical tool has been developed which features several aspects, each one of them playing a key role for the achievement of the final simulation target.

At first, a conservative immersed interface method for compressible viscous flows has been derived with the aim of being suitable for dealing with complex moving or stationary boundary problems. The method is based on a local modification of the classical finite volume scheme on Cartesian grids and on a Level-Set technique. These features make the implementation quite simple and allow to handle moving boundary problems in a straightforward way. Computations of laminar flows at low and high Mach numbers with and without heat transfer are performed and compared with results from the literature in order to evaluate the accuracy of the method.

The focus has then been moved to the analysis and validation of the proposed implicit-LES approach. Several LES of supersonic turbulent channel flows and supersonic turbulent boundary layers have been carried out. It has been shown that a significant improvement for the LES prediction in the case of wall bounded flows could be achieved by combining ALDM with a damping procedure based on a coherent structures detection criterion, as proposed by [Kobayashi, 2005] in the framework of explicit-LES.

Afterwards, the numerical investigation of a compression-decompression ramp flow has been performed. A high Reynolds number corresponding to experimental conditions has been achieved, allowing direct comparison of the data. The Reynolds number based on the incoming boundary-layer thickness is $Re_{\delta_0} = 132840$, the free stream Mach number is $M_\infty = 2.88$. The results are validated successfully against the reference experiment of [Zheltovodov et al., 1990]. Good agreement has been found for surface-pressure and skin-friction distributions, mean velocity profiles. Some differences have been detected for the comparison of density and velocity fluctuations, since this set of experimental data has been derived with an experiment that

was conducted at a smaller Reynolds number $Re_{\delta_0} = 63560$. Evidence for the existence of streamwise Görtler-like vortices has been found in the computational results. Such vortices are generated in the core of the recirculation region after the compression corner. They travel downstream along the ramp and they vanish after interacting with the Prandtl-Meyer expansion induced by the decompression corner. The effect of these structures on the spanwise mean-flow variation had to be taken into account when performing validation of numerical methods using experimental data. The computation has shown amplification of turbulence when interacting with the compression wave, with amplification factors that are found to be in accordance with previous numerical and experimental investigations conducted on compression-corner flows. It also has been shown that the interaction between turbulence and Prandtl-Meyer expansion results in a damping of the level of turbulent fluctuations. An analysis of the turbulence structure in the near wall region showed that the boundary layer recovers the typical streaky structures featured by the incoming zero pressure gradient turbulent boundary layer, after the passage through the decompression corner.

A particular focus has been posed on to the analysis of the low-frequency shock unsteadiness which has been detected in the numerical simulation. We have applied a Dynamic Mode Decomposition to a set of snapshots of spanwise averaged flow fields extracted from the LES. By considering a subdomain that contains both the shock and the recirculation region, we have identified and isolated a high-amplitude mode within the low-frequency regime. A temporal reconstruction of the flow field associated with the four most dominant modes has reproduced a pulsating separation bubble together with an oscillatory streamwise motion of the shock. This reduced description of the flow behavior (based on four dynamic modes) has captured the main features of the shock-wave turbulent-boundary-layer interaction: a clear coupling between the motion of the recirculation region and the motion of the shock, in agreement with experimental observations [Piponniau et al., 2009]. Our results have shown that SWTBLI cannot be described by a single mode, but that the superposition of the four dominant low-frequency modes is sufficient to recover the essential characteristics. These modes are phase locked and represent an asymmetric cycle for the shock motion as well as the periodic pumping of the separation bubble. As shown in Fig. 6.1, the DMD analysis shows negligible variations of the flow field in the region located upstream of the interaction. Based on this reconstruction we can state that upstream effects of the incoming boundary layer are irrelevant for the SWTBLI considered in our investigation. By adopting the scaling argument introduced from [Ganapathisubramani et al., 2006] the length of the structure capable of generating such a low frequency would exceed the domain considered upstream of the interaction in our simulation. At the same time, any of the structures that could be generated upstream would infer a low-frequency motion which is at least one order of magnitude higher than any of the four DMD modes considered in our analysis. Based on this evidence, we conclude that such structures cannot represent the driving mechanism for the low-frequency motion of the shock. Our results fully support the hypothesis that the observed SWTBLI phenomena are a consequence of

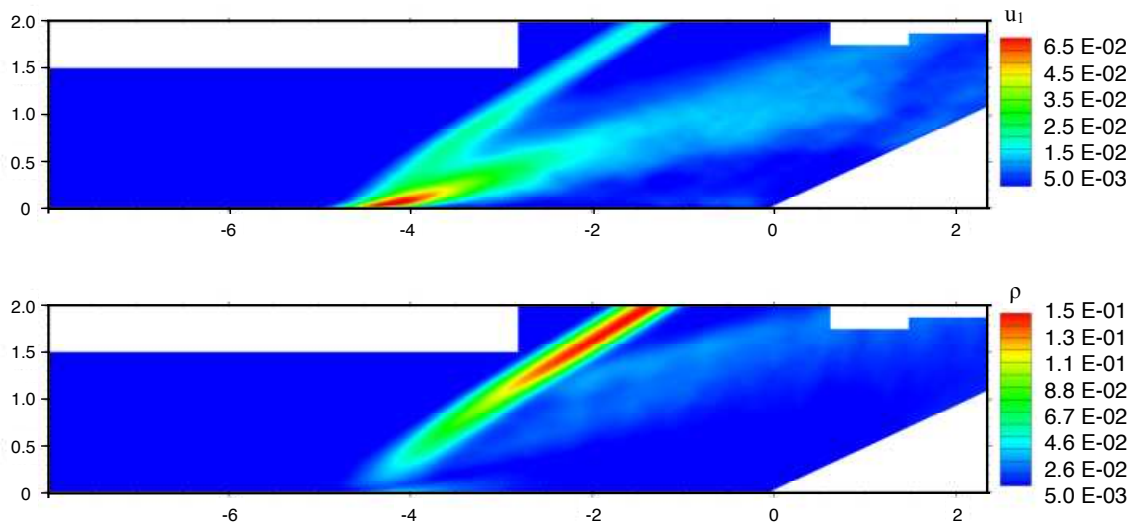


Figure 6.1.: (a) Contours of the amplitude of the superimposition of the four most dominant modes. (a) streamwise velocity u_1 (20 contours ranging from 0.005 to 0.065). (b) density ρ (20 contours ranging from 0.005 to 0.15).

the inherent dynamics between separation bubble and shock and are not driven by upstream coherent structures.

Finally, one possible application of the DMD analysis that has been conducted here could be in the field of aerodynamic design. The DMD modes that have been extracted from the analysis presented above could be used to generate a reduced-order model of the flow. As the mode basis is truncated to a limited number of low-frequency the most energetic modes, high frequencies are filtered and small scales could be neglected. Such model could be then adopted to assess the resistance of the underlying structural element.

A. Dynamic Mode Decomposition

In this appendix a brief description of the Dynamic Mode Decomposition approach will be given, together with a sample code and a validation test case that might be used for further implementations and developments.

A.1. General description

We consider at first a set of flow fields collected by sampling either direct numerical simulations or experimental data. A pre-processing stage might be required for experimental data in order to avoid possible interference effects coming from inherent measurement noise. The data should be ordered in the form of a snapshot sequence given by the matrix defined as follows

$$\mathbf{D}_1^N = \{\mathbf{d}_1, \mathbf{d}_2, \dots, \mathbf{d}_N\}, \quad (\text{A.1})$$

where \mathbf{d}_i stands for the i -th flow field. In the above definition, the subscript 1 denotes the first field of the sequence, while the superscript N denotes the last entry in the sequence. We then consider an ordered sequence of data separated by a constant sampling time Δt .

We consider now a linear mapping \mathbf{A} which relates the flow field d_i to the subsequent flow field d_{i+1} in the following way:

$$\mathbf{d}_{i+1} = \mathbf{A} \mathbf{d}_i \quad (\text{A.2})$$

This mapping is assumed to be the same over the sampling interval that spans in the snapshot range $[0, (N - 1)\Delta t]$. If the flow fields stem from a nonlinear process, this assumption resorts to a linear tangent approximation. For slowly varying systems, a multiple-scale argument can provide a foundation for the above assumption. In the special case of purely linear processes, no approximation is invoked by assuming a constant mapping. In any case, the assumption of a constant mapping between the snapshots \mathbf{d}_i allow for formulating the sequence of flow fields as a Krylov sequence

$$\mathbf{D}_1^N = \{\mathbf{d}_1, \mathbf{A} \mathbf{d}_1, \mathbf{A}^2 \mathbf{d}_1, \dots, \mathbf{A}^{N-1} \mathbf{d}_1\}. \quad (\text{A.3})$$

The main goal of the dynamic mode decomposition is the extraction of the dynamic characteristics (eigenvalues, eigenvectors, pseudoeigenvalues, energy amplification, resonance behaviour, etc.) of the dynamical process described by the linear operator \mathbf{A} and contained in the sequence \mathbf{D}_1^N . By Increasing the number of snapshots of

the data sequence given by \mathbf{D}_1^N beyond a critical number of snapshots, the vectors given by (A.2) become linearly dependent. Therefore, adding further flow fields \mathbf{d}_i to the data sequence will not improve the vector space spanned by \mathbf{D}_1^N . If this limit is reached, it is possible to express the vector \mathbf{d}_N as a linear combination of the previous, and linearly independent, vectors \mathbf{d}_i , $i = 1, \dots, N$ as follows

$$\mathbf{d}_N = a_1 \mathbf{d}_1 + a_2 \mathbf{d}_2 + \dots + a_{N-1} \mathbf{d}_{N-1} + \mathbf{r} \quad (\text{A.4})$$

which in a matrix form can be written as

$$\mathbf{d}_N = \mathbf{D}_1^{N-1} \mathbf{a} + \mathbf{r} \quad (\text{A.5})$$

with $\mathbf{a}^T = \{a_1, a_2, \dots, a_{N-1}\}$ being the vector of the linear combination coefficients and \mathbf{r} the residual vector. Considering the relations introduced above is possible to write:

$$\mathbf{A}\{\mathbf{d}_1, \mathbf{d}_2, \dots, \mathbf{d}_{N-1}\} = \{\mathbf{d}_2, \mathbf{d}_3, \dots, \mathbf{d}_N\} = \{\mathbf{d}_2, \mathbf{d}_3, \dots, \mathbf{D}_1^{N-1} \mathbf{a}\} + \mathbf{r} \mathbf{l}_{N-1}^T \quad (\text{A.6})$$

where $\mathbf{l}_{N-1}^T \in \mathbb{R}$ is a unit vector of dimension $N - 1$. Eq. (A.6) can be then expressed in matrix form as

$$\mathbf{A} \mathbf{D}_1^{N-1} = \mathbf{D}_2^N = \mathbf{D}_1^{N-1} \mathbf{S} + \mathbf{r} \mathbf{l}_{N-1}^T, \quad (\text{A.7})$$

where the matrix \mathbf{S} represents a companion matrix

$$\mathbf{S} = \begin{bmatrix} 0 & & & a_1 \\ 1 & 0 & & a_2 \\ & 1 & \ddots & \vdots \\ & & \ddots & \ddots & a_{N-2} \\ & & & 1 & a_{N-1} \end{bmatrix}. \quad (\text{A.8})$$

The only unknown elements in \mathbf{S} are the coefficients $\{a_1, a_2, \dots, a_{N-1}\}$, which represent the above mentioned $(N-1)$ -component linear approximation of the last sample \mathbf{d}_N in terms of the previous samples $\{\mathbf{d}_1, \mathbf{d}_2, \dots, \mathbf{d}_{N-1}\}$.

The eigenvalues of \mathbf{S} are approximations of the eigenvalues of the linear operator \mathbf{A} . The computation of \mathbf{S} then proceeds by computing the linear coefficients vector \mathbf{a} . The last element of a given data sequence \mathbf{d}_N is expressed as a linear combination of the previous elements of the sequence as stated in Eq. (A.5), whose least-squares solution, for a full-rank matrix \mathbf{D}_1^{N-1} is obtained through:

$$\mathbf{a} = \mathbf{R}^{-1} \mathbf{Q} \mathbf{d}_N \quad \text{with} \quad \mathbf{D}_1^{N-1} = \mathbf{Q} \mathbf{R}. \quad (\text{A.9})$$

Even though the decomposition based on a companion matrix \mathbf{S} is mathematically correct, a practical implementation yields an ill-conditioned algorithm that is often not capable of extracting more than the first or first two dominant dynamic modes. This is particularly true when the data stem from an experiment and are contaminated with noise and other uncertainties. For this reason, we choose a more robust

implementation that computes the *full* matrix $\tilde{\mathbf{S}}$ related to \mathbf{S} via a similarity transformation. The robustness requirement is achieved by a preprocessing step using a singular value decomposition of the data sequence $\mathbf{D}_1^{N-1} = \mathbf{U}\mathbf{\Sigma}\mathbf{V}^H$. Substituting the singular value decomposition $\mathbf{U}\mathbf{\Sigma}\mathbf{V}^H$ into Eq. (A.7) and rearranging the resulting expression, we obtain $\tilde{\mathbf{S}} = \mathbf{U}^H \mathbf{A} \mathbf{U} = \mathbf{U}^H \mathbf{D}_2^N \mathbf{V} \mathbf{\Sigma}^{-1}$. By recognizing that the matrix \mathbf{U} contains the proper orthogonal modes of the data sequence \mathbf{D}_1^{N-1} , the above operation resorts to a projection of the linear operator \mathbf{A} onto a proper-orthogonal-decomposition basis. A further advantage of this operation, besides a more robust calculation of the low-dimensional representation of \mathbf{A} , is the opportunity to account for a rank-deficiency in the data sequence \mathbf{D}_1^{N-1} via a restriction to a limited projection basis \mathbf{U} given by the non-zero singular values of $\mathbf{\Sigma}$ (or by singular values above a prescribed threshold). In our case, we obtain the following expression for the dynamic modes Φ_i :

$$\Phi_i = \mathbf{U} \Lambda_i, \text{ with } [\Lambda_i, \lambda_i] = \text{eiv}(\tilde{\mathbf{S}}) \quad (\text{A.10})$$

with Λ_i as the i -th eigenvector of $\tilde{\mathbf{S}}$, i.e. $\tilde{\mathbf{S}} \Lambda_i = \lambda_i \Lambda_i$ and \mathbf{U} as the right singular vectors of the snapshot sequence \mathbf{D}_1^{N-1} .

A.2. Matlab script for Dynamic Mode Decomposition

```
%%% -----
%%% Dynamic Mode Decomposition - Matlab script
%%% Muzio Grilli (2012)
%%% Matlab
%%% -----
%%% -----
%%%
%%% These routines may contain errors and bugs.They are distributed without
%%% warranty of merchantability, even without implied warranty of fitness
%%% for any particular purpose.
%%%
%%%      (c) by Muzio Grilli , 2012
%%%
%%% -----

clear all
clc

%%% -----
%%% Step 1: Define the location of the data and timestep
%%% -----

pathbase = '/Users/grilli/Documents/PhD_work/Dissertation/matlab/';
pathdata = 'data/';
pathres = 'dmd';

pathinput = strcat (pathbase,pathdata)
pathoutput = strcat (pathbase,pathres)
pathgrid = strcat (pathinput,'grid.dat')

dt = 1/19

%%% -----
%%% Step 2: Define dimensions of the snapshot basis ( M rows N columns )
%%% M defines the number of entries in each snapshot
%%% N defines the number of snapshot
%%% -----
%%% The grid contains 188 x 62 points = 11656
%%% -----

m = 11656
n = 80

md = 11656.d0
nd = 80.d0

npx = 188
npy = 62
```

A.2. Matlab script for Dynamic Mode Decomposition

```
nmode = 2

%%% -----
%%% Step 3: Define threshold value for singular values
%%% -----

soll = 10e-9

%%% -----
%%% Step 4: Read in the snapshot basis to form the  $D_{\{1\}}^{\{N-1\}}$  matrix
%%% -----

for i = 1 : n-1
    file      = strcat('File', num2str(i));
    pathfile = strcat(pathinput, file);
    D1(:,i)  = dlmread(pathfile);
end

%%% -----
%%% Step 5: Read in the snapshot basis to form the  $D_{\{2\}}^{\{N\}}$  matrix
%%% -----

for i = 2 : n
    j = i - 1;
    file      = strcat('File', num2str(i));
    pathfile = strcat(pathinput, file);
    D2(:,j)  = dlmread(pathfile);
end

%%% -----
%%% Step 6: Execute economy size SVD of  $D_{\{1\}}^{\{N-1\}}$ 
%%% -----

[U,S,V] = svd(D1,'econ');
Sval    = diag(S);

%%% -----
%%% Step 7: Compute singular values entries above the threshold
%%% -----

r = 0;
for i = 1 : n - 1
    if Sval(i) > soll
        r = r + 1;
    end
end

Smax = max(Sval)
Smin = min(Sval)

%%% discarded percentage of total variance
```

A. Dynamic Mode Decomposition

```
discarded = 100 - (sumsqr(Sval(1:r))*100/sumsqr(Sval))
```

```
%%% -----  
%%% Step 8: Extract portion of the matrixes  
%%% -----
```

```
Up = U(:,1:r);  
Sp = S(1:r,1:r);  
Vp = V(:,1:r);  
Vt = V';  
Vtp = Vt(1:r,:);
```

```
%%% -----  
%%% Step 9: Compute inverse of the singular values diagonal matrix S  
%%% -----
```

```
Spinv = inv(Sp);
```

```
%%% -----  
%%% Step 10: Compute matrix  $L1 = U^H * D_{\{2\}}^{-1}$   
%%% -----
```

```
L1 = Up' * D2;
```

```
%%% -----  
%%% Step 11: Compute matrix  $L2 = V * S^{-1}$   
%%% -----
```

```
L2 = Vp * Spinv;
```

```
%%% -----  
%%% Step 12: Compute matrix  $L = L1 * L2$   
%%% -----
```

```
L = L1 * L2;
```

```
%%% -----  
%%% Step 13: Compute eigenvalues and eigenvectors of the L matrix  
%%% -----
```

```
[eivVec,eivVal] = eig(L);  
eivarray = diag(eivVal);
```

```
%%% -----  
%%% Step 14: Compute unscaled Dynamic Modes  
%%% -----
```

```
X1 = Up * eivVec;
```

```
%%% -----  
%%% Step 15: Compute Dynamic Modes amplitudes
```

```
%%% -----  
d=X1\D1(:,1);  
amplitude=abs(d);  
%%% -----  
%%% Step 16: Compute scaled Dynamic Modes  
%%% -----  
X=X1*diag(d);  
%%% -----  
%%% Step 17: Reconstruction  
%%% -----  
for i = 1 : n - 1  
    VandermondeMatrix(:,i) = eivarray.^(i-1);  
end  
Flowfield=X*VandermondeMatrix;  
Flowfield=real(Flowfield);  
relErr = norm((D1-Flowfield),'fro')/norm(Flowfield,'fro')
```

A.3. Validation example

A validation example is also given here as a reference for further implementations of the dynamic mode decomposition. The data refers to a series of visualizations of a flame, which is available at the following link (<http://dentaku.aer.mw.tum.de/pub/grilli/DMDcase>). One of the snapshots is given in the figure given below:

Results from the dynamics mode decomposition of the database are also given in terms of eigenvalue distribution and detected dynamic modes amplitudes with respect to their own frequency.

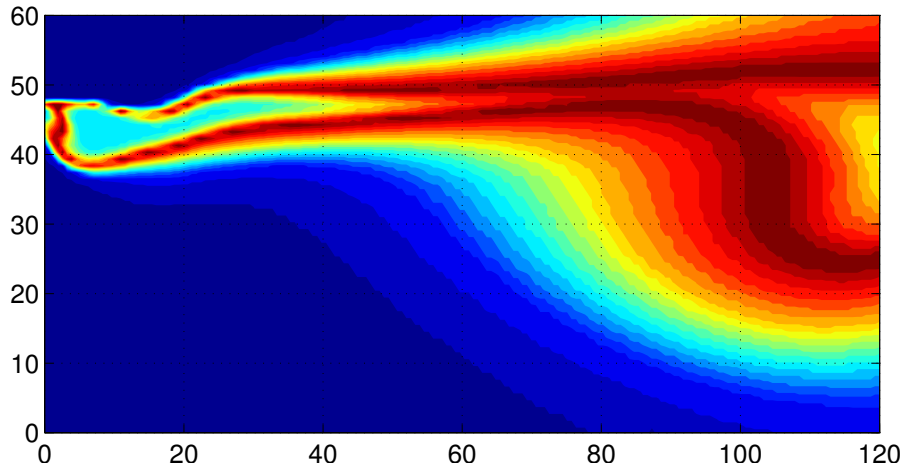


Figure A.1.: Snapshot from the flame visualization database.

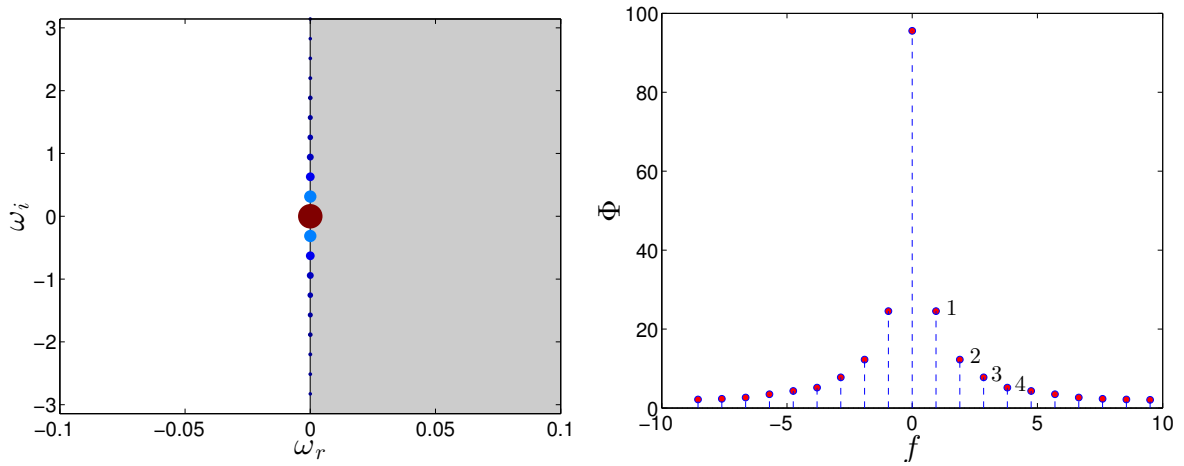


Figure A.2.: DMD spectrum for the flame visualization example. (a) Time-stepper spectrum visualization. The color and symbol size of the eigenvalues indicate the coherence of the associated dynamic modes. (b) amplitudes distribution with respect to the frequency. The spectrum is symmetric since the post-processed data is not complex.

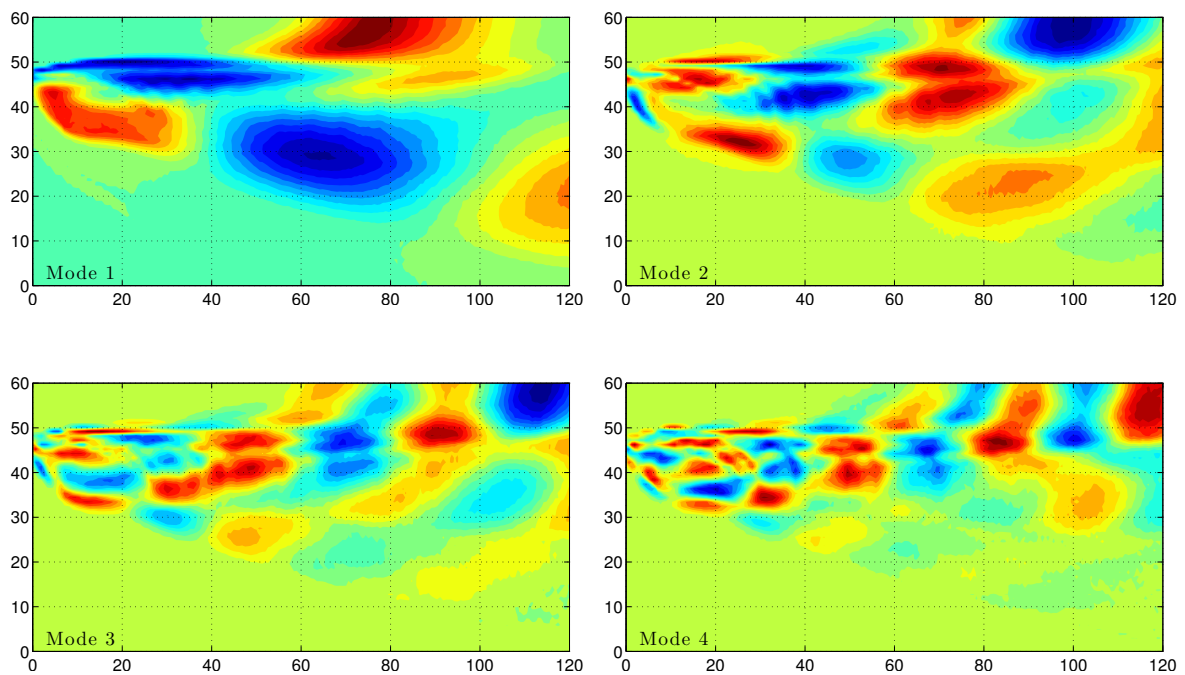


Figure A.3.: Spatial distribution of the first four most dominant dynamic modes.

Bibliography

- [Adams, 2000] Adams, N. (2000). Direct simulation of the turbulent boundary layer along a compression ramp at $Ma = 3$ and $Re_\theta = 1685$. *J. Fluid Mech.*, 420:47–83.
- [Adams et al., 2004] Adams, N., Hickel, S., and Franz, S. (2004). Implicit subgrid-scale modeling by adaptive deconvolution. *J. Comp. Phys.*, pages 412–431.
- [Adrian and Meinhart, 2000] Adrian, R. J. and Meinhart, C. D. (2000). Vortex organization in the outer region of the turbulent boundary layer. *J. Fluid Mech.*, 422:1–54.
- [Ardonceanu et al., 1979] Ardonceanu, P., Lee, D., Deroquefort, T., and Goethals, R. (1979). Details of a shock-separated turbulent boundary-layer at a compression corner. *AGARD CP*, 14(271):8–14.
- [Baars et al., 2012] Baars, W. J., Tinney, C. E., Ruf, J H Brown, A. M., and McDaniels, D. M. (2012). Wall pressure unsteadiness and side loads in overexpanded rocket nozzles. *AIAA J.*, 50:61–73.
- [Beresh et al., 2002] Beresh, S., Clemens, N., and Dolling, D. (2002). Relationship between upstream turbulent boundary-layer velocity fluctuations and separation shock unsteadiness. *AIAA J.*, 40:2412–2422.
- [Blevins, 1990] Blevins, R. (1990). *Flow induced Vibrations*. Van Nostrand Reinhold, New York, NY.
- [Borazjani et al., 2008] Borazjani, I., Ge, L., and Sotiropoulos, F. (2008). Curvilinear immersed boundary method for simulating fluid stucture interaction with complex 3d rigid bodies. *J. Comp. Phys.*, 227:7587–7620.
- [Bradshaw, 1977] Bradshaw, P. (1977). Compressible turbulent shear layers. *Annu. Rev. Fluid Mech.*, 9:1–33.
- [Brown et al., 2002] Brown, A., Ruf, J., Reed, D., D’Agostino, M., and Keanini, R. (2002). Characterization of side load phenomena using measurement of fluid-structure interaction. *AIAA Joint Propulsion Conf.*, *AIAA Paper No. 2002-3999*.
- [Chen and Chakravarthy, 1994] Chen, C. L. and Chakravarthy, S. R. (1994). Numerical investigation of separated nozzle flows. *AIAA J.*, 32:1836–1843.

- [Coleman et al., 1995] Coleman, G. N., Kim, J., and Moser, R. (1995). A numerical study of turbulent supersonic isothermal-wall channel flow. *J. Fluid Mech.*, pages 159–183.
- [Coutanceau and Bouard, 1977] Coutanceau, M. and Bouard, R. (1977). Experimental determination of the main features of the viscous flow in the wake of a circular cylinder in uniform translation. part 1. steady flow. *J. Fluid Mech.*, 79:231–256.
- [De Palma et al., 2003] De Palma, P., de Tullio, M., Pascazio, G., and Napolitano, M. (2003). An immersed boundary method for compressible flows. *J. Comp. Phys.*, 192:593–623.
- [Deardorff, 1970] Deardorff, J. W. (1970). A numerical study of three-dimensional turbulent channel flow at large Reynolds numbers. *J. Fluid Mech.*, 41:453–480.
- [Deck and Guillen, 2002] Deck, S. and Guillen, P. (2002). Numerical simulation of side loads in an ideal truncated nozzle. *Journal of Propulsion and Power*, 18:261–269.
- [Delery, 1985] Delery, J. M. (1985). Shock wave/turbulent boundary layer interaction and its control. *Progress In Aerospace Sciences*, 22(4):209–280.
- [Delery and Bur, 2000] Delery, J. M. and Bur, R. S. (2000). The physics of shock wave/boundary layer interaction control- Last lessons learned. *ONERA, TP no. 2000-181*.
- [Dennis and Chang, 1970] Dennis, S. C. R. and Chang, G. Z. (1970). Numerical solutions for steady flow past a circular cylinder at Reynolds number up to 100. *J. Fluid Mech.*, 42:471–489.
- [Dolling, 2001] Dolling, D. S. (2001). Fifty years of shock-wave/boundary-layer interaction research: what next? *AIAA J.*, 39:1517–1530.
- [Ducros et al., 2000] Ducros, F., Laporte, F., Souleres, T., Guinot, V., Moinat, P., and Caruelle, B. (2000). High-order fluxes for conservative skew-symmetric-like schemes in structured meshes: application to compressible flows. *J. Comp. Phys.*, 161(1):114–139.
- [Dumnov, 1996] Dumnov, G. E. (1996). Unsteady side-loads acting on the nozzle with developed separation zone. *AIAA Joint Propulsion Conf., AIAA Paper No. 96-3220*.
- [Dupont et al., 2006] Dupont, P., Haddad, C., and Debieve, J. (2006). Space and time organization in a shock-induced separated boundary layer. *J. Fluid Mech.*, 559:255–277.

- [Dussauge et al., 2006] Dussauge, J., Dupont, P., and Debieve, J. (2006). Unsteadiness in shock wave boundary layer interactions with separation. *Aerosp. Sci. Tech.*, 10:85–91.
- [Fernholz and Finley, 1977] Fernholz, H. and Finley, P. (1977). A critical compilation of compressible turbulent boundary layer data. *AGARDograph*, 223.
- [Fernholz and Finley, 1981] Fernholz, H. and Finley, P. (1981). A further compilation of compressible boundary layer data with a survey of turbulence data. *AGARDograph*, 263.
- [Floryan, 1991] Floryan, J. M. (1991). Three-dimensional heat-and mass-transfer effects across high-speed reattaching flows. *Prog. Aerospace Sci.*, 28:235–271.
- [Fornberg, 1980] Fornberg, B. (1980). A numerical study of the steady viscous flow past a circular cylinder at low Reynolds number. *J. Fluid Mech.*, 79:231–256.
- [Foysi et al., 2004] Foysi, H., Sarkar, S., and Friedrich, R. (2004). Compressibility effects and turbulence scalings in supersonic channel flow. *J. Fluid Mech.*, 509:207–216.
- [Frey and Hagemann, 1999] Frey, M. and Hagemann, G. (1999). Flow separation and side-loads in rocket nozzles. *AIAA Joint Propulsion Conf., AIAA Paper No. 99-2815*.
- [Frey and Hagemann, 2000] Frey, M. and Hagemann, G. (2000). Restricted shock separation in rocket nozzles. *Journal of Propulsion and Power*, 3:478–484.
- [Ganapathisubramani et al., 2006] Ganapathisubramani, B., Clemens, N., and Dolling, D. (2006). Effects of upstream boundary layer on the unsteadiness of shock induced separation. *J. Fluid Mech.*, 585:369–394.
- [Garnier et al., 2009] Garnier, E., Adams, N., and Sagaut, P. (2009). *Large Eddy Simulation for Compressible Flows*. Springer.
- [Ghosal, 1996] Ghosal, S. (1996). An analysis of numerical errors in large-eddy simulations of turbulence. *J. Comp. Phys.*, 125:187–206.
- [Grove et al., 1998] Grove, A., Shair, F., Petersen, E., and Acrivos, A. (1998). An experimental investigation of the steady separated flow past a circular cylinder. *J. Fluid Mech.*, 19:60–80.
- [Guarini et al., 2000] Guarini, S. E., Moser, R. D., and Shariff, K. (2000). Direct numerical simulation of a supersonic turbulent boundary layer at Mach 2.5. *J. Fluid Mech.*, 414:1–33.
- [Hagemann et al., 2002] Hagemann, G., Frey, M., and Koschel, W. (2002). Appearance of restricted shock separation in rocket nozzles. *Journal of Propulsion and Power*, 3:577–584.

- [Harten et al., 1997] Harten, A., Engquist, B., Osher, S., and Chakravarthy, S. R. (1997). Uniformly High Order Accurate Essentially Non-oscillatory Schemes, III. *J. Comp. Phys.*, 131(1):3–47.
- [Hartmann et al., 2008] Hartmann, D., Meinke, M., and Schröder, W. (2008). An adaptive multilevel multigrid formulation for cartesian hierarchical grid methods. *Computer & Fluids*, 37:1103–1125.
- [Hickel, 2007] Hickel, S. (2007). Implicit subgrid-scale modeling for large eddy simulation of compressible flows and shock turbulence interaction. *Phys. Fluids*, submitted.
- [Hickel, 2012] Hickel, S. (2012). Implicit subgrid-scale modeling for large eddy simulation of compressible flows and shock turbulence interaction. *Phys. Fluids*, submitted.
- [Hickel et al., 2006] Hickel, S., Adams, N. A., and Domaradzki, J. A. (2006). An adaptive local deconvolution method for implicit les. *J. Comput. Phys.*, 213:413–436.
- [Hickel and Larsson, 2008] Hickel, S. and Larsson, J. (2008). An adaptive local deconvolution model for compressible turbulence. *Proceedings of the Summer Program*, page 85.
- [Hu et al., 2006] Hu, X., Khoo, B., and Adams, N. (2006). A conservative interface method for compressible flows. *J. Comp. Phys.*, 219(1):553–578.
- [Huang et al., 1995] Huang, P., Coleman, G., and Bradshaw, P. (1995). Compressible turbulent channel flows: DNS results and modelling. *J. Fluid Mech.*, 305:185–218.
- [Inger, 1977] Inger, G. (1977). Three-dimensional heat-and mass-transfer effects across high-speed reattaching flows. *AIAA J.*, 15:383–389.
- [Jackson et al., 2001] Jackson, A., Hillier, R., and S., S. (2001). Experimental and computational study of laminar cavity flows at hypersonic speeds. *J. Fluid Mech.*, 427:329–358.
- [Jiang and Shu, 1998] Jiang, G. and Shu, C. (1998). Efficient implementation of weighted ENO schemes. *Phys. Fluids*, 126:202–228.
- [Jimenez and Moin, 1991] Jimenez, J. and Moin, P. (1991). The minimal flow unit in near-wall turbulence. *J. Fluid Mech.*, 225:213–240.
- [Jimenez and Pinelli, 1999] Jimenez, J. and Pinelli, A. (1999). The autonomous cycle of near-wall turbulence. *J. Fluid Mech.*, 389:335–359.
- [Kim et al., 1971] Kim, H. T., Kline, S. J., and Reynolds, W. C. (1971). The production of turbulence near a smooth wall in a turbulent boundary layer. *J. Fluid Mech.*, 50:133–160.

- [Kim et al., 1987] Kim, J., Moin, P., and Moser, R. (1987). Turbulence statistics in fully developed channel flow at low Reynolds number. *J. Fluid Mech.*, 177(1):133–166.
- [Klein et al., 2003] Klein, M., Sadiki, A., and Janicka, J. (2003). A digital filter based generation of inflow data for spatially developing direct numerical or large eddy simulations. *J. Comp. Phys.*, 186:652–665.
- [Kobayashi, 2005] Kobayashi, H. (2005). The subgrid-scale models based on coherent structures for rotating homogeneous turbulence and turbulent channel flow. *Phys. Fluids*, 17(4):045104.
- [Kobayashi et al., 2008] Kobayashi, H., Ham, F., and Wu, X. (2008). Application of a local sgs model based on coherent structures to complex geometries. *International Journal of Heat and Fluid Flow*, pages 640–653.
- [Kolmogorov, 1991] Kolmogorov, A. N. (1991). Dissipation of Energy in the Locally Isotropic Turbulence. *Royal Society of London Proceedings Series A*, 434:15–17.
- [Kravchenko and Moin, 1997] Kravchenko, A. and Moin, P. (1997). On the effect of numerical errors in large-eddy simulation of turbulent flows. *J. Comp. Phys.*, 130:310–322.
- [Kreplin and Eckelmann, 1979] Kreplin, H. P. and Eckelmann, H. (1979). Behavior of the three fluctuating velocity components in the wall region of a turbulent channel flow. *Phys. Fluids*, 22(7):1233.
- [Larsson and Lele, 2009] Larsson, J. and Lele, S. (2009). Direct numerical simulation of canonical shock/turbulence interaction. *Phys. Fluids*, 21:101–126.
- [Lewis et al., 1968] Lewis, J., Kubota, T., and L., L. (1968). Experimental investigation of supersonic laminar, two-dimensional boundary-layer separation in a compression corner with and without cooling. *AIAA J.*, 6:7–14.
- [Linnick, 2003] Linnick, M.N. and Fasel, H. (2003). A high-order immersed boundary method for unsteady incompressible flow calculations. *AIAA Paper 2003-1124*.
- [Loginov et al., 2006] Loginov, M., Adams, N., and Zheltovodov, A. (2006). Large-Eddy Simulation of shock-wave/turbulent boundary layer interaction. *J. Fluid Mech.*, 565:133–169.
- [Lüdeke et al., 2004] Lüdeke, H., Radespiel, R., and Schüle, E. (2004). Simulation of streamwise vortices at the flaps of re-entry vehicles. *Prog. Aerospace Sci.*, 8:703–714.
- [Lumley, 1978] Lumley, J. L. (1978). Computational modeling of turbulent flows. *Adv. Appl. Mech.*, 18:123–176.

- [Lund et al., 1998] Lund, T. S., Wu, X., and Squires, K. D. (1998). Generation of Turbulent Inflow Data for Spatially-Developing Boundary Layer Simulations. *J. Comp. Phys.*, 140:233–258.
- [Maeder et al., 2001] Maeder, T., Adams, N., and Kleiser, L. (2001). Direct simulation of turbulent supersonic boundary layers by an extended temporal approach. *J. Fluid Mech.*, 429:187–216.
- [Meyer et al., 2010] Meyer, M., Devesa, A., Hickel, S., Hu, X., and Adams, N. (2010). A conservative immersed interface method for Large-Eddy Simulation of incompressible flows. *J. Comp. Phys.*, 229(18):6300–6317.
- [Morkovin, 1962] Morkovin, M. V. (1962). Effects of compressibility on turbulent flows. In *Mécanique de la Turbulence* (ed. A. Favre), pages 367–380.
- [Nave and Coffey, 1973] Nave, L. H. and Coffey, G. A. (1973). Sea-level side-loads in high area ratio rocket engines. *AIAA Joint Propulsion Conf., AIAA Paper No. 73-1284*.
- [Newman, 2001] Newman, J. S. (2001). Failure-space: a systems engineering look at 50 space system failures. *Acta Astronaut.*, 48:517–527.
- [Östlund et al., 2004] Östlund, J., Damgaard, T., and Frey, M. (2004). Side-load phenomena in highly overexpanded rocket nozzles. *Journal of Propulsion and Power*, 20:695–704.
- [Östlund and Muhammad-Klingmann, 2005] Östlund, J. and Muhammad-Klingmann, B. (2005). Supersonic flow separation with application to rocket engine nozzles. *Appl. Mech. Rev.*, 58:143–177.
- [Piponnier et al., 2009] Piponnier, S., Dussauge, J. P., Debieve, J., and Dupont, P. (2009). A simple model for low-frequency unsteadiness in shock-induced separation. *J. Fluid Mech.*, 629:87–108.
- [Pirozzoli and Bernardini, 2011] Pirozzoli, S. and Bernardini, M. (2011). Turbulence in supersonic boundary layers at moderate Reynolds number. *J. Fluid Mech.*, 688:120–168.
- [Pirozzoli et al., 2010a] Pirozzoli, S., Bernardini, M., and Grasso, F. (2010a). Direct numerical simulation of transonic shock/boundary layer interaction under conditions of incipient separation. *J. Fluid Mech.*, 657:361–393.
- [Pirozzoli and Grasso, 2006] Pirozzoli, S. and Grasso, F. (2006). Direct numerical simulation of impinging shock wave/turbulent boundary layer interaction at $Ma = 2.25$. *Phys. Fluids*, 8:1–17.

- [Pirozzoli et al., 2004] Pirozzoli, S., Grasso, F., and Gatski, T. (2004). Direct numerical simulation and analysis of a spatially evolving supersonic turbulent boundary layer at $M=2.25$. *Phys. Fluids*, 16:530–545.
- [Pirozzoli et al., 2010b] Pirozzoli, S., Larsson, J., Nichols, J. W., Bernardini, M., Morgan, B. E., and Lele, S. K. (2010b). Analysis of unsteady effects in shock/boundary layer interaction. *Center for Turbulence Research Proceedings of the Summer Program*.
- [Plotkin, 1975] Plotkin, K. J. (1975). Shock wave oscillation driven by turbulent boundary-layer fluctuations. *AIAA J.*, 13:1036–1040.
- [Rowley et al., 2009] Rowley, C., Mezic, I., Bagheri, S., Schlatter, P., and Henningson, D. (2009). Spectral analysis of nonlinear flows. *J. Fluid Mech.*, 641:1–13.
- [Ruf et al., 2009] Ruf, J. H., McDaniels, D. M., and Brown, A. M. (2009). Nozzle side load testing and analysis at marshall space flight center. *AIAA Joint Propulsion Conf., AIAA Paper No. 2004-3681*.
- [S, 1996] S, C. I. (1996). Investigation of space launch vehicle catastrophic failures. *AIAA J. Spacecr. Rockets*, 33:198–205.
- [Sarpkaya, 2004] Sarpkaya, T. (2004). A critical review of the intrinsic nature of vortex induced vibrations. *Journal of Fluids and Structures*, 19:389–447.
- [Schmid, 2010] Schmid, P. J. (2010). Dynamic mode decomposition of numerical and experimental data. *J. Fluid Mech.*, 656:5–28.
- [Schmid, 2011] Schmid, P. J. (2011). Applications of the dynamic mode decomposition to experimental data. *Exp. Fluids*, 50:1123–1130.
- [Schwane and Xia, 2005] Schwane, R. and Xia, Y. (2005). Time-accurate CFD predictions and data validation for side load generation by flow-structure coupling in over-expanded rocket nozzles. *Journal of Mathematical Modelling and Algorithms*, 4:53–65.
- [Shahab et al., 2011] Shahab, M. F., Lehnasch, G., Gatski, T. B., and Comte, P. (2011). Statistical Characteristics of an Isothermal, Supersonic Developing Boundary Layer Flow from DNS Data. *Flow Turbulence And Combustion*, 86(3-4):369–397.
- [Shu, 1988] Shu, C. W. (1988). Total-Variation-Diminishing Time Discretizations. *SIAM Journal on Scientific and Statistical Computing*, 9(6):1073–1084.
- [Simeonides, 1993] Simeonides, S. (1993). Hypersonic shock wave boundary layer interactions over simplified deflected control surface configurations. *AGARD Tech Report AR-792*.
- [Smits and Dussauge, 2006] Smits, A. and Dussauge, J. P. (2006). *Turbulent shear layers in supersonic flow*. Springer.

- [Smits and Muck, 1987] Smits, A. and Muck, K. (1987). Experimental study of three shock wave/turbulent boundary layer interactions. *J. Fluid Mech.*, 182:291–314.
- [Smits et al., 1983] Smits, A. J., Matheson, N., and Joubert, P. N. (1983). Low-reynolds number turbulent boundary layers in zero and favourable pressure gradients. *J.Ship. Res.*, 27:147–157.
- [Spalart, 1988] Spalart, P. R. (1988). Direct simulation of a turbulent boundary layer up to $Re_\theta = 1410$. *J. Fluid Mech.*, 187:61–98.
- [Spalart and Leonard, 1985] Spalart, P. R. and Leonard, A. (1985). Direct numerical simulation of equilibrium turbulent boundary layers. *5th Symposium on Turbulent Shear Flows*, page 9.
- [Stolz and Adams, 2003] Stolz, S. and Adams, N. A. (2003). Large-eddy simulation of high-Reynolds-number supersonic boundary layers using the approximate deconvolution model and a rescaling and recycling technique. *Phys. Fluids*, 15:2398.
- [Summerfield et al., 1954] Summerfield, M., Foster, C. R., and Swan, W. C. (1954). Flow separation in overexpanded supersonic exhaust nozzles. *Jet Propuls.*, 24:319–321.
- [Sunley and Ferriman, 1964] Sunley, H. L. G. and Ferriman, V. N. (1964). Jet separation in conical nozzles. *J. R. Aeronaut. Soc.*, 8:808–818.
- [Toro, 2006] Toro, E. (2006). *Riemann Solvers and Numerical Methods for Fluid Dynamics: A Practical Introduction*. Springer.
- [Touber, 2009] Touber, E. (2009). Large-eddy simulation of low-frequency unsteadiness in a turbulent shock-induced separation bubble. *Theoretical and Computational Fluid Dynamics*, 23:79–107.
- [Touber and Sandham, 2009] Touber, E. and Sandham, N. (2009). Large-eddy simulation of low-frequency unsteadiness in a turbulent shock-induced separation bubble. *Theor. Comp. Fluid Dyn.*, 23:79–107.
- [Touber and Sandham, 2010] Touber, E. and Sandham, N. D. (2010). Unsteadiness in shock-wave/boundary-layer interactions. *Ph.D. Thesis*.
- [Tritton, 1959] Tritton, D. (1959). Experiments on the flow past a circular cylinder at low Reynolds number. *J. Fluid Mech.*, 6:547–567.
- [Tseng and Ferziger, 2003] Tseng, Y. and Ferziger, J. (2003). A ghost-cell immersed boundary method for flow in complex geometry. *J. Comp. Phys.*, 192:593–623.
- [Veloudis et al., 2007] Veloudis, I., Yang, Z., McGuirk, J. J., Page, G. J., and Spencer, A. (2007). Novel Implementation and Assessment of a Digital Filter Based Approach for the Generation of LES Inlet Conditions. *Flow Turbulence And Combustion*, 79(1):1–24.

- [Verma and Haidn, 2009] Verma, S. B. and Haidn, O. (2009). Study of restricted shock separation phenomena in a thrust optimized parabolic nozzle. *Journal of Propulsion and Power*, 25:1046–1057.
- [Vreman et al., 1995] Vreman, B., Geurts, B., and Kuerten, H. (1995). A priori tests of large eddy simulation of the compressible plane mixing layer. *Journal of Engineering Mathematics*, 29(4):299–327.
- [Wang, 2004] Wang, T. S. (2004). Transient three-dimensional analysis of side load in liquid rocket engine nozzles. *AIAA Joint Propulsion Conf., AIAA Paper No. 2004-3681*.
- [Wang, 2009] Wang, T. S. (2009). Transient three-dimensional startup side load analysis of a regeneratively cooled nozzle. *Shock Waves*, 19:251–264.
- [Williamson, 1996] Williamson, C. (1996). Vortex dynamics in the cylinder wake. *Ann. Rev. Fluid. Mech.*, 28:477–539.
- [Williamson and Goverdhan, 2004] Williamson, C. and Goverdhan, R. (2004). Vortex-induced vibrations. *Ann. Rev. Fluid. Mech.*, 36:413–455.
- [Wu and Martin, 2007] Wu, M. and Martin, M. (2007). Direct numerical simulation of shockwave and turbulent boundary layer interaction induced by a compression ramp. *AIAA J.*, 45:879–889.
- [Wu and Martin, 2008] Wu, M. and Martin, M. (2008). Analysis of shock motion in shockwave and turbulent boundary layer interaction using direct numerical simulation data. *J. Fluid Mech.*, 594:71–83.
- [Zandonade et al., 2004] Zandonade, P. S., Langford, J. A., and Moser, R. D. (2004). Finite-volume optimal large-eddy simulation of isotropic turbulence. *Phys. Fluids*, 16(7):2255.
- [Zheltovodov, 1991] Zheltovodov, A. (1991). Peculiarities of development and modeling possibilities of supersonic turbulent separated flows. In *In Separated Flows and Jets: IUTAM Symposium, July 9-13, 1990*, pages 225–236, Novosibirsk, USSR.
- [Zheltovodov et al., 1990] Zheltovodov, A., Trofimov, V., Schülein, E., and Yakovlev, V. (1990). An experimental documentation of supersonic turbulent flows in the vicinity of forward- and backward-facing ramps. In *Tech. Rep. 2030*, Inst. Theor. Appl. Mech., USSR Acad. Sci., Novosibirsk.
- [Zheltovodov and Yakovlev, 1986] Zheltovodov, A. and Yakovlev, V. (1986). Stages of development, flowfield structure and turbulence characteristics of compressible separated flows in the vicinity of 2-D obstacles. In *Preprint 27D86 ITAM (in Russian)*, Inst. Theor. Appl. Mech., USSR Acad. Sci., Novosibirsk.